UNIVERSITÀ DEGLI STUDI DI PADOVA

Dipartimento di Fisica e Astronomia "Galileo Galilei"

Master Degree in Physics

Final Dissertation

Probing the asymmetry of matter distribution in galaxy clusters' environment with hydrodynamical simulations

Thesis supervisor

Prof. Sabino Matarrese

Thesis co-supervisors

Dr. Nabila Aghanim

Dr. Céline Gouin

Candidate

Stefano Gallo

Academic Year 2020/2021

Abstract

Galaxy clusters are the most massive cosmic structures in the Universe, and are connected at their peripheries to extended and complex filamentary structures, that act as funnels for the infalling material. This network of clusters and filaments is known as the cosmic web. For this reason, matter distribution in and around galaxy clusters is far from being isotropic, and the anisotropies are related to the processes of structure formation, with different matter components (dark matter, galaxies and different gas phases) being affected by different physical effects.

Therefore, in this work we decided to study the asymmetries in the distributions of the different matter components from the central regions of galaxy to their outskirts. For this analysis we used the data from the cosmological hydrodynamical simulation IllustrisTNG. To characterize the asymmetries of the matter distribution we used two methods, both based on an harmonic decomposition of the projected matter density: the harmonic power excess, and the β parameters, which we introduce here for the first time.

In the first part of the work we used the harmonic power excess to study the asymmetries of galaxy and gas distributions in and around galaxy clusters, with respect to the background distribution. We found that, on average, matter distribution in the inner cluster regions tends to be elliptical in shape, while the outskirts of clusters present a more complex harmonic signature, pointing towards the presence of filamentary structures. We also observed that different gas phases trace different structures in galaxy clusters: while the hot gas (that has been shock heated to high temperatures) is mainly found inside clusters, and traces their elliptical shapes, the warm-hot intergalactic medium is a better tracer for the filaments that connect to the clusters' outskirts.

In the second part of the project we used the β parameters to quantify the level of asymmetry in dark matter and gas distributions in clusters' environments. We then related these quantities to the cluster properties. We found that the level of asymmetries is correlated to the geometrical properties of the matter density field, such as the ellipticity and the number of filaments around clusters, called the connectivity. It also shows dependencies on the radial distance from the cluster center, on the cluster mass, and on the cluster dynamical state.

This work shows that the harmonic decomposition of the projected matter density can be a powerful tool to probe the departure from spherical symmetry of the matter distribution, and the level of asymmetry of the various matter components can be used as a probe of the cluster properties.

Contents

Chapter 1

Introduction

Being the most massive cosmic structures in the Universe, galaxy clusters lay at the interface of astrophysics and cosmology, and are extremely interesting in both perspectives.

Galaxy clusters are multi-component objects: while most of their mass in the form of dark matter (DM), they also contain hot and diffuse gas called the intracluster medium (ICM), and of course a large number of galaxies, typically from a few hundreds to a few thousands (although they only contribute to around 5% to the total mass of the cluster). Each of these matter components provide important information on the physical processes happening inside clusters, from details about their formation history, to thermodynamical properties of the gas, to feedback mechanisms involving supernovae and active galactic nuclei (AGN), just to make some examples.

Furthermore, galaxy clusters are far from being isolated objects. On the contrary, they form at the nodes of a complex, web-like structure called the "cosmic web" [6]. This network of filaments, connecting clusters to each other, as been observed in both simulations (e.g. [6,57]) and large galaxy surveys [11,13,72].

In the cluster outskirts, where the filaments connect to them and act as channels for the continuously infalling matter, a lot more interesting physical effects can be studied. For example, in these regions a departure from hydrostatic equilibrium is expected, as well as distinctive marks of accretion physics such as shocks and turbulent gas motion, which affect the density distribution of the gas. Moreover, a detailed description of the cluster gas up to large radii is important for better constraining cluster properties such as the mass, which in turn are crucial for using clusters as accurate cosmological probes. Indeed, the mass function of galaxy clusters is commonly used to constrain cosmological parameters of the ΛCDM model such as the matter density parameter (Ω_m). [55]

In the standard picture of hierarchical structure formation scenario, galaxy clusters are formed mainly by merging of smaller groups [65], and are therefore expected to show a spatial matter distribution that is not spherically symmetric in general, especially the most massive ones [14,22,31]. Indeed, it has been observed that they are better approximated as triaxial objects, rather than spherical ones [21,23,35]. Furthermore, they continue to accrete galaxies, gas and smaller groups, preferentially through the filamentary structures of the cosmic web, that connect to their outer regions [56,66]. For this reason, matter distribution in the outskirts of galaxy clusters is expected to deviate even more largely from spherical symmetry (see for example [19,21,23]).

In order to characterize these asymmetries, a statistical method called "harmonic power excess" has been developed by [23], and has been successfully applied to the dark matter [23] and galaxy distributions [21] in clusters' environments. These studies form the basis of our work. This method consists in a harmonic decomposition of a 2D projected density field in clusters' environments. By averaging

such decomposition over a large number of clusters, one can highlight azimuthal symmetries on the cluster shape and their surroundings.

In this work we want to explore the distribution and asymmetries of the different matter components in the environments of galaxy clusters from the cosmological simulation IllustrisTNG [45]. There are two main questions we are interested in answering:

1. What are the asymmetries of matter in galaxy clusters with respect to the background density field of the Universe? And do different components have the same behaviour?
2. How much does the matter distribution in galaxy clusters deviate from the spherical symmetry? And how does the level of asymmetry correlate to the cluster properties?

We address the first question using the harmonic power excess method, in particular applying it for the first time on the distribution of gas, and comparing our results with the previous studies of [21, 23].

To try and answer the second questions we introduce a new set of estimators, which we call β parameters (partly inspired by [66]), which quantify the powers of the most relevant orders of the harmonic decomposition with respect to a spherical distribution. We aim to capture in this way the level of asymmetry, and relate it to the physical cluster properties.

This thesis is organized in the following way:

In Chapter 2 we introduce the theoretical background of our work, presenting elements of cosmology and structure formation theory, and describing the main properties of galaxy clusters, which are the focus of this work.

In Chapter 3 we describe the IllustrisTNG simulations, from which we extracted the dataset we then used for our analysis. We explain the data selection and post-processing.

In Chapter 4 we detail the methods and statistical estimators used in the analysis, in particular the harmonic power excess and the β parameters, that give us information on the asymmetry of matter distribution.

Then, in Chapters 5 and 6 we describe our analyses and present our results with the harmonic power excess applied on the galaxy and gas distributions, respectively.

In Chapter 7 we present the results of the analyses of the β parameters on the gas distribution, relating it to different cluster properties.

Finally, in Chapter 8 we summarize our results and draw the conclusions of our work.

Chapter 2

Theoretical Background

In this chapter, we present the main theoretical topics that serve as a background for our work. In the first Section 2.1 we introduce some basic notions of cosmology, together with important parameters that will be used later in the analysis. In the second Section 2.2 summarize about the theory of structure formation, introducing the concept of gravitational instability and different methods describing the growth of structures. Finally, in the third Section 2.3, we present galaxy clusters, which are the object of our analysis, listing their most important properties and some observational aspects. For writing this chapter, we mostly followed the following books and review articles: [12, 33, 53, 68].

2.1 Cosmology

Cosmology aims to understand the Universe in its entirety, studying its properties, composition and evolution, from its beginnings to the present time and beyond. The foundations of cosmology in its standard form lie in two pillars: a theory of gravity and the "Cosmological Principle".

Gravity is the strongest force acting on cosmological scales, and the best candidate to describe it is Einstein's theory of General Relativity. In this context, gravity is seen as a geometrical property of the spacetime, which is deformed by the presence of mass.

A curved spacetime is described by the metric tensor, $g_{\mu\nu}$, and the distance between two spacetime events can be written as $\mathrm{d}s^2 = g_{\mu\nu}\mathrm{d}x^\mu \mathrm{d}x^\nu$. The relation between the metric and the mass-energy content is given by Einstein's Equations:

$$R_{\mu\nu} - \frac{1}{2} g_{\mu\nu} R = \frac{8\pi G}{c^4} T_{\mu\nu} \tag{2.1}$$

where $R_{\mu\nu}$ and R are respectively the Ricci tensor and scalar, which are contractions of the Riemann tensor $R^\alpha_{\mu\beta\nu}$, G is the gravitational constant, c is the speed of light, and $T_{\mu\nu}$ is the stress-energy tensor. The Riemann tensor holds information on the local curvature of spacetime, and it's constructed with the metric tensor and its first and second derivatives. The stress-energy tensor describes the distribution of mass-energy in the Universe, and for a perfect fluid it can be written as:

$$T_{\mu\nu} = \left(p + \rho c^2\right) u_\mu u_\nu - p g_{\mu\nu} \tag{2.2}$$

where p and ρ are the energy density and pressure of the fluid, and u_μ is its 4-velocity.

Einstein's equations are notoriously very difficult to solve, even in simple cases, so we need to place some initial simplifying assumptions on the metric if we are to hope for a solution for the evolution of the Universe. This is where the Cosmological Principle comes in.

The Cosmological Principle states that, on large scales, every comoving observer[1] (at fixed time in its reference frame) sees the Universe as homogeneous and isotropic.

From these assumptions, justified by observations (such as the Cosmic Microwave Background, or CMB), one can easily write the metric of the Universe under these symmetries, called the Friedmann-Lemaître-Robertson-Walker metric:

$$ds^2 = -dt^2 + a^2(t)\left[\frac{dr^2}{1-kr^2} + r^2\left(d\theta^2 + \sin^2\theta d\phi^2\right)\right] \tag{2.3}$$

given in comoving polar coordinates, where $a(t)$ is the scale factor, which governs the expansion of the Universe (and it is usually normalized to 1 at present time t_0), and k is a constant that describes its spatial curvature. Thereby, $k = 0$ describes a flat Universe and $k = +1, -1$ describe closed or open Universes respectively.

In this metric, and taking the stress-energy tensor of a perfect fluid, Einstein's equations become the Friedmann equations:

$$\begin{aligned}\left(\frac{\dot{a}}{a}\right)^2 &= \frac{8\pi G}{3}\rho - \frac{kc^2}{a^2} \\ \frac{\ddot{a}}{a} &= -\frac{4\pi G}{3}\left(\rho + \frac{3p}{c^2}\right)\end{aligned} \tag{2.4}$$

where $\dot{a}$ and $\ddot{a}$ are the first and second derivatives of a with respect of time. These equations depend on three unknown functions: the scale factor $a(t)$, and the fluid density $\rho(t)$ and pressure $p(t)$. To be solved they require the introduction of a third equation, the equation of state (EoS), relating p and ρ.

The most relevant components of cosmological interest can be described by an EoS of the type $p = w\rho c^2$, where the choice of w discriminates between the various types of fluids. The three main components of the Universe are:

- Matter (non-relativistic): can be well approximated by a pressureless dust with $w = 0$
- Radiation: has $w = 1/3$ and includes photons and ultra-relativistic (non-degenerate) particles
- Cosmological constant Λ: has $w = -1$ and is used as an approximation for dark energy

If we consider each of these components separately, as if the Universe contained only one component, we can substitute the equation of state in the Friedmann equations 2.4. Then, assuming $k = 0$ (which is consistent with the experimental result), we can solve the equations and find that:

- For a matter Universe: $\rho(a) = \rho_m(a) \propto a^{-3}, \quad a(t) \propto t^{2/3}$
- For a radiation Universe: $\rho(a) = \rho_r(a) \propto a^{-4}, \quad a(t) \propto t^{1/2}$
- For a Λ Universe: $\rho = \rho_\Lambda = \text{const}, \quad a(t) \propto e^{Ht}$

Obviously, we know that the Universe is not entirely filled with only one component, but these solutions are nonetheless important because they describe well the behaviour of the Universe when one

[1] An observer that is at rest with respect to the source of geometry of the Universe, i.e. one that is following the expansion of the Universe

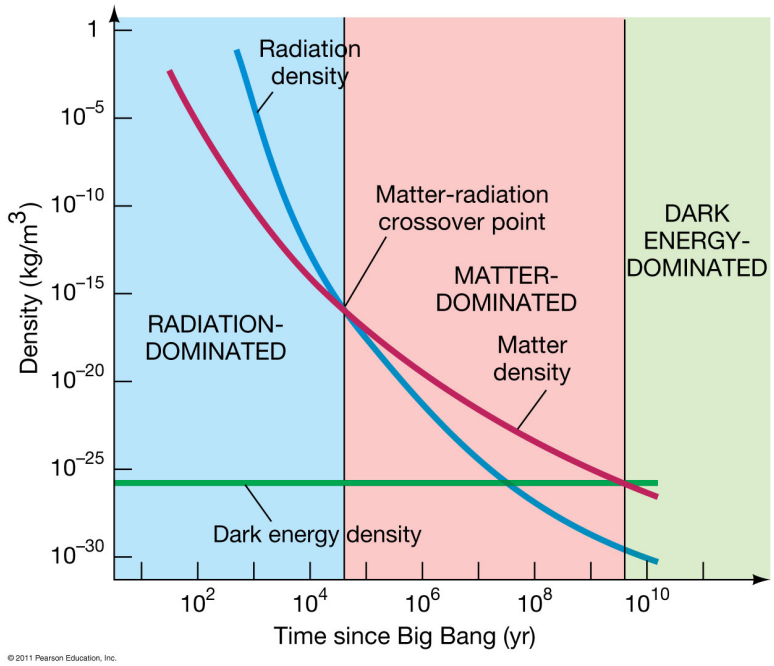

Figure 2.1: Density evolution of the different cosmological components through cosmic time: radiation, matter and dark energy. Credits: Pearson Education.

component dominates over the others. Also, when looking at the dependence of the energy density with respect to a, we can see that ρ_r decreases faster than ρ_m, while ρ_Λ remains constant. This means that, in an Universe containing these three components, we expect to have an early phase in which the energy budget is dominated by radiation, a central era dominated by matter[2], and a late phase in which the Cosmological constant becomes the dominant component, while the other two get more and more diluted by the expansion, as shown in Fig. 2.1, which shows the density evolution of the three components over cosmic time.

At this point, what we need to fix in the cosmological model, are the values of the energy densities of the various components at some reference time (usually today). To do this, it is customary to introduce a dimensionless parameter called the "density parameter". This is defined as the ratio between the energy density ρ_i of the species i, and the critical energy density ρ_c. The latter is the energy density required to have spatial curvature $k = 0$, and can be calculated from the first Friedmann equation 2.4 to be:

$$\rho_c = \frac{3}{8\pi G}\left(\frac{\dot{a}}{a}\right)^2 \tag{2.5}$$

so the density parameter is:

$$\Omega_i \equiv \frac{\rho_i}{\rho_c} = \frac{8\pi G\rho_i}{3}\left(\frac{\dot{a}}{a}\right)^{-2}. \tag{2.6}$$

From this definition we can also see that the total density parameter $\Omega = \sum_i \Omega_i$ is exactly equal to 1 if the Universe is flat.

[2]This phase does not actually arise in all cases: if the Cosmological constant is high enough, it may already be dominant by the time matter and radiation equal each other.

Before talking about the current favoured cosmological model, let us introduce two important quantities related to the scale factor: the Hubble parameter and the redshift. The Hubble parameter is defined as

$$H(t) = \frac{\dot{a}(t)}{a(t)} \tag{2.7}$$

and it's a measure of the rate of expansion of the Universe. The value of H today, $H_0 = H(t_0)$, is usually written as $H_0 = 100h\ \mathrm{km\,s^{-1}\,Mpc^{-1}}$ where h is an adimensional parameter accounting for the uncertainty on the value of H_0 present in the literature (for a review on this tension, see for example [15]).

The redshift z is a variable that accounts for the increase of photon wavelengths due to the expansion of the Universe, as they travel towards us from distant sources (an effect similar to the Doppler shift that occurs when a source is moving away from the observer). It is defined as

$$z = \frac{\lambda_{\mathrm{obs}} - \lambda_{\mathrm{em}}}{\lambda_{\mathrm{em}}} \tag{2.8}$$

in which λ_{obs} and λ_{em} are, respectively, the wavelength of the light observed and the one emitted by the source. If the emitter and the observer are both comoving observers, the redshift can be related to the scale factor by the formula:

$$1 + z = \frac{a(t_{\mathrm{obs}})}{a(t_{\mathrm{em}})} \tag{2.9}$$

Starting from a measure of redshift one can get an estimate of the "distance"[3] of the source from our position, once we fix the cosmological model.

Now that we have the basic ingredients, we can introduce the current standard cosmological model, called ΛCDM. The name comes from its two main components: Λ is the cosmological constant, or dark energy, which is the energy that drives the accelerated expansion of the Universe, and constitutes $\sim 70\%$ of its energy budget today; while CDM stands for "cold dark matter", in which dark refers to a kind of matter that interacts (almost) only gravitationally with the other components, and cold means that the dark matter particles are non-relativistic (i.e. their velocity is much smaller than c).

Dark matter (DM) makes up around 25% of the total energy budget of the Universe today, while the baryonic[4] matter (i.e. ordinary matter, which includes stars, galaxies and gas) only represents around 5% of the total energy density. In this model it is also assumed that the Universe is flat, since the measurements of the spatial curvature from the CMB are consistent with $k = 0$.

The exact cosmological parameters we will use in this work are the ones extracted from the observations of the Planck satellite, quoted in [51]: $\Omega_{\Lambda,0} = 0.6911$, $\Omega_{matter,0} = 0.3089$, $\Omega_{baryon,0} = 0.0486$, $h = 0.6774$.

[3] The concept of distance in cosmology is a quite broad topic that would require a lengthier discussion, which is beyond the scope of this simple summary.

[4] In cosmology it is usual to refer to both baryons and leptons under the collective name of baryons, since the former are the ones contributing the most to the energy budget today

2.2 Structure Formation

So far, we only talked about the Universe as if it were perfectly homogeneous and isotropic, but in fact we know that it is not exactly the case. Indeed, our Universe is only homogeneous on very large scales (over $\sim$ 100 Mpc), while below that scale it becomes highly inhomogeneous, with matter arranged in a complex network of nodes, filaments and walls, hosting collapsed structures with sizes ranging from stars to clusters of galaxies. This is known as the "cosmic web" [6], and it is the result of the anisotropic collapse, under the effect of gravity, of initial fluctuations in the matter density field [73].

The current favoured model for the formation of cosmic structures is the "hierarchical clustering" model, which in brief states that the first structures to form were the smaller ones, which then clustered, merged and accreted material to form larger and larger structures.

The story of structure formation begins in the primordial Universe, right after inflation, when small fluctuations of the matter density field are supposed to be formed. They can be modeled as a realization of an homogeneous and isotropic random Gaussian field (e.g. [25]). These initial fluctuations are the seeds of all the structures we see in the Universe today. With time, these small fluctuations evolve under the effect of gravity, attracting material from their surroundings, thus becoming larger and exerting a stronger gravitational pull, attracting more matter. This effect is known as "gravitational instability", and it is believed to be the main driving process in the formation of structures.

Eventually, as the density fluctuations grow, some of those reach the point where the gravitational pull becomes strong enough that the matter they are composed of starts collapsing towards the center of the fluctuation, forming a gravitationally bound object. This process happens first at small scales forming the first isolated structures. Later these small halos collapse in turn into larger structures, and so on until forming the extended filamentary web-like structure we observe today (for example [11,13,72]).

A note before proceeding: as we stated in the previous Section, when we talk about matter, the main component we refer to is dark matter, which drives the gravitational collapse and forms the "backbone" of the cosmic web, while baryons are mostly "dragged" into the potential wells created by DM. For this reason, and because dark matter does not require to deal with the complicated baryonic physics, in this Section we will mostly ignore baryons, focusing only on dark matter, which gives already an excellent insight on the process of structure formation. The physics of baryons becomes important for structure formation when considering galaxy clusters, for example, as we will mention in the next Section 2.3.

2.2.1 Gravitational Instability

Gravitational instability was first studied by Jeans [28] in 1902, in the context of a static background, to understand how stars and planets form from a cloud of gas. Applying this theory to the cosmological case provides a good picture of structure formation, as long as the fluctuations remain small (i.e. in the linear regime) [53].

In principle, to attack the problem of the evolution of small density perturbations, we should consider the perturbed form of the Friedmann equations and solve them. In practice, in the limit of small fluctuations, we can make some simplifications. We start with the assumption that dark matter can be treated as a fluid, and that it is non-relativistic, so that the use of the Newtonian treatment is justified. We can therefore write the fluid equations in the Newtonian setting, i.e. the continuity, Euler and Poisson equations:

$$\begin{aligned}
&\left.\frac{\partial \rho}{\partial t}\right|_{\mathbf{r}} + \nabla_{\mathbf{r}} \cdot (\rho \mathbf{u}) = 0 \\
&\left.\frac{\partial \mathbf{u}}{\partial t}\right|_{\mathbf{r}} + (\mathbf{u} \cdot \nabla_{\mathbf{r}})\, \mathbf{u} = -\frac{1}{\rho} \nabla_{\mathbf{r}} p - \nabla_{\mathbf{r}} \Phi \\
&\nabla^2_{\mathbf{r}} \Phi = 4\pi G \rho
\end{aligned} \tag{2.10}$$

where ρ, $\mathbf{u}$ and p are the density, velocity and pressure of the fluid, respectively, while Φ is the gravitational potential. These equations are written in physical coordinates $\mathbf{r}$, but we want them in comoving coordinates $\mathbf{x}$. To do so, we use the relations:

$$\begin{aligned}
&\mathbf{r} = a(t)\mathbf{x} \\
&\mathbf{u} = \dot{\mathbf{r}} = \dot{a}\mathbf{x} + a\dot{\mathbf{x}} = H\mathbf{r} + \mathbf{v} \\
&\nabla_{\mathbf{r}} f = \frac{1}{a} \nabla_{\mathbf{x}} f \\
&\left.\frac{\partial f}{\partial t}\right|_{\mathbf{r}} = \left.\frac{\partial f}{\partial t}\right|_{\mathbf{x}} - H\, (\mathbf{r} \cdot \nabla_{\mathbf{r}})\, f
\end{aligned} \tag{2.11}$$

where the dot represent the total derivative with respect to time, H is the Hubble parameter and f is a generic function. We also define $\mathbf{v} = a\dot{\mathbf{x}}$ [5]. Applying these relations we obtain:

$$\begin{aligned}
&\left.\frac{\partial \rho}{\partial t}\right|_{\mathbf{x}} + 3H\rho + \frac{1}{a} \nabla_{\mathbf{x}} (\rho \mathbf{v}) = 0 \\
&\left.\frac{\partial (Ha\mathbf{x} + \mathbf{v})}{\partial t}\right| + (\mathbf{v} \cdot \nabla_{\mathbf{x}}) H\mathbf{x} + \frac{1}{a} (\mathbf{v} \cdot \nabla_{\mathbf{x}}) \mathbf{v} = \frac{1}{\rho a} \nabla_{\mathbf{x}} p - \frac{1}{a} \nabla_{\mathbf{x}} \Phi \\
&\nabla^2_{\mathbf{x}} \Phi = 4\pi G a^2 \rho
\end{aligned} \tag{2.12}$$

At this point, what we need to do to proceed with the solution is separating the evolution of the background fluid from the evolution of the fluctuations, which is what is actually interesting for us. To do so, we rewrite the fluid quantities as the sum of a background term, which follows the Friedmann equations, and a small perturbation term, that accounts for the fluctuations. After inserting them in the equations, we will then consider only the terms that are linear in the perturbations. Before doing that though, we make a final simplification: we neglect the pressure term in the Euler equation. This approximation is justified if we look at scales much larger than the Jeans scale[6], that determines the scale above which the gravitational force starts dominating over the pressure forces. So, we can write (with a slight abuse of notation for $\mathbf{v}$):

$$\begin{aligned}
&\rho(\mathbf{x}, t) = \rho_b(t)(1 + \delta(\mathbf{x}, t)) \\
&\mathbf{v}(\mathbf{x}, t) = \mathbf{0} + \mathbf{v}(\mathbf{x}, t) \\
&\Phi(\mathbf{x}, t) = \Phi_b(\mathbf{x}, t) + \phi(\mathbf{x}, t)
\end{aligned} \tag{2.13}$$

So, substituting these quantities in Eq. 2.12 and considering only the linear terms in the perturbations, we arrive to the set of equations we want to solve:

[5] The quantity $\dot{\mathbf{x}}$, which is the velocity with respect to the comoving coordinates, is called "peculiar velocity".

[6] The Jeans length is defined as $\lambda_j = c_s \sqrt{\frac{\pi}{G\rho_{\mathrm{b}}}}$, where c_s is the sound speed in the fluid, G is the gravitational constant, and ρ_{b} is the mean background density of the Universe.

$$\begin{aligned}
&\left.\frac{\partial \mathbf{v}}{\partial t}\right|_{\mathbf{x}} + H\mathbf{v} + \frac{1}{a}\left(\mathbf{v}\cdot\nabla_{\mathbf{x}}\right)\mathbf{v} = -\frac{1}{a}\nabla_{\mathbf{x}}\phi \\
&\left.\frac{\partial \delta}{\partial t}\right|_{\mathbf{x}} + \frac{1}{a}\nabla\cdot\mathbf{v} = 0 \\
&\nabla^2\phi = 4\pi G a^2 \rho_b \delta.
\end{aligned} \tag{2.14}$$

Manipulating these equations we finally arrive to

$$\frac{\partial^2\delta}{\partial t^2} + 2H(t)\frac{\partial\delta}{\partial t} - 4\pi G\rho_b\delta = 0 \tag{2.15}$$

which is our final equation, describing the evolution of a small density fluctuation in an expanding Universe. A generic solution to this equation is of the form:

$$\delta(\mathbf{x},t) = \delta_+\left(\mathbf{x},t_i\right)D_+(t) + \delta_-\left(\mathbf{x},t_i\right)D_-(t) \tag{2.16}$$

which has a growing $(+)$ and a decaying $(-)$ part, where $\delta_\pm$ are the spatial distributions of the growing/decaying modes at some reference time t_i, while $D_\pm$ are the functions regulating their evolution which depend on the chosen cosmology. Since the decaying modes tend to disappear, it is usual to consider only the growing ones, which are the only interesting ones for the study of structure formation.

As an example, we can see what is the result for a flat, matter-dominated Universe, for which we have:

$$a(t) \propto t^{2/3} \quad H = \frac{2}{3t} \quad \rho_b = \frac{1}{6\pi G t^2} \tag{2.17}$$

Substituting into Eq. 2.15 and solving the equation we get

$$\begin{aligned}
D_+(t) \propto t^{2/3} \propto a(t) \qquad D_-(t) \propto t^{-1} \propto H(t) \\
\delta(t) = \delta_+\left(t_i\right)\left(t/t_i\right)^{2/3} + \delta_-\left(t_i\right)\left(t/t_i\right)^{-1}
\end{aligned} \tag{2.18}$$

This result shows that there is indeed a gravitational instability and confirms the picture we drew in the beginning: small fluctuations in the density field in the primordial Universe can grow thanks to this effect, attracting matter from their surroundings and increasing their overdensity compared to mean density.

2.2.2 Beyond linear theory

So far, we have considered the linear evolution of perturbations, which gives very important information in the first phase of growth, but is valid only until $\delta \ll 1$. When the overdensities become of order 1, the linear theory is no longer adequate to describe them and we enter the non-linear regime.

Solving the full non-linear evolution of perturbations in the Universe is extremely complicated and in general analytically intractable, so different strategies have been developed to follow the process of structure formation beyond the linear regime. Here we discuss some of these methods.

Spherical Top-hat Collapse Model

One relatively straightforward way to obtain an analytical solution for a problem is stripping it down to a particularly simplified form, the solution of which, although not directly comparable to the real case, can often yield important insights on the problem. In our case, the simplest model one can imagine for describing the collapse of structures is the so-called "spherical top-hat model". It consists of an isolated, spherical perturbation of constant overdensity $\rho_p(t) = \rho_b(t)(1 + \delta_p(t))$ inside (which represented in 2D would look like a top hat, hence the name), whose peculiar velocity is 0 in the beginning. We assume that at the initial time t_i, we have $\delta_i \equiv \delta_p(t_i) > 0$, and $\delta_i \ll 1$. For simplicity we also consider a background Universe that is flat and matter dominated ($\Omega_m = \Omega = 1$).

The spherical symmetry of this configuration allows us to solve exactly the equations for the perturbation, and one can show that it actually evolves as a separate Universe , with $\Omega_p(t_i) = \Omega(t_i)(1 + \delta_i)$. In our case this corresponds to a closed Universe ($k = 1$).

It can be shown that such a Universe evolves according to the following set of parametric equations in the parameter θ:

$$\begin{cases} a(\theta) = \frac{a_i}{2}\frac{\Omega_i}{\Omega_i - 1}(1 - \cos\theta) \\ t(\theta) = \frac{1}{2H_i}\frac{\Omega_i}{(\Omega_i - 1)^{3/2}}(\theta - \sin\theta) \end{cases} \tag{2.19}$$

where the subscript i refers to the initial time. From these equations we can see that a Universe like this first experiences a period of expansion: the scale factor grows until $\theta = \pi$ which corresponds to the "turn-around" time t_{TA}. It then starts contracting and collapsing to $a = 0$ with infinite density when $\theta = 2\pi$ and $t = 2t_{TA} \equiv t_c$. We expect our spherical perturbation to behave in a similar way, with the important difference that it does not collapse to a point in the end: in the real case we expect that, when the density gets high, slight departures from spherical symmetry will produce shocks, which will convert some of the infalling kinetic energy into random thermal motion. Therefore, we will end up in an equilibrium configuration, where the virial theorem can be applied.

The virial theorem states that $2E_{\rm kin} + E_{\rm gr} = 0$ (where $E_{\rm kin}$ and $E_{\rm gr}$ are the kinetic and gravitational energy respectively), from which we deduce that $E_{\rm tot} = \frac{1}{2}E_{\rm gr}$. So, for the spherical overdensity at equilibrium we will have:

$$E_{\rm vir} = -\frac{1}{2}\frac{3GM^2}{5R_{\rm vir}} \tag{2.20}$$

where M is the mass contained in the collapsed object, and $R_{\rm vir}$ is its virial radius.

On the other hand, at the moment of "turn-around", we have that $E_{\rm kin} = 0$, so if we ignore all the possible losses of mass and we assume conservation of energy, the total energy is just the gravitational one:

$$E_{\rm TA} = -\frac{3GM^2}{5R_{\rm TA}} = E_{\rm vir} \tag{2.21}$$

from which we derive that $R_{\rm TA} = 2R_{\rm vir}$, and for the volumes $V_{\rm TA} = 8V_{\rm vir}$, so that the density inside the sphere will be

$$\rho(t_{\rm vir}) = 8\rho(t_{\rm TA}) \tag{2.22}$$

Using equations from the previous Section 2.2.1 we can calculate the ratio between the density inside the virialized perturbation and the one of the background:

$$\frac{\rho_p\left(t_{\rm vir}\right)}{\rho_b\left(t_{\rm vir}\right)} = \frac{\rho_p\left(t_{\rm vir}\right)}{\rho_p\left(t_{\rm TA}\right)}\frac{\rho_p\left(t_{\rm TA}\right)}{\rho_b\left(t_{\rm TA}\right)}\frac{\rho_b\left(t_{\rm TA}\right)}{\rho_b\left(t_{\rm vir}\right)} \simeq 180 \tag{2.23}$$

To summarize, we found that a spherical "top-hat" perturbation expands for some time following the background Universe. Then after a time $t_{\rm TA}$ it stops expanding and starts collapsing, ending up in a virialized final state, after $t_{\rm vir} \approx 2t_{\rm TA}$, when it becomes a bound object with an overdensity of $\delta_p \sim 180$.

This last result is particularly relevant in cosmology since it has become customary, in both simulations and observations, to quote the radius of structures based on the mean overdensity enclosed within that radius. It is defined as the radius R_Δ of a sphere within which the mean density is $\Delta \times \rho_c(z)$, where Δ is a number that can be chosen according to the specific use. For this reason, the rounded up value of $\Delta = 200$ for the overdensity is historically used to define a virialized structure. Actually, for a ΛCDM model, the virial radius of a top-hat spherical perturbation at $z = 0$ comes out to be approximately $R_{100} = 1.36R_{200}$. However, the use of R_{200} for the radius of structures is common in the literature, and we will also use it in this work.

Zel'dovich Approximation

The spherical collapse model described before, although instructive, is not at all realistic, and cannot be compared with observations. Another approach to describe the formation of structures in an analytical way, beyond the linear regime, is the Zel'dovich approximation [73], developed by Yakov B. Zel'dovich in 1970. This theory is a first-order Lagrangian perturbation theory, in contrast to the first-order Eulerian theory, which is the one we developed in Sec. 2.2.1. What this means is that the Zel'dovich approximation is a linear approximation in the displacement of particles, rather than the density. In this picture the particles are moving on straight lines in a sort of inertial motion, dictated by the initial density perturbations. This approximation stops being predictive once the particles with different Lagrangian coordinates start crossing each other's path, arriving at the same Eulerian coordinate, thus forming regions of infinite density called "caustics".

The great advantage of this method is that the velocity perturbations remain linear for much longer than the density ones, especially at large scales. This means that we can follow their trajectories far into the density's non-linear regime. [12, p.290-292]

So, the central point of the Zel'dovich approximation is that the velocity of the particles is assumed to remain constant, and equal to the initial value which depends on the gravitational potential generated by the density perturbations:

$$\mathbf{v}_0(\mathbf{q}) = -\nabla_{\mathbf{q}}\phi_0(\mathbf{q}) \tag{2.24}$$

where $\mathbf{x}$ is the Eulerian (comoving) coordinate, while $\mathbf{q}$ is the Lagrangian coordinate. This allows us to write a relation between the Eulerian and the Lagrangian coordinates of a particle at time t:

$$\mathbf{x}(\mathbf{q}, t) = \mathbf{q} + D_+(t)\,\mathbf{v}_0(\mathbf{q}) = \mathbf{q} - D_+(t)\,\nabla_{\mathbf{q}}\phi_0(\mathbf{q}) \tag{2.25}$$

where $D_+(t)$ is growth function of the perturbations in the linear regime, solution of Eq. 2.15.

Equation 2.25 defines a unique mapping between the Lagrangian and Eulerian coordinates, as long as the trajectories do not cross. This allows us to relate the density in the two set of coordinates, with the relation:

$$\rho(\mathbf{x}, t)\, \mathrm{d}^3x = \rho_0(\mathbf{q})\, \mathrm{d}^3q = \rho_0(\mathbf{q}) \left| \frac{\partial \mathbf{q}}{\partial \mathbf{x}} \right| \mathrm{d}^3x \tag{2.26}$$

where $\left| \frac{\partial \mathbf{q}}{\partial \mathbf{x}} \right|$ is the inverse of the determinant of the Jacobian of the change of coordinates. Writing the Jacobian in components

$$\frac{\partial x^i}{\partial q^j} = \delta_{ij} - D_+(t) \frac{\partial^2 \varphi_0}{\partial q^j \partial x^i} \tag{2.27}$$

and observing that, since the velocity is irrotational the deformation matrix $\frac{\partial^2 \varphi_0}{\partial q^j \partial x^i}$ can be locally diagonalized, we obtain the expression for the density in this approximation:

$$\rho(\vec{x}, \tau) = \rho_0(\mathbf{q}) \left\{ \prod_i \left[1 - D_+(t)\, \lambda_i(\vec{q}) \right] \right\}^{-1} \tag{2.28}$$

where the λ_i are the eigenvalues of the deformation matrix.

This solution tells us that, if at least one of the eigenvalues is positive (for example λ_j), the local fluid element will tend to collapse along the direction of the eigenvector relative to the positive eigenvalue, until at some time t_{sc}, when $D_+(t_{\mathrm{sc}}) = 1/\lambda_j$, the particles' trajectories overlap and the density becomes infinite. This event is called "shell-crossing" and the region in which it occurs is called a "caustic". The direction of the eigenvector with the highest-valued eigenvalue will be the first to collapse, so in general we can expect to form structures that are mostly flat, oblate or triaxial, and are sometimes called "pancakes".

The Zel'dovich approximation matches well the predictions from numerical codes (which will be described in the next section) until the moment of shell-crossing. After that, the particles simply continue moving on a straight line through the overdensity, and the caustic gets dissolved immediately after it formed.

In the real case, however, we expect the strong gravity in the overdense region to bind the particles entering it, preventing them to escape to the other side. To account for this effect, one can make an extension of the Zel'dovich approximation, adding an artificial viscosity term, that aims to simulate the effect of gravity in the vicinity of caustics. This is called the "Adhesion model" [24].

In this model, when a particle enters a high density region, the viscous term has the effect of erasing its velocity in the direction perpendicular to the caustic, but maintains the freedom to move in the other directions. Therefore, if the caustic is two dimensional (this kinds of structures are usually called "walls"), the particles will move in its plane until they reach the intersection of two planes, which is a 1-dimensional caustic (in the real world it would be a "filament"). At this point, the particles are again forced to move only in the direction of the filament, until they arrive at the intersection between (at least) two of them, forming a "node".

The adhesion model proves to be quite accurate with respect to numerical simulations for overdensities up to $\delta \sim 10$, and especially at large scales. Furthermore, it gives a simplified but informative picture for the formation of the filamentary structures of the observed cosmic web, in this sense the results from this approximate method form a sort of "skeleton" of the cosmic web, with nodes connected by filaments and walls, surrounding large underdense regions called "voids".

Cosmological Simulations

While the methods discussed so far, in particular the adhesion model, can approximate quite well the processes of structure formation in the first part of the non-linear evolution, they are not adequate to describe the highly non-linear regime that leads to the formation of clusters of galaxies, for example. To treat the full non-linear evolution of cosmic structures, we must resort to numerical simulations.

The basic principle of cosmological simulations is that it is possible to represent a region of the Universe as a box containing a large number of particles, that evolve according to the laws of gravity (and, possibly, hydrodynamics) from the linear regime to the present time. [12, p.304]

There are two big classes of simulations: N-body simulations, which treat just the gravitational interaction, and are therefore only suited for following the dark matter evolution, and hydrodynamical simulations, which include the full treatment of hydrodynamics, together with numerical recipes to treat a number of small scale effects that are too difficult to include a priori, such as, for example, gas cooling, formation and evolution of stars, different feedback mechanisms. Hydrodynamical simulations are therefore more realistic and accurate, but that comes obviously at a higher computational cost, compared to N-body simulations, which bounds the maximum size of the box feasible, once one fixes the resolution. A recent review of cosmological simulations can be found in [67].

In this work, I used the outputs of a magneto-hydrodynamical simulation from the IllustrisTNG project [45] to study the asphericity of matter distribution in and around galaxy clusters. The level of detail required by this study, so deep in the non-linear regime, and the treatment of gas physics, are currently impossible to achieve with analytical methods. More information on the simulations used for this study can be found in Chapter 3.

2.3 Galaxy Clusters

As shortly discussed in Chapter 1, galaxy clusters are the most massive gravitationally bound objects in the Universe and lie at the nodes of the cosmic web. In the hierarchical model of structure formation, they form as the result of major mergers between smaller structures [65] as well as continuous accretion of galaxies, gas and smaller groups from their outskirts, in particular through filaments, that funnel material towards the clusters [33, 56, 66]. They are therefore complex and often still evolving mixtures of dark matter, that makes up $\sim 80\%$ of the total mass, gas ($\sim 15\%$) and galaxies ($\sim 5\%$).

Observationally, the different cluster components are visible using different probes: the galaxies can be observed in the optical band, and were historically the first probes that allowed the compilation of galaxy clusters catalogues [1]. The hot intracluster gas can be seen through its thermal X-ray emission [48] or the inverse Compton scattering of CMB photons on the hot electrons, called the Sunyaev-Zel'dovich (SZ) effect [52]. The dark matter component is not directly visible, but it can be characterized through the gravitational lensing of background galaxies, that appear distorted into arcs centered on the cluster [4]. This effect is a direct probe of the total mass of the cluster, and the levels of distortion of the background galaxies can be used to reconstruct the projected mass distribution.

Clearly, the study of galaxy clusters yields important information from a cosmological point of view. As rare objects, their number density is especially sensitive to properties of the cosmological model considered, such as the matter density or the amplitude of primordial density fluctuations. Therefore, measuring it can place constraints on various cosmological parameters [47]. Additionally, the measurement of the peculiar velocity of galaxy clusters can be an important tool to study the large scale velocity field of the universe (e.g. [34]), that in turn provides an opportunity for probing the underlying mass distribution. Plus, their development with redshift lets us learn about the growth of cosmic structures, giving insights on the mechanisms of structure formation [2].

Moreover, many characteristics such as the thermal state of the gas in clusters probe both their formation mechanism and their internal physical processes, such as cooling and energy-injection feedback in case of the example [39]. Therefore, it becomes clear that galaxy clusters and their formation processes are an extremely interesting field of study from an astrophysical perspective as well. Their gravitational collapse can be seen as another example. It is driven by large the amount of dark matter and creates a deep gravitational potential well inside which gas and galaxies fall turning galaxy clusters into unique laboratories for studying the interplay of gravity and the physics of gas and plasma.

Also our own study on galaxy clusters is interesting in both perspectives. On the one hand, we look at them as complex astrophysical objects which let us investigate the impact of dense environments on cosmic gas properties. On the other hand, we see them as massive structures in the context of the underlying large scale cosmic web, exploring their geometry which is closely connected to the process of structure formation in the universe as a whole. After having outlined how we expect this process to have happened from a theoretical point of view in this Chapter, we now turn to the description of the cosmological simulation from which we drew our data.

Chapter 3

The IllustrisTNG simulation

For the analysis we used the outputs of the IllustrisTNG simulation[1] [37, 42, 44, 45, 49, 61], a suite of large volume, cosmological, gravo-magnetohydrodynamical simulations run with the moving-mesh code AREPO [60, 70]. These simulations follow the coupled evolution of dark matter (DM), gas, stars, and black holes from redshift $z = 127$ to $z = 0$; using the cosmological parameters from the Planck 2015 results [51].

The suite is composed of a series of simulations that are divided by the size of their probed volumes. Three different cubic box sizes were used: roughly 50, 100 and 300 comoving Mpc, which are referred to as, respectively, TNG50, TNG100 and TNG300. This aim of the authors was to provide complementary sets of data for different purposes: TNG300 is best suited for studying galaxy clusters, while, for example the smaller volume of TNG50 allows a mass resolution 100 times better than TNG300, making it more suited for studies focusing on galactic scales.

For this work we focused only on the largest simulation box of the set, TNG300, at redshift $z = 0$. This choice was made in order to have the largest possible sample of galaxy clusters, probing the range of masses up to $\sim 10^{15} M_{\odot}$, and have a good statistics for the analysis.

For this volume, three simulations with different resolution levels are provided, labelled TNG300-1, TNG300-2 and TNG300-3, with 1 being the highest resolution one, and the others decreasing in steps of eight of mass resolution. A comparison between these three simulations is provided in Table 3.1.

3.1 Physical Models and Numerical Methods

The purpose of a cosmological hydrodynamical simulation is to solve the coupled equations of gravity and hydrodynamics (and possibly, as it is the case for IllustrisTNG, electromagnetism) for dark matter

Table 3.1: Table of parameters for each of the resolution levels of the TNG300 set of simulations: physical volume, length of cubic box side, initial number of gas cells, number of dark matter particles, target baryon mass and dark matter particle mass in different units. Table adapted from [45].

Run	Volume $[\mathrm{cMpc}^3]$	L_{box} [cMpc/h]	$N_{\mathrm{GAS,DM}}$ –	m_{baryon} $[\mathrm{M}_{\odot}/h]$	m_{DM} $[\mathrm{M}_{\odot}/h]$	m_{baryon} $[10^6 \mathrm{M}_{\odot}]$	m_{DM} $[10^6 \mathrm{M}_{\odot}]$
TNG300-1	302.6^3	205	2500^3	7.6×10^6	4.0×10^7	11	59
TNG300-2	302.6^3	205	1250^3	5.9×10^7	3.2×10^8	88	470
TNG300-3	302.6^3	205	625^3	4.8×10^8	2.5×10^9	703	3760

[1] https://www.tng-project.org

and baryons (gas, stars and black holes) in an expanding Universe (these equations were introduced in Chapter 2, and are further detailed in [70]).

To do so, the IllustrisTNG simulations use the code AREPO[2] [60, 70], that treats dark matter, stars and black holes as particles, whereas the gas is modeled as a fluid on a grid. This code uses a tree-particle-mesh approach to solve for the gravitational interaction, which combines the very high spatial force resolution of a tree code for the short scale interactions, with the easy scalability and speed of the particle-mesh approach for the long range interactions.

On the other hand, the equations of hydrodynamics are computed using a adaptive grid refinement method, with a spatial discretization based on a fully adaptive, moving Voronoi tessellation of the simulation volume. The Voronoi mesh is generated based on a set of control points that move with the local fluid velocity. This approach allows the continuous and unrestricted adjustment of the resolution to the local clustering, while preserving the high-accuracy treatment of shocks typical of mesh codes. For example, when the gas falls into a gravitational potential well, the control points will follow it, getting closer to each other, and the cells of the mesh will automatically get smaller, increasing the resolution where it is most needed. Furthermore, the size of the cells is also adjusted so that the mass contained in them remains close to a target mass of fixed value (see Table 3.1). This fact is very important for our work, since it allows us to treat the gas in the simulation as a collection of particles, rather than a continuous field, which is a great numerical advantage, as we will see in Chapter 4.

On top of the main gravo-magnetohydrodynamical evolution, a number of sub-resolution physical models have to be introduced, which are fundamental for accounting properly for the all the astrophysical processes that are too small or too complicated to be resolved in the simulation, but affect the large scale evolution of the gas. For the IllustrisTNG simulations, we quote here an extract from [45] with a list of the models applied:

> (1) Primordial and metal-line radiative cooling in the presence of an ionizing background radiation field which is redshift-dependent and spatially uniform, with additional self-shielding corrections. (2) Stochastic star formation in dense ISM gas above a threshold density criterion. (3) Pressurization of the ISM due to unresolved supernovae using an effective equation of state model for the two-phase medium. (4) Evolution of stellar populations, with associated chemical enrichment and mass loss (gas recycling), accounting for SN Ia/II, AGB stars, and NS-NS mergers. (5) Stellar feedback: galactic-scale outflows with an energy-driven, kinetic wind scheme. (6) Seeding and growth of supermassive blackholes. (7) Supermassive blackhole feedback: accreting BHs release energy in two modes, at high-accretion rates ('quasar' mode) and low-accretion rates ('kinetic wind' mode). Radiative proximity effects from AGN affect nearby gas cooling. (8) Magnetic fields: amplification of a small, primordial seed field and dynamical impact under the assumption of ideal magnetohydrodynamics.

The details of these models are not relevant for this work, a detailed explanation can be found in [50, 69].

3.2 Cluster and galaxy catalogues

In this work, we are interested in analyzing the asymmetry of matter distribution in the environments of galaxy clusters. So, we need to extract from the simulation a catalogue of galaxy clusters, as well as the different matter components (dark matter, galaxies and gas), in and around them. Direct outputs of the IllustrisTNG simulation are halo and sub-halo catalogues. Therefore, we will fist describe how these are defined, before explaining how we obtained our set of samples from them.

[2] https://arepo-code.org

3.2.1 Halo and Sub-halo catalogues provided by the simulation

The halos are derived using a friends-of-friends (FoF) algorithm run on dark matter particles, while the other components (gas, stars, black holes) are associated to the same halo as their nearest DM particle. The FoF algorithm works by placing any two particles with a separation less than a certain linking length b in the same halo. The halos formed in this way are approximately enclosed by a density contour of about $\rho \propto 1/b^3$. Choosing b accordingly, one can, for example, tune the halo overdensities to match the values predicted by the spherical collapse model. In IllustrisTNG the choice of the linking length is $b = 0.2$.

The sub-halo catalogue is derived with the Subfind algorithm [17, 62]. It identifies locally overdense, gravitationally bound substructures inside a "parent" FoF group, considering all particle types in the calculation.

3.2.2 Extraction of the galaxy clusters and their matter components

The catalogue provides a list of properties for each halo and sub-halo. Among them are the position of the center of mass, their radius R_{200} and the total mass contained inside that radius, called M_{200}, which helped us to define our own catalogues with the objects of our interest.

To do so, we considered the halos to be galaxy groups and used the two parameters R_{200} and M_{200} as proxies for their radius and their mass respectively. In this way, we could choose the groups with M_{200} higher than a certain threshold (which was adapted during the analysis) to be part of our cluster catalogue. Thereby, R_{200} served as reference for the clusters' extent and the definition of their inner and outer regions.

The galaxies can be identified with the sub-halos and therefore taken from the according catalogue. Following [45], we selected only the sub-halos with a cosmological origin, in the sense that they formed as a result of structure formation and collapse. In fact, some of the objects in the catalogue may have formed as a result of baryonic processes (e.g. disk instabilities) inside already formed galaxies. These objects are flagged in the catalogues, and we discarded them. We decided not place a threshold in stellar mass for the galaxies, to maintain the largest possible statistics for our analysis.

Regarding the DM and Gas component around our selection of galaxy clusters, we directly extract them from the simulation snapshot. For each cluster, we selected all the particles inside a sphere of radius $\Delta \times R_{200}$ centered on the center of mass of the cluster ($\Delta = 4$ usually, but different choices are also taken, and are explained in the next chapters).

3.3 Cluster properties

In our analysis we investigated the dependence of the matter asymmetries on the cluster properties introduced in [22], namely the ellipticity, the connectivity and the relaxedness, that have been computed for the clusters of TNG300 and kindly provided by the authors for this study. They will shortly be discussed in the following.

The ellipticity allowed us to measure the anisotropy of matter distribution inside galaxy clusters. In order to compute it, we approximated the shape of the cluster with an ellipsoid in three dimensions. The parameters of the ellipsoid were fitted to the dark matter distribution with a method described in [22], until they converged to within 1%. Then, the three axes of the ellipsoid, $\lambda_{1,2,3}$ (with $\lambda_1 \geq \lambda_2 \geq \lambda_3$), and their sum $\tau = \lambda_1 + \lambda_2 + \lambda_3$, are could be used to compute the ellipticity, as defined in [30]:

$$\epsilon = \frac{\lambda_1 - \lambda_3}{2\tau} \tag{3.1}$$

With this definition, a large ellipticity parameter means that the dark matter particles have a shape that is more elongated, and thus more asymmetric.

To describe the anisotropies of matter in the outskirts of galaxy clusters we used the connectivity. It is defined as the number of cosmic filaments intersecting the surface of a sphere of radius $1.5 \times R_{200}$. These are considered to be the filaments that are connected to that cluster. This number has been computed by identifying filaments with the code T-Rex [8] using the sub-halo catalogue of TNG300, and counting the ones intersecting the sphere.

Another property of galaxy clusters that we were interested in relating to the level of asymmetries is the dynamical state. That is, whether a cluster can be considered relaxed or rather there are dynamical processes acting within the cluster (such as, for example, a merging event). To probe this property, the authors of [22] have used a parameter called "relaxedness" (first introduced by [26]). This parameter is a combination of three other parameters: the center-of-mass offset $\Delta_{\rm r}$, i.e. the distance between the center of mass of the object $r_{\rm cm}$ and the position of the peak of the density $r_{\rm c}$, normalized by the virial radius. The second parameter is the subhalo mass function $f_{\rm sub}$, which is the ratio of the sum of the masses of all subgroups inside a cluster, and the total mass of the group. The third parameter is the virial ratio, defined as $\eta = 2T/|W|$, where T is the kinetic energy and W is the gravitational potential energy of the cluster. Finally, these three parameters were combined to give the relaxedness:

$$\chi_{\rm DS} = \sqrt{\frac{3}{\left(\frac{\Delta_{\rm r}}{0.07}\right)^2 + \left(\frac{f_{\rm sub}}{0.1}\right)^2 + \left(\frac{\eta-1}{0.15}\right)^2}} \tag{3.2}$$

Clusters with $\chi_{\rm DS} > 1$ were considered relaxed.

3.4 Gas phases in IllustrisTNG

In order to get a more detailed image on the effect of the different matter components, we decided to consider not only the gas component as a whole, but to analyze separately the different phases of the gas, which can potentially highlight different structures and show different behaviours, due to the wide range of physical processes that affect the gas.

To separate the gas into phases we follow the classification of [38], which is also based on IllustrisTNG, and whose phases are found to highlight different parts of the cosmic web. These phases are identified placing cuts in temperature T and hydrogen number density n_H. These two parameters can be calculated for every gas cell from the outputs of the simulation using the following relations:

$$n_H = X_H \frac{\rho}{m_p} \tag{3.3}$$

for the number density, where X_H is the hydrogen mass fraction (~ 0.76), ρ is the cell mass density (given by the simulation) and m_p is the mass of the proton. To compute the temperature we used the internal energy u of the cells provided by the simulation:

$$T = (\gamma - 1) \cdot \frac{u}{k} \cdot \mu \cdot 10^{10} \tag{3.4}$$

where $\gamma = 5/3$ is the adiabatic index, k is the Boltzmann constant in CGS units, the factor 10^{10} is a conversion factor to get the temperature in Kelvin, and μ is the mean molecular weight, calculated as

$$\mu = \frac{4}{1 + 3X_H + 4X_H x_e} \cdot m_p \tag{3.5}$$

with X_H the hydrogen mass fraction and x_e is the fractional electron number density with respect to the total hydrogen number density (given by the simulation).

The criteria used to distinguish the phases are the following (from [38]):

- Star-forming Gas: number density $n_H > 0.13$ cm^{-3}, temperature $T < 10^7$ K and star formation rate SFR> 0.
- Halo Gas: number density 10^{-4} cm^{-3} $< n_H < 0.13$ cm^{-3} and temperature $T < 10^5$ K. This phase contains 'cool' gas associated with the Interstellar Medium (ISM) of galaxies and with the Circumgalactic Medium (CGM) observed in the halos of galaxies.
- Diffuse Integalactic Medium (IGM): number density $n_H < 10^{-4}$ cm^{-3} and temperature $T < 10^5$ K. The density cutoff selects gas at small to mild overdensities, effectively capturing the typical range associated with intergalactic gas. The temperature cutoffs selects the phase of the IGM in which hydrogen can be either neutral or ionized, but helium and heavier elements are not completely ionized.
- Warm-Hot Intergalactic Medium (WHIM): number density $n_H < 10^{-4}$ cm^{-3} and temperature 10^5K $< T < 10^7$ K. This phase has the same characteristic density of the Diffuse IGM, but the temperature cutoff is such that gas can contain a significant abundance of ionized helium and heavier elements.
- Warm Circumgalactic Medium (WCGM): number density 10^{-4} cm^{-3} $< n_H < 0.13$ cm^{-3} and temperature $10^5 K < T < 10^7$ K. Dense gas in this temperature range is more efficiently created by shock heating and feedback processes near galaxies. For this reason, we expect the cutoffs to select gas in the warm CGM of galaxies and galaxy groups, hence the 'WCGM' label.
- Hot Medium (HM): any number density nH and temperature $T > 10^7$ K. The cutoffs selects gas with temperature larger than the virial temperature of massive galaxy clusters ($M_{vir} \gtrsim 10^{14} M_\odot$). For this reason, we are selecting gas that has been shock heated to these high temperatures in (and near) the most massive dark matter halos in the universe.

In Figure 3.1 we show the phase diagram T over n_H of the gas particles in TNG300-3, together with the regions corresponding to the various phases we identified before, and in Table 3.2 are presented the relative number of gas cells in the various phases. As we can see, the WHIM is the phase taking the largest fraction of the total gas, with more than half of the cells, followed by the diffuse IGM. According to [38], at $z = 0$ the most prevalent phases in galaxy clusters are the Hot Medium, due to shock-heating, and, secondly, the WHIM. The latter is also found to be the main gas component in filaments, while the diffuse IGM is predominant outside those regions, so in sheets and voids.

Table 3.2: Relative number of gas cells in the different phases in TNG300-3.

Phase	Relative number of cells
Star-forming gas	1.82×10^{-4}
Halo gas	0.013
Diffuse IGM	0.37
WHIM	0.52
WCGM	0.02
Hot Medium	0.07

For this reason, in our analysis we concentrate mainly on the Hot Medium and the WHIM phases, that are the ones that make up almost the entirety of the gas in the regions of interest, i.e. in the environments of galaxy clusters.

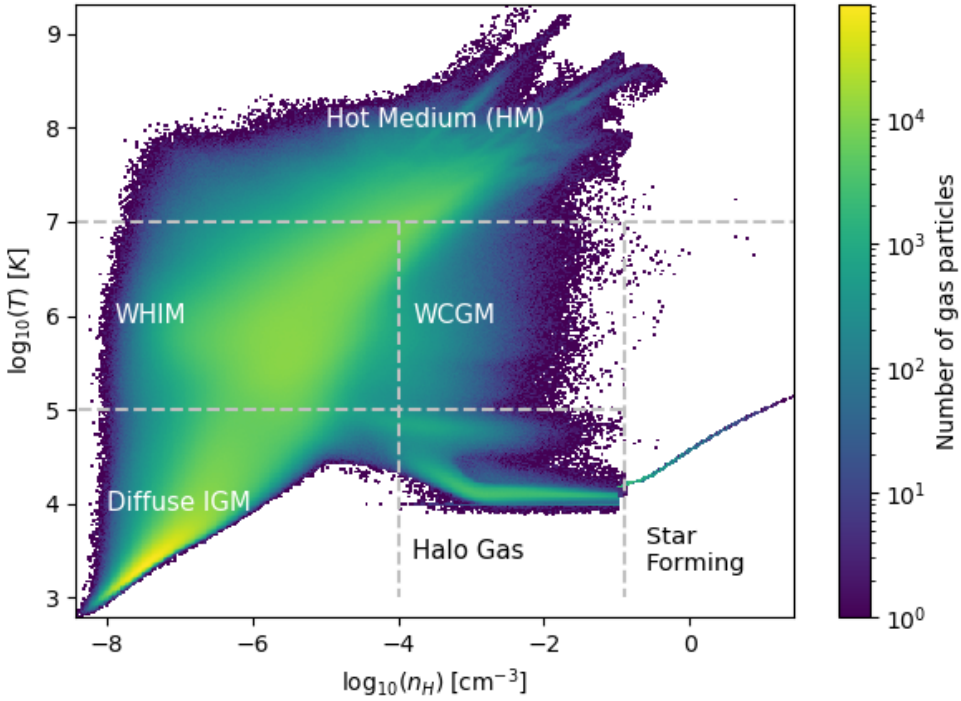

Figure 3.1: Phase diagram (T, n_H) of the gas particles in TNG300-3, with different phases higlighted following [38].

Chapter 4

Methods

The aim of this project, as we introduced before, is to probe how different matter components (gas, DM, galaxies) are differently distributed in galaxy clusters' enviroments. Beyond the radial matter distribution, that has been extensively probed in the past [9, 18, 29, 32, 36, 43, 46, 54], exploring the azimuthal matter distribution of cluster environments is becoming a powerful method to quantify any departure from spherical symmetry from the shape of clusters up to their connected cosmic filaments, so we decided to explore further in this direction.

To achieve this we used two methods, that we will present in this Chapter: the first is the "harmonic power excess" method (developed in [23]), and the second exploits a new set of parameters that we call the "β parameters" (partly inspired by the work of [66]). Both methods are based on the "aperture multipole moments" method, a 2-dimensional harmonic decomposition of the projected matter distribution, that was first introduced by [58] in the context of weak lensing. It was later used, for example, to determine the ellipticity of galaxy clusters [10, 59] (from the quadrupole moment, $m = 2$ in Fig. 4.2), but also to detect filamentary structures inside clusters [40], or a bridge of matter between two clusters [16]. In addition, the authors of [21] have used multipole moments of the galaxy distribution to measure the harmonic signature of cosmic filaments around clusters comparing recent galaxy surveys to state-of-the-art simulations.

We chose to investigate the 2-dimensional, projected matter distribution, rather than the full 3-dimensional distribution, due to the observational properties of the matter components we considered. Indeed, almost all the observational probes that are used to study galaxy clusters do not give any information on the distribution of the source along the line of sight. For dark matter, the effect of weak lensing is used, but with it it is possible to reconstruct only the projected matter density field. For the hot gas observables, namely x-rays and the Sunyaev-Zel'dovich effect, the quantities we are able to measure, the flux and the Compton-y parameter respectively, are both integrated along the line of sight. Only the galaxy observations can in principle yield information on their 3-dimensional distribution, if we obtain an accurate estimate of their redshift. Unfortunately, precise and accurate redshift estimations can be obtained with a spectroscopic measurement of the spectrum of the galaxy, which is observationally time consuming. Therefore, if we want a large number of galaxies, like in our case, we need to use also galaxies with redshift measured using a photometric approach, which is not precise enough to resolve the 3D distribution inside a cluster.

4.1 Aperture multipole moments

Any function of the polar angle ϕ, $f(\phi)$ can be decomposed in multipole moments Q_m through an harmonic decomposition of the form:

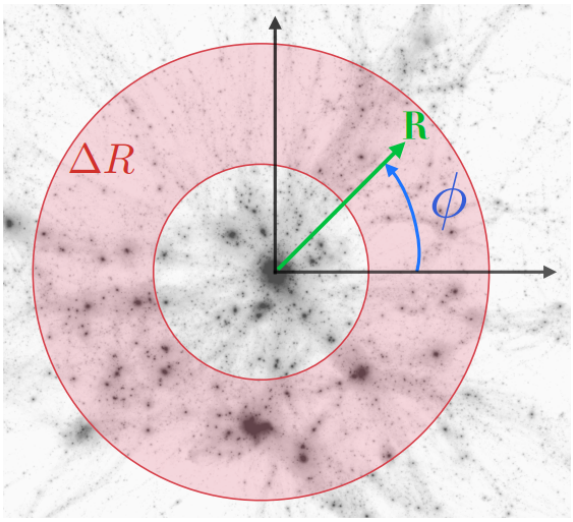

Figure 4.1: Illustration of the polar coordinate system (R, ϕ) and a example of radial aperture ΔR for projected matter distribution centred on a simulated galaxy cluster from the Illustris simulation (picture taken from [21]).

$$f(\phi) \propto \sum_{m=0}^{\infty} Q_m \, e^{im\phi} \tag{4.1}$$

Aperture multipole moments are defined as the coefficients of the harmonic decomposition of a surface density field $\Sigma(R, \phi)$ integrated along the radial direction in an annulus called the "aperture", using the equation:

$$Q_m = \int_{\Delta R} R \, \mathrm{d}R \int_0^{2\pi} e^{im\phi} \, \Sigma(R, \phi) \; \mathrm{d}\phi \tag{4.2}$$

where Σ is the surface density field, and it is integrated using the polar coordinates (R, ϕ) in the projected plane, weighted by a complex exponential depending on m, which is the multipolar order. The radial aperture is denoted by ΔR. An optional radial weight function can also be applied[1], but we will not do it here. An example of a possible aperture is shown in Fig. 4.1, together with an illustration of the coordinate system.

Therefore, the aperture multipole moment of order m measures the "degree of similarity" between the matter distribution we are considering in that aperture and the distribution associated with the order m, some of which are shown as an example in Fig. 4.2. As we can see from Fig. 4.2 the number of the multipole is connected to the angular scale of the structures in the matter distribution. We also point out that the Q_ms are in general complex numbers.

If we consider a discrete distribution of particles, which is the case for all the matter components we will analyze in this work (with the approximation for the gas described in Chapter 3), then the surface density can be written as a sum of Dirac deltas:

$$\Sigma = \sum_j M_j \, \delta_D(R - R_j) \tag{4.3}$$

[1]Indeed, a radial weight can be used to optimize the signal to noise ratio when computing multipole moments on direct observations (such as on gravitational lensing map in [58]).

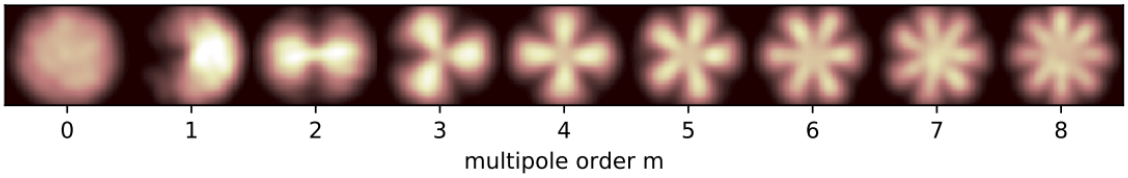

Figure 4.2: Graphical depiction of the distributions associated with first eight multipolar orders of the harmonic decomposition. Figure taken from [21].

Furthermore, if the masses of the particles are all equal, which is true for dark matter and (approximately) for the gas particles, we can safely ignore it, as it becomes just a normalization factor common to all multipoles[2]. So, inserting this result in Eq. 4.2 the expression for the multipoles simplifies greatly:

$$Q_m = \sum_{j, R_j \in \Delta R} e^{im\phi_j} \tag{4.4}$$

This is the formula we used to compute multipole moments throughout our work.

To compute the aperture multipole moments in the environment of galaxy clusters for this work, we place the center of the coordinate system on the center of mass on each cluster, and we consider two apertures: one that identifies the cluster's inside, while the second probes its outskirts. The radial limits of the apertures are chosen to be a fixed multiple of the R_{200} radius of each cluster, this allows us to compare the results between clusters with different masses and dimensions.

4.2 Harmonic power excess

The harmonic power excess [21,23] is a statistical estimator based on the aperture multipole moment decomposition, that compares the asymmetries of matter distribution around galaxy clusters with respect to the background matter distribution. It is defined as the ratio between the average harmonic power spectrum centered on clusters and the same quantity computed on random positions:

$$\widetilde{Q_m} = \frac{\left\langle |Q_m^{cluster}|^2 \right\rangle}{\alpha \left\langle |Q_m^{random}|^2 \right\rangle} \tag{4.5}$$

We will now explain each of the quantities on the right hand side separately.

The quantity $\left\langle |Q_m^{cluster}|^2 \right\rangle$ is the average of the square moduli of the aperture multipole moments of order m, centered on galaxy clusters, and we call it the "harmonic power" (we also call "harmonic power spectrum" the collection of $\left\langle |Q_m|^2 \right\rangle$ for all orders). We considered this quantity instead of the simple Q_ms because the asymmetries we are interested in identifying, in particular the ones related to the cosmic filaments in the clusters' outskirts, have generally a low density contrast with respect to the background. Moreover, different clusters can have wildly different harmonic power spectra, depending on the specific configuration of matter. For these reasons, we are interested in the mean multipole moments, averaged over all the clusters, to highlight the average level of asymmetries around them. But, given that the multipole moments are in general complex, averaging them directly would just symmetrize the result, erasing the information contained in the phase of the Q_m, since the clusters have random orientations and we do not align them. For this reason, we first take the square modulus

[2] This fact is not true for galaxies, but we will ignore their mass nonetheless, since we treat them as tracers of the total density field, following [21]

$|Q_m|^2$, the power of the multipole for each order, and we average them over all clusters, preserving all the relevant information.

Moreover, to obtain a large statistics, we first projected each cluster along the three axes of the simulation box, and we computed the multipolar decomposition for each projection, thus effectively multiplying by 3 the number of clusters we analyzed. So in the end we obtained the quantity:

$$\left\langle |Q_m^{cluster}|^2 \right\rangle = \frac{1}{3N_{clusters}} \sum_i^{N_{clusters}} (|Q_m^{i,x}|^2 + |Q_m^{i,y}|^2 + |Q_m^{i,z}|^2) \tag{4.6}$$

To compare harmonic power around clusters with the background density field, the same quantity $\left\langle |Q_m^{random}|^2 \right\rangle$ was also computed around random locations in the simulation box. For each one of these position an R_{200} is randomly assigned from the cluster catalogue, to probe an equivalent set of regions. This procedure allows us to highlight the filamentary patterns near clusters that are in excess with respect to the overall large-scale structures [21].

Finally, the factor α is introduced to account for a boost of harmonic power, independent on m, that was found to happen in galaxy clusters during the collapse, due to the tidal contraction of density fluctuations, as explained in [23, Sec. 2.3]. As detailed there, this effect is regarded as a first-order change of multipole powers of clusters with respect to the background, while we are interested in the second-order effect due to the non-linear collapse and the effect of the filamentary structures. That is why we take the ratio between $\left\langle |Q_m^{cluster}|^2 \right\rangle$ and $\alpha \times \left\langle |Q_m^{random}|^2 \right\rangle$.

From a practical point of view, the α factor is computed, following [21], as the ratio of the average multipole powers of clusters and random positions, above a certain threshold th, set where both curves reach their asymptote:

$$\alpha = \frac{\left\langle \left\langle |Q_m^{cluster}|^2 \right\rangle \right\rangle_{m>th}}{\left\langle \left\langle |Q_m^{random}|^2 \right\rangle \right\rangle_{m>th}} \tag{4.7}$$

This method has been successfully applied to the dark matter [23] and galaxy distributions [21] in clusters' environments. What we will do in this work is to reproduce the analysis done on the galaxy distribution, to confirm the results of [21], and then to apply the method for the first time to the gas distribution in IllustrisTNG.

4.3 Beta parameters

To answer the second question underlying our research, that we presented in the Introduction (Chap. 1), on how the asymmetries in the matter distribution are correlated to the properties of clusters, we decided to introduce new estimators for the level of departure from spherical symmetry.

We call these estimators the β parameters (taking inspiration from [66]). They are also based on the aperture multipole moment decomposition. We define these parameters as

$$\beta_m \equiv \sqrt{\frac{|Q_m|^2}{|Q_0|^2}} \tag{4.8}$$

representing the amount of asymmetry of the matter distribution in the order m, $|Q_m|^2$, with respect to a spherical distribution, represented by the power of the order 0, $|Q_0|^2$.

In the spirit of simplifying the analysis and the interpretation of the results, while still keeping the most relevant information from the multipole decomposition, we decided to concentrate only on the multipole orders that are expected to be the leading ones in the decomposition, thus containing most of the information on the asymmetries. We chose these orders to be $m = 2, 3, 4$, leading to the parameters β_2, β_3 and β_4.

As for the previous method, for each cluster we took the three projections along the axes of the simulation box. We then computed the three β parameters for each projection in different apertures and related these results with the cluster parameters as introduced in Section 3.3.

Chapter 5

Harmonic power excess of the galaxy distribution

In the first part of the project we applied the aperture multipole moments method introduced by [23] and explained in Chapter 4 on the simulation data of IllustrisTNG300 (introduced in Chapter 3).

In this Chapter, we focus on the galaxy distribution in and around galaxy clusters, from the low-resolution simulation TNG300-3 and the high-resolution simulation TNG300-1. Previously, the authors of [21] have estimated the galaxy multipole moments on the magneticum simulation and on galaxy observation (WISExSCOSMOS survey [5]). The comparison of our analysis with the study of [21] will be thus discussed later in this Chapter.

5.1 Method and choice of parameters

5.1.1 Selection and decomposition of the clusters

From the halo catalogue of the TNG300 simulations we selected the Groups with mass $M_{200} > 10^{14}\ M_{\odot}$ as our galaxy cluster sample. As shown in Fig. 5.1 which depicts the average number of galaxies per halo for different mass bins, the selected clusters have more than a 1000 galaxies on average while the halos with mass $\sim 10^{12}\ M_{\odot}$ contain only around 10 galaxies. Due to this selection we obtain 202 clusters from TNG300-3 and 216 cluster from TNG300-1 which form the cluster catalogues used for the computation.

To compare the inner parts with the outskirts of the clusters, we chose two different radial apertures. For TNG300-3 and the comparison with TNG300-1 we used the intervals $[0-1.5]R_{200}$ and $[1.5-4]R_{200}$ in order to have a large enough number of galaxies in the inner annulus, while we changed the separation for the final analysis with TNG300-1 to $[0-1]R_{200}$ and $[1-4]R_{200}$. This last choice resulted in a better differentiation of the behaviour regarding the inner parts of the clusters and their surroundings considering that $R_{200} \simeq R_{vir}$.

Having selected the clusters and according galaxies, the next step of the procedure consisted in the projection of the galaxies along the three axis of the simulation. As an example Fig. 5.2 shows a projection of the dark matter particles inside $5 \times R_{200}$ around three random clusters from TNG300-3 together with the positions of the galaxies in the same region associated with the cluster. Finally we calculated the multipolar moments decomposition for each projection using Eq. 4.4. The resulting average harmonic decomposition of the clusters will be discussed further in the next sections.

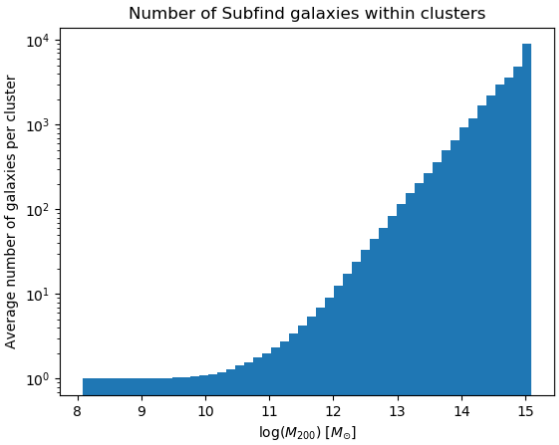

Figure 5.1: Average occupation number of galaxy clusters in TNG300-1 as function of their M_{200}.

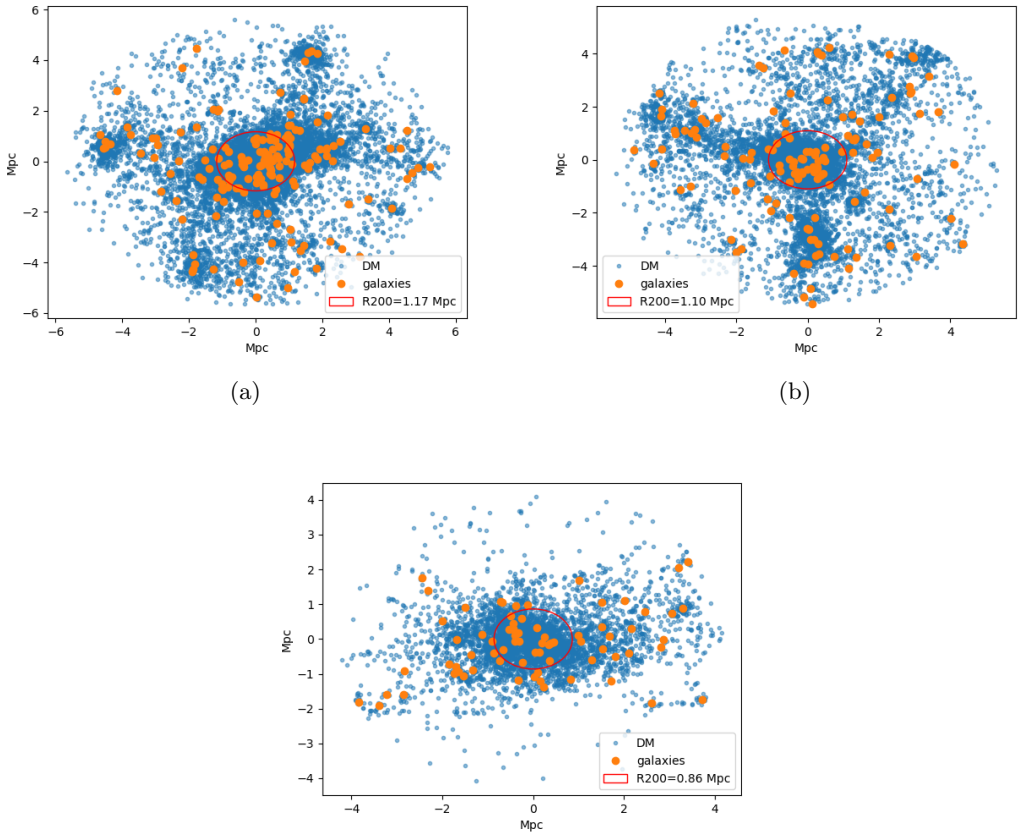

(a) (b)

(c)

Figure 5.2: Three examples of clusters from the TNG300-3 simulation. Here we show the dark matter particles (in blue) and the galaxies (in orange) selected in a sphere of radius $5 \times R_{200}$ centered on the cluster and projected along the z axis for three randomly selected clusters. The red circle has a radius of $1 \times R_{200}$.

5.1.2 Masking of the background density field

In order to determine the background harmonic power, we drew ten times as many random positions as the number of clusters across the whole simulation volume, and for each random position we selected randomly an R_{200} from the cluster catalogue. Then we considered all galaxies inside the same annuli as chosen for the inner and outer parts of the clusters around the random positions. The resulting average harmonic decompositions of the background for Illustris-TNG300-3 are shown as red and green curves in Fig. 5.3(a).

Figures 5.3(c) and 5.3(d) which present the final individual results for the clusters and the random positions in linear and logarithmic scale additionally take the factor α according to Eq. 4.7 into account. Thereby Fig. 5.3(b) serves as justification for choosing a threshold at $m = 15$ for the calculation of α because it shows how the gradient of the clusters' multipoles goes approximately to zero after $m \sim 13$.

In Fig. 5.3(d) we can observe some harmonic powers of the random positions exceeding the ones computed around the clusters. This is an unwanted effect due to random positions being chosen near or inside clusters. In this way part of the cluster's power is incorporated in the random harmonic profile artificially increasing the background power. In order to remove those contaminations, we introduced a mask on the clusters when choosing the random positions.

All the regions inside $6R_{200}$ around the clusters were masked and therefore excluded during the selection process. This choice of radius was made because the mask is removed during the multipole analysis of the background. In this way we ensure that even if a random position is drawn very close to the mask, the central region of the cluster falls outside the circle of radius $4R_{200}$ around the random position. Therefore the chosen annuli lay outside the clusters.

In order to have more control over the effect of this action, only the clusters with mass above a certain threshold are masked. The choice of the threshold depends on the average number of galaxies per cluster as function of the cluster mass, as well as the computational time needed to complete the calculations.

Fig. 5.3(e) and 5.3(f) present the comparison between two different masks implemented in the analysis of TNG300-3: on the left only the more massive clusters (with $M_{200} > 10^{14} M_{\odot}$) are excluded, while on the right all clusters are masked. In both figures we can see that the harmonic power spectra of the clusters and random positions for the inner region agree much better with each other for $m > 5$ due to the masking. Thereby the difference of the two masks seems small considering the shape of the multipole powers.

However, the second mask increases the relative amplitude of the clusters' multipoles with respect to the random positions. The effect is greatly amplified in the higher resolution simulation where the number of galaxies is much higher. This can be seen in Fig. 5.4 which compares the results obtained from TNG300-3 and TNG300-1. Therefore we decided to set the limit for the clusters to mask at $10^{12}\ M_{\odot}$ regarding the final results with the high resolution simulation. In this way we could ensure to exclude the relevant clusters from contaminating the random profiles while not masking them all which would result in much longer computation times.

5.1.3 Calculation of the harmonic power excess

Finally the harmonic power excess could be calculated by dividing the harmonic power of the galaxies inside the clusters by the harmonic power of the background using Eq. 4.5 with α from Eq. 4.7 setting $th = 15$. In addition we evaluated the mean and median multipole order (weighted by the harmonic power excess) which represent the average angular symmetry in the projected 2D galaxy distribution.

To obtain a statistical error on the harmonic power spectrum, we applied bootstrap re-sampling on

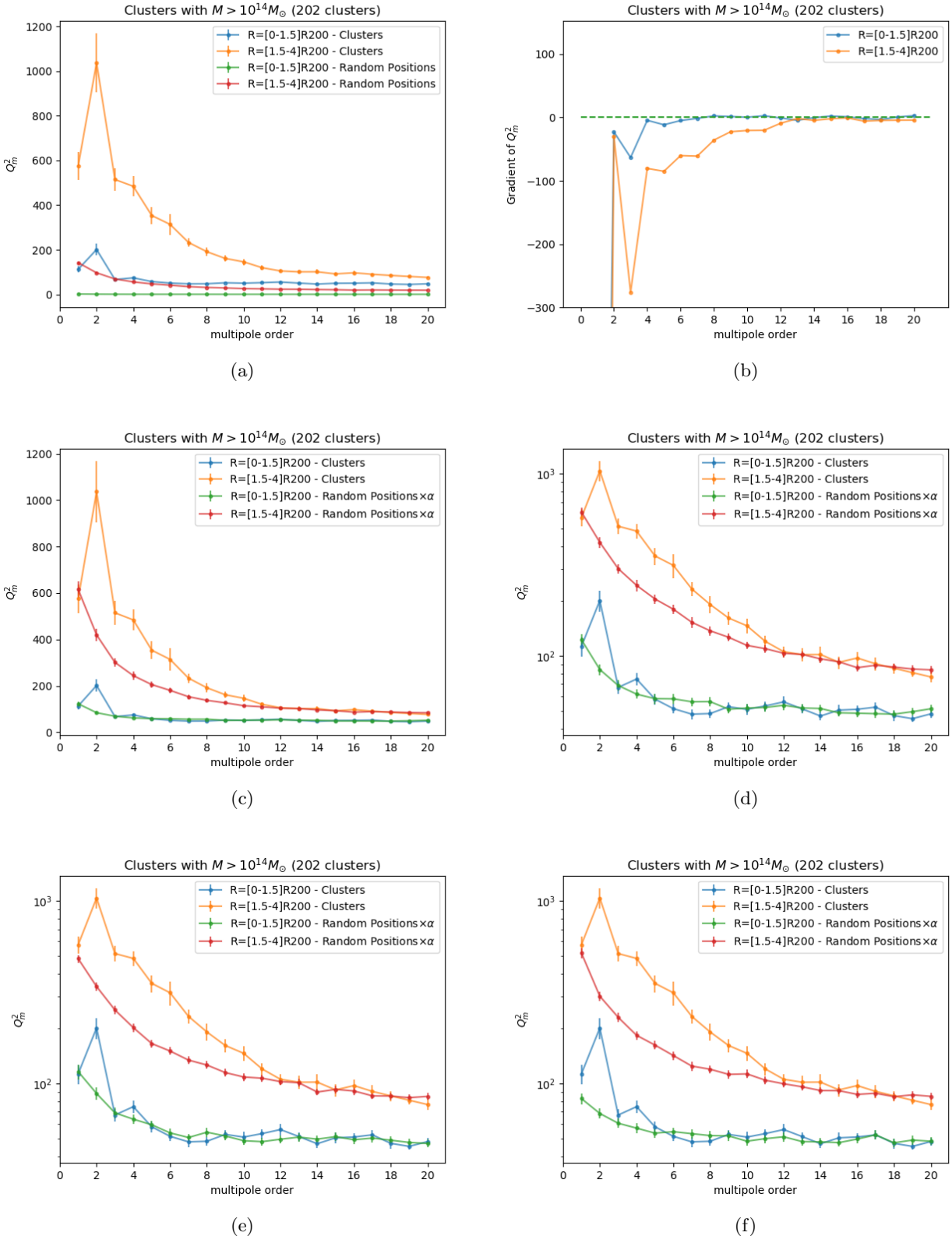

Figure 5.3: Multipole analysis of galaxy distribution around clusters with $M_{200} > 10^{14}$ $M_\odot$ in TNG300-3 for two apertures: $R = [0 - 1.5]R_{200}$ (blue) and $R = [1.5 - 4]R_{200}$ (orange). (a) clusters' and randoms' multipole powers (b) gradient of the clusters' harmonic power spectrum (c & d) same as (a) with background harmonic power spectrum multiplied by the factor α in linear and logarithmic scale (e & f) same as (d) with masking on the clusters with $M_{200} > 10^{14}$ $M_\odot$ (left) and on all the clusters in the simulation catalogue (right).

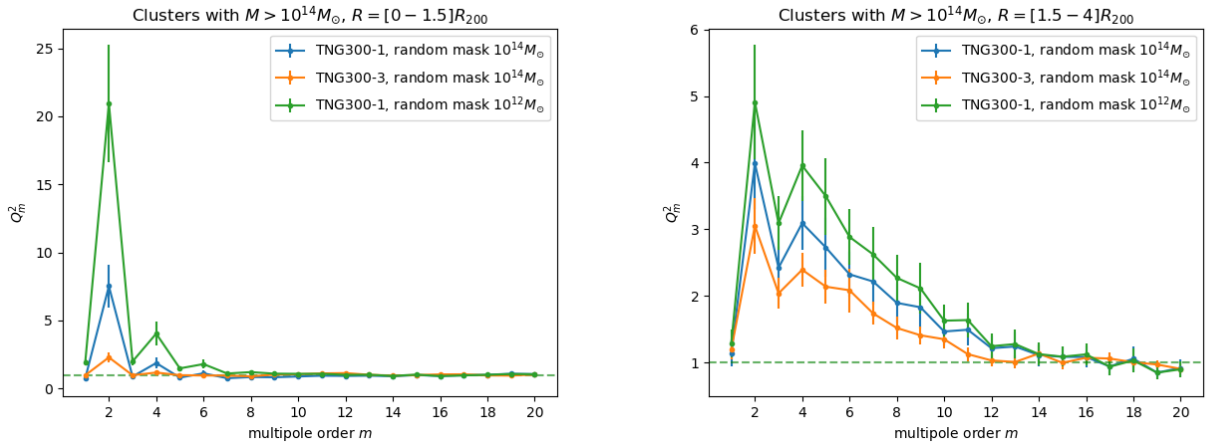

(a) (b)

Figure 5.4: Comparison of harmonic power excess between TNG300-3 and TNG300-1 simulations in the inner (left column) and outer (right column) aperture.

the cluster and random multipoles. Out of the N cluster and random multipole profiles, another N profiles were randomly selected where replacement was allowed. Then the harmonic power excess was computed for all resampled sets. This procedure was repeated 1000 times. In this way we obtained the average harmonic power excess and its error from the 1000 bootstrapped samples. The results are presented in the next section.

5.2 Results

5.2.1 Comparison of low and high resolution results

The low resolution simulation TNG300-3 served as example data when implementing and adapting the aperature multipole moments method for the purposes of this thesis project. The results which were already partly presented in the last section confirmed the good functionality of the code. After the successful completion of the analysis, we repeated it with the high resolution simulation which implies a larger statistics for the multipoles analysis.

Fig. 5.4 shows the comparisons between the two simulations for the two radial apertures $[0-1.5]R_{200}$ and $[1.5-4]R_{200}$ as discussed in the previous section. It can be seen how the higher resolution greatly increases the harmonic power excess inside clusters. This is mainly due to a much larger number of galaxies in this simulation. The clusters in TNG300-1 contain on average ~ 1560 subhalos, compared to the only 45 in TNG300-3. For the outskirts of the clusters we still see an improvement (of about 30% for the $m = 2$ peak) up to multipole order of $m = 15$, but less substantial than for the inner cluster regions. As the analysis of TNG300-1 provides a more significant harmonic signature (due to the larger number of galaxies) we decided to use that as final result for the comparison with the previous findings.

5.2.2 Comparison of TNG300-1 and previous results

Harmonic power excess

The final results of the galaxy harmonic decomposition analysis are shown in Fig 5.5. In the inner region of the clusters the power excess shows a high peak at $m = 2$, which corresponds to the quadrupole order. This feature implies that the projected shape of the clusters is elliptical on average.

Beyond the dominant quadrupolar term, we see that the harmonic power of the clusters converges quickly to the one computed around random locations for m larger than ~ 7. The only other significant excess is found for $m = 3, 4$ suggesting a low level of asymmetry or substructures in the galaxy distribution.

Turning to the outer region with $R = [1 - 4]\ R_{200}$, we see a significant difference with respect to the inner one: the highest peak is still at $m = 2$, but it is lower than in the previous case, and there is a larger power at all orders until $m \sim 14$. This shape of the power spectrum indicates a more complex asymmetry in the distribution of galaxies, hinting at the presence of filamentary structures connecting the clusters with the rest of the Cosmic Web.

These two main results are in strong agreement with [21]. As shown in Fig 5.6, they found also both: a strong quadrupolar excess inside clusters, and a more complex harmonic signature at cluster peripheries. Their results have been estimated from both Magneticum simulation (green) and for observed galaxy distribution (black). In their case, observational issues have been take into account such as the selection of galaxy (only massive/luminous galaxies have been selected to match with observation). This selection of galaxies could explain the relative difference between our amplitude of harmonic power excess ($1 < Q_m < 15$) and their results ($1 < Q_m < 12$).

Mean and median angular scales

When computed on the outskirts of clusters, the mean and median angular scales are a way to estimate the average number of filaments connected to the clusters (as explained in [21]). Fig. 5.7 presents our results for $R = [1 - 4]\ R_{200}$.

The first two panels show the distributions of the means and medians of the 1000 bootstrapped samples. These distributions look approximately normal, although the median is slightly more skewed. This justifies the fact that we took the standard deviation of the sample as the error on the average of the mean and median multipole order.

In Fig. 5.7(c) the mean and median are identified on the original power excess with values $m_{mean} = 4.94 \pm 0.19$ and $m_{median} = 3.87 \pm 0.17$. The difference in the numerical values comes from the fact that the power excess is highly asymmetric, and the mean tends to be more sensitive to this, while the median is less affected by skewed distributions as estimator of the central value. These results are quite compatible, though a bit higher, than the ones in [21], quoted in Fig 5.6. This small difference must be due to the selection of galaxies which is applied in [21] and not in our work.

5.3 Conclusions

In this Chapter we analyzed the asymmetries in the distribution of galaxies in and around galaxy clusters from the TNG300 simulations. We used the harmonic power excess to highlight the differences in the harmonic power spectrum of clusters compared to the background density field. From the this analysis we found that:

- In the inner regions of clusters (inside R_{200}) only the quadrupole has a high power excess, which suggests that the projected galaxy distribution is elliptical on average (in accordance with other studies [21, 35]).
- In the outer regions (up to $4R_{200}$), the power excess is distributed on larger orders, pointing towards the presence of filamentary structures in the galaxy distribution around clusters, consistently with what found in [21]. Moreover, from the mean and median angular scales we expect to find an average number of filaments between 4 and 5 connected to the clusters.

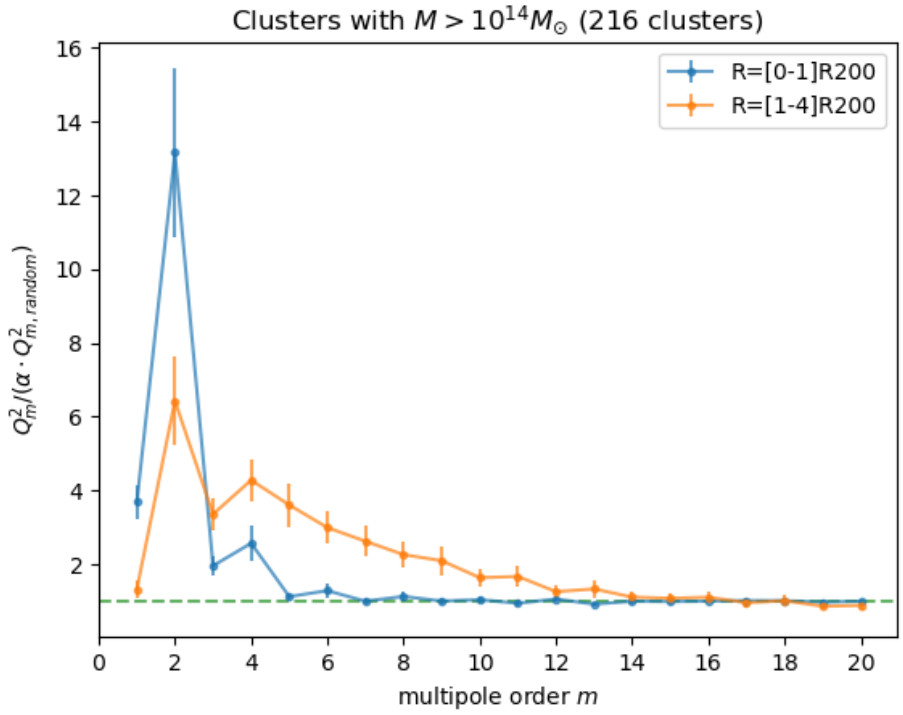

Figure 5.5: Harmonic power excess of galaxy distribution around clusters with $M_{200} > 10^{14}\ M_\odot$ in TNG300-1, for two apertures: $R = [0-1]R_{200}$ and $R = [1-4]R_{200}$.

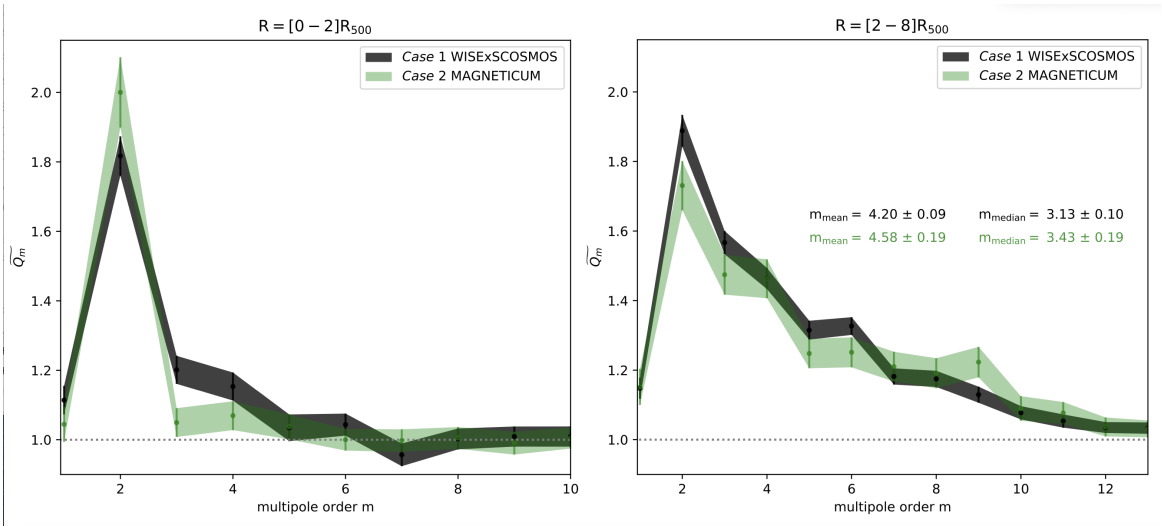

Figure 5.6: Harmonic power excess in the inner (left panel) and outer (right panel) regions of galaxy clusters, computed using the Magneticum simulation (green) and real data (black). Figure taken from [21].

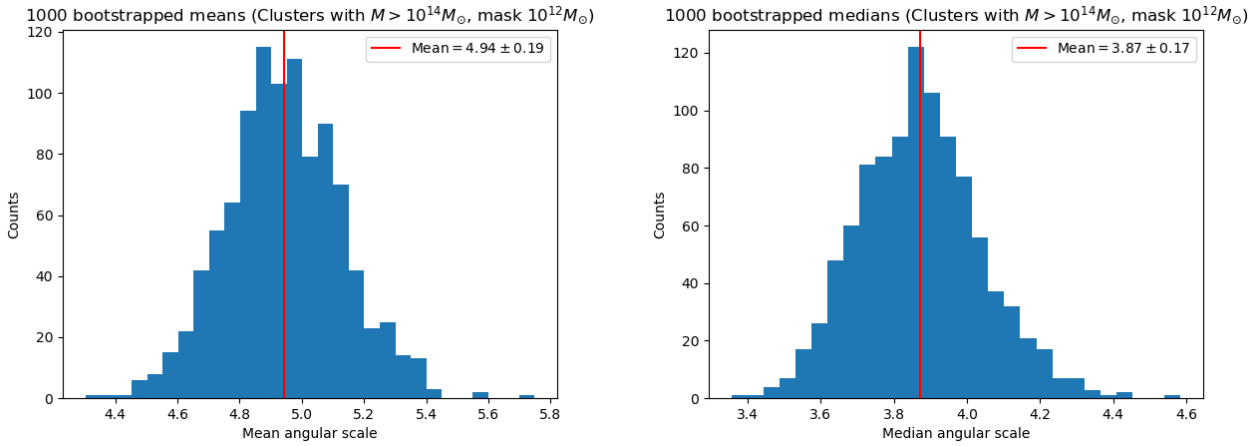

Figure 5.7: Mean and median multipole orders of the harmonic power excess in the outskirts of clusters, $R = [1 - 4]\ R_{200}$. (a & b) distribution of the mean and median multipole orders for 1000 bootstrap samples (c) final estimate of the mean and median superimposed to the harmonic power spectrum.

Chapter 6

Harmonic power excess of the gas distribution

In the second part of the project we applied the aperture multipole moments method on the gas distribution of the low resolution simulation TNG300-3 (for computational reasons). This is the first time this method is applied on gas. So far, it had only been applied on galaxies and dark matter in simulations [21,23].

Studying the distribution of gas in galaxy clusters' environments is important to have a better understanding of the processes that lead the collapse of baryonic matter into clusters. This is not so easy to achieve with observational data, due to the faint signal that gas produces, especially in the outskirts of clusters and in filaments. Indeed, the gas phase in filaments is expected to be less hot and dense compared to hot plasma in cluster central regions ([20]). In fact, only few individual detection of massive gas filaments have been made based on X-ray or Sunyaev-Zel'dovich (SZ) effect (for example [7,63,64]). Recently statistical methods based on staking SZ or X-ray observations from filaments are thus developed to improve the detectability of gas filaments ([63,64]).

In this Chapter, our aim is to understand whether the gas traces the filamentary structures in the cosmic web in the same way as galaxies; and if so, which gas phase introduced in section 3.4 traces them better.

6.1 Analysis on the total all gas

We started the harmonic analysis of the gas distribution centered on galaxy clusters considering all the gas cells, without putting any threshold in temperature or density. We considered the same parameters used previously for the galaxy distribution analysis, that are: two apertures at radii $[0-1]R_{200}$ and $[1-4]R_{200}$, clusters with mass $M_{200} > 10^{14}\ M_{\odot}$, and a mask on all the groups identified by the simulation when computing the harmonic spectra of the background gas distribution.

6.1.1 An unexpected result

In Figure 6.1 the results of this first analysis are shown. We can immediately notice the stark difference between this plot and the one in Fig. 5.5, especially looking at the inner aperture. This one shows a lot of power at all orders until $m = 16$, looking almost like a power law, which is in contrast with all our expectations, that predicted a high quadrupolar peak and a sharp drop of power excess, going to 1 between $m = 5$ and 10. An additional problem can be seen focusing on the highest orders surveyed ($m = [18, 20]$). We can see a consistent lack of power in the cluster decomposition compared to the random one, where, instead, a match of the two is expected at high orders [21,23].

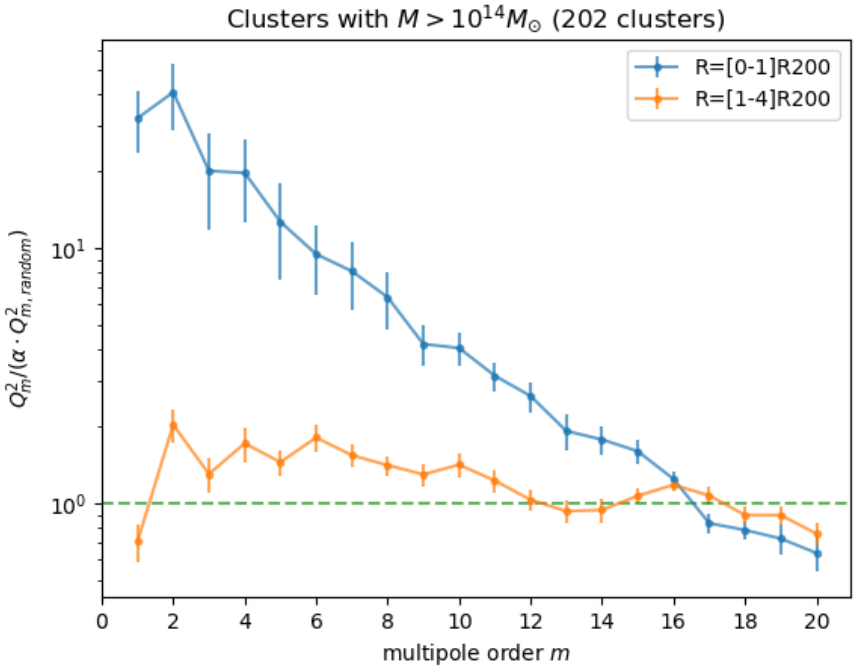

Figure 6.1: Harmonic power excess of gas distribution around clusters with $M_{200} > 10^{14}\ M_\odot$ in TNG300-3, for two apertures: $R = [0-1]R_{200}$ and $R = [1-4]R_{200}$.

Also the profile of the outer power excess is quite unexpected. The first thing which can be noticed is that there is no clear peak at $m = 2$, and instead the power of the orders $m = 2, 4$ and 6 is approximately the same. Looking at the full curve we can see how it fluctuates around the same value until around order 7, and then slowly decreases, going to 1 at $m = 12$.

Both these results are puzzling and difficult to interpret, so we decided to perform a series of tests to check if the behaviours shown here were caused by a particular choice of parameters or some kind of error in the analysis.

6.2 Testing the anomalous results

6.2.1 Enlarging the inner radial aperture

The first idea we had was that the reason of the unusual inner power excess of Fig. 6.1 could be due to the fact that we were probing an area too small to capture well the elliptical shape we were looking for, since the cluster gas might spread more outwards than the galaxies do. So we decided to change the two apertures to $[0-2]R_{200}$ and $[2-4]R_{200}$, keeping the rest unchanged.

The results are shown in Fig. 6.2(a). There are no appreciable differences in the shape of the inner power excess, while for the result in the outer region it seems that the power of the random positions has increased compared to the one computed around the clusters. This makes the power excess compatible with 1 at low orders, worsening the problems described in the last section. Clearly the larger spread of the gas is not the reason for the behaviours we saw in Fig. 6.1.

6.2.2 Stacking random positions

A second test was made stacking the projected 2D positions of the gas particles collected around random locations, with the aim of testing if the lower number of particles in random profiles affected

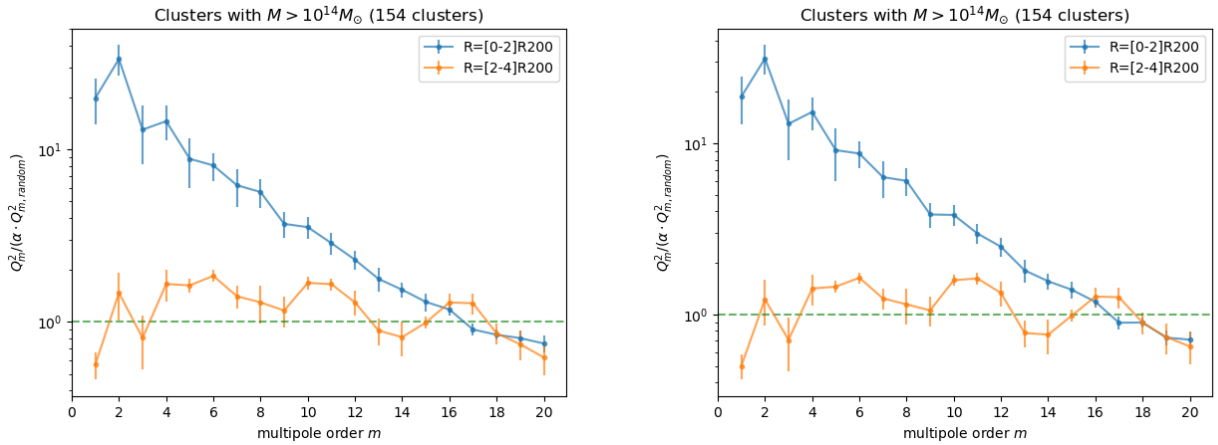

(a) (b)

Figure 6.2: Harmonic power excess of gas distribution around clusters with $M_{200} > 10^{14}\ M_\odot$ for the apertures: $R = [0-2]R_{200}$ and $R = [2-4]R_{200}$. (a) using the standard procedure, (b) stacking random positions.

the average result. So, starting from the results of the previous test, we decided to stack the random positions in groups of 20, so to have $\sim 400 \times 3$ random profiles with more particles each, instead of the $\sim 8000 \times 3$ of the previous test.

The results are presented in Fig. 6.2(b), and from quick comparison with the Figure on its left one can already tell that the test was unsuccessful. Indeed, this Figure shows no real difference from the previous one, signaling that the results are nearly independent of the stacking procedure.

6.2.3 Extending the analysis to higher orders

Trying to address the lack of power excess at high orders in the inner aperture, we decided to extend the multipole analysis to higher orders, up to $m = 30$, and to plot also the unnormalized cluster powers superimposed to the random powers multiplied by the α factor, to have a clearer view of their respective relation.

In Fig. 6.3(a) and 6.3(b) we see the results of this analysis using the same threshold as before to compute α, namely $th = 15$ (so in this case the average in Eq. 4.7 is done on the orders $m = [15-30]$). As we can see there is indeed a matching problem between the cluster and the random harmonic powers, which is small but noticeable in the outer region, while in the inner one the two curves really diverge, an additional sign that something is not quite working as expected.

To account for this problem we decided to shift the threshold for computing α from order 15 to order 20, the results being shown in Figures 6.3(c),6.3(d). From there we see a much better agreement especially for the power excess in the outskirts of clusters, it now averages to 1 from $m = 18$ onward. Also in the inner region the cluster and the random spectra agree better, although there is still an inconsistency at very high multipoles. In conclusion, the modification has the general effect to shift upwards the power excess curves, partly but not fully solving the issue.

6.2.4 Decreasing the masked regions

Continuing to focus on the apparent mismatch between the random harmonic powers and the cluster ones in the central cluster region, we turned to reconsider their mask. One hypothesis was that we were masking too many structures when computing the multipole moments around random locations, and thus it may have affected the steepness of the spectrum.

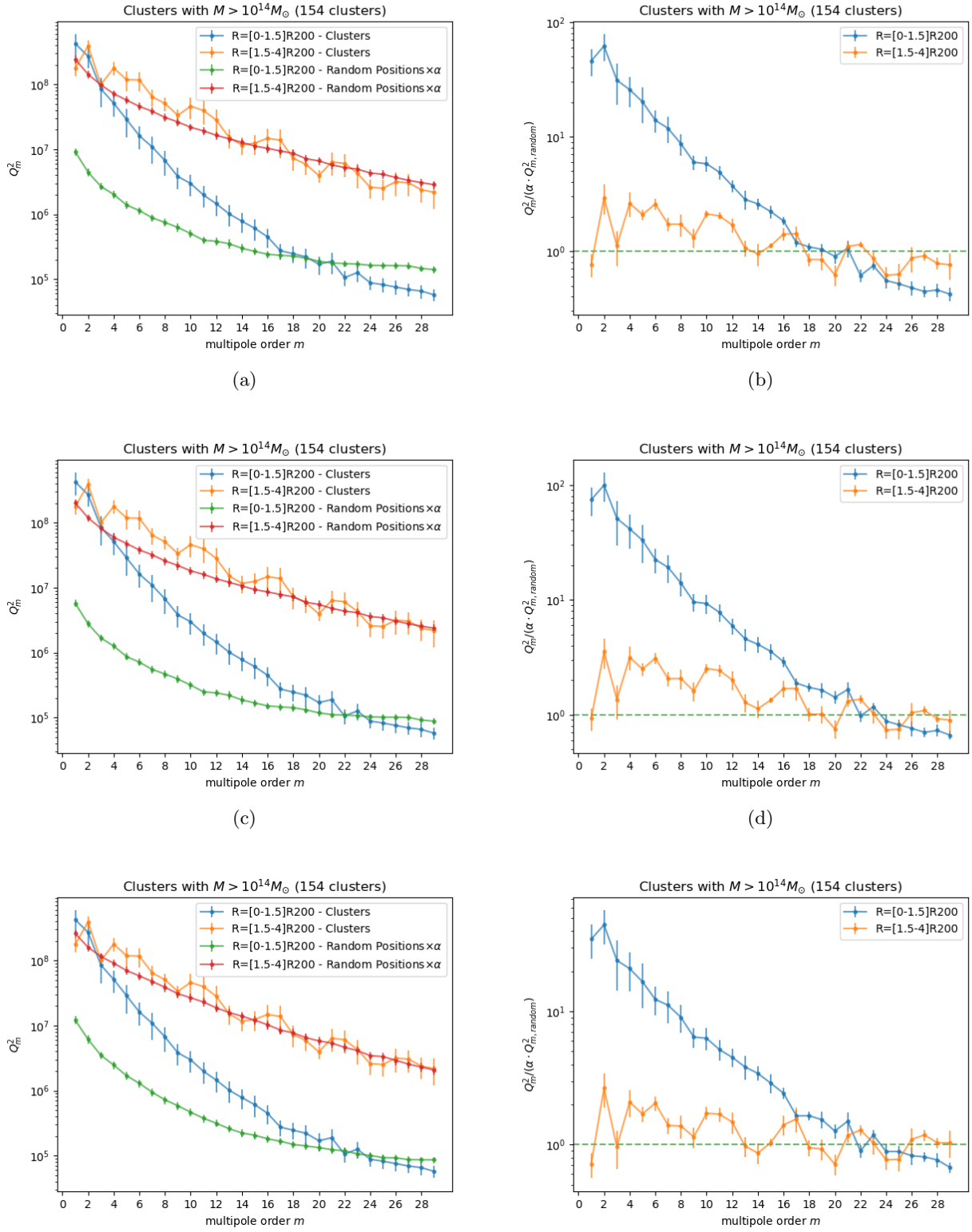

Figure 6.3: Harmonic power spectra (left), and harmonic power excess (right) of gas distribution around clusters with $M_{200} > 10^{14}\ M_\odot$ in TNG300-3, for two apertures: $R = [0 - 1.5]R_{200}$ and $R = [1.5 - 4]R_{200}$. *Top*: setting the threshold for α to $th = 15$. *Middle*: setting the threshold for α to $th = 20$. *Bottom*: masking the clusters with $M_{200} > 10^{13}\ M_\odot$.

To test this hypothesis we decided to mask only the clusters with $M_{200} > 10^{13}\ M_{\odot}$, and to lower the radius of the mask around clusters from 6 to $4R_{200}$. The result of this test is shown in Figs. 6.3(e), 6.3(f): comparing the first one with the one directly above (Fig. 6.3(c)) we notice indeed a slightly steeper curve for the random positions at low orders, but definitely not enough to cure the unexpected behaviour of the normalized power excess in the inner region.

6.2.5 New selection criteria

Trying to understand the source of the unusual steepness of the power inside the inner aperture we realized that the method we were using to separate the two apertures was not fitted to our purposes. In fact, up to that point we were selecting the particles based on their 3D radius, and only later projecting them. This means that we were actually sorting the particles in spherical shells rather than in cylinders before the projection, effectively excluding from the inner annulus all the particles that are placed behind and in front the inner cluster sphere, which is not what we wanted to obtain. This might be the reason for the mismatch with the random profile at high orders.

For this reason we changed the selection process, first identifying in 3D space all the gas particles inside a sphere of radius $4R_{200}$, then projecting them along the three axes, and finally sorting them by their 2D radius in each projection. This approach is the appropriate also from an observational point of view, since what we observe in the sky is the projection along the line of sight of the full cluster, together with its surroundings, and there is no way to separate the inner from the outer components along this direction.

The result of this new method is presented in Figures 6.4(a) and 6.4(b), where we focus on the harmonic power for the inner region, since the outer one is unchanged. From 6.4(a) we see that there is a better agreement between the cluster and the random curve at high orders, and the random power is higher than before at low m, but still not high enough to match the cluster harmonic power spectrum for orders lower than $m \sim 20$; this translates in Fig. 6.4(b) into a flatter power excess at high orders (although still not converging to 1 properly), and a lower and less steep curve for $m < 20$ compared to the previous cases.

6.2.6 Centering on gas distribution

In all the analyses and tests we described so far, we used the center of mass from the group catalogue as reference point for the center of the cluster, which is computed using all particles and cells in the group, of all types (namely dark matter, gas, stars and black holes). We decided to investigate if there was a difference between the center of mass computed with all matter and a different method of centering based only on the gas particles; and, if so, whether this difference affected the multipole analysis.

To compute the center of the gas distribution we decided to apply a variant of the shrinking sphere method described in [23], which can be summarized as follows:

- The gas particles inside $1R_{200}$ from the center given by the simulation are selected.
- The center of mass of these particles is computed, and becomes the starting point for the successive steps.
- At each iteration, a new center of mass is computed from the particles inside a sphere centered on the previous center of mass and a radius 2.5% smaller than the previous iteration.
- The process is stopped when the number of particles inside the sphere gets smaller than a certain threshold which depends on the M_{200} of the cluster.

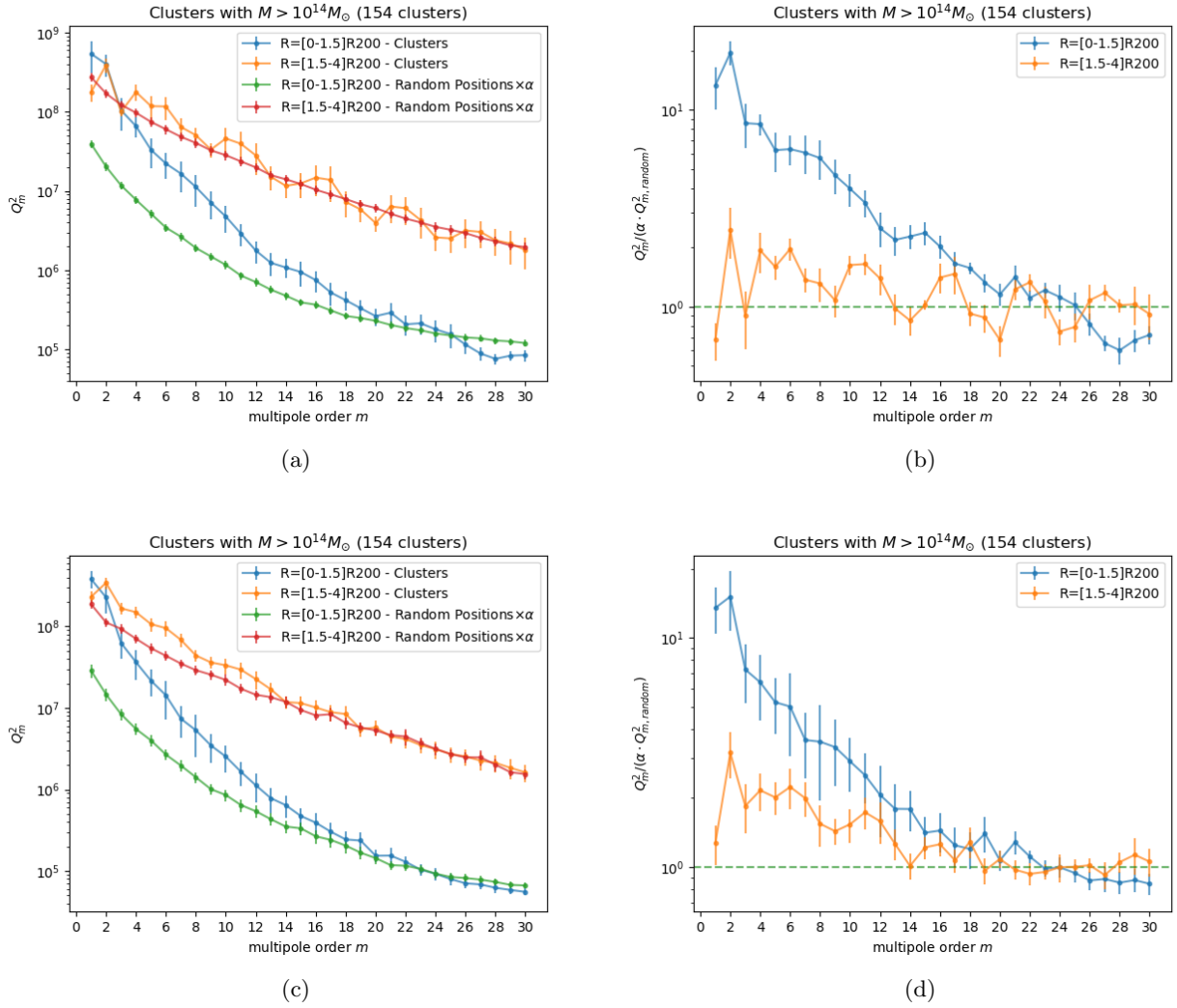

Figure 6.4: Harmonic power spectra (left), and harmonic power excess (right) of gas distribution around clusters with $M_{200} > 10^{14}\ M_\odot$, for two apertures: $R = [0-1.5]R_{200}$ and $R = [1.5-4]R_{200}$. *Top*: using the new selection criteria described in the text *Bottom*: centering the analysis on the gas distribution.

Following this procedure we found that there generally is a displacement of the center of the gas distribution with respect to the center of mass of the cluster. However, the displacement tends to decrease with the mass of the cluster. Fig. 6.5 exemplifies this, where 2D histograms of the gas distribution for some example clusters are shown together with the two centers.

On average, for the clusters with $M_{200} > 10^{14}\ M_\odot$, this displacement is ~ 0.21 Mpc$/h$; while considering the clusters with $M_{200} > 10^{13.5}\ M_\odot$, the mean displacement is reduced to ~ 0.16 Mpc$/h$.

We then recomputed the harmonic decomposition using the updated center positions, and the results are presented in Figures 6.4(c), 6.4(d). Looking at Fig. 6.4(d), we can immediately realize that the centering does not solve the difficulty with the inner region harmonic power excess, although it does help the matching of the cluster and random curves at high orders, making the power excess consistent with 1 for $m > 22$. Focusing on the outer region we see a much clearer signature of consistent power excess up to order 14, which is also what we found during the analysis of the galaxies, even though it doesn't completely flatten to one at higher orders.

All these results seem encouraging at first, but the effects are unfortunately only relevant for the high

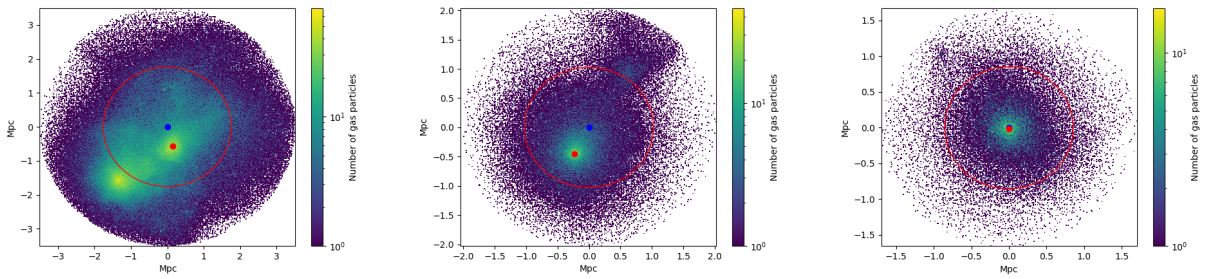

(a) (b) (c)

Figure 6.5: Examples of the differences in center in three clusters: in blue the position given by the simulation and in red the center found focusing on the gas distribution, the red circle has radius R_{200} centered on the blue dot. The clusters have mass: (a) $M_{200} = 12.6 \times 10^{14}\ M_\odot$ (b) $M_{200} = 2.5 \times 10^{14}\ M_\odot$ (c) $M_{200} = 1.4 \times 10^{14}\ M_\odot$.

mass clusters which are low in number. As we found out performing the test described in the next section, when considering a larger set of clusters with lower masses, these effects become completely negligible.

6.2.7 Aperture and mask comparisons

At this point, we decided to investigate and compare more in detail the effects of changing the radius of the inner aperture in combination with the masking of the clusters for the random positions choice. We decided to analyze larger number of clusters, selecting the ones having mass M_{200} larger than $10^{13.5}\ M_\odot$. Then we analyzed the harmonic power distribution in a range of different radii from the center, namely $[0-0.5]R_{200}$, $[0-1]R_{200}$, $[0-1.5]R_{200}$, $[0-2]R_{200}$, and using three different masking thresholds for the random positions: applying no mask, therefore choosing the positions across the whole simulation box; masking the clusters with $M_{200} > 10^{13}\ M_\odot$; and masking all the groups listed in the simulation catalogue. We took an aperture set on the far outskirts of the clusters with $R = [2.5-4]R_{200}$ as a reference to compare these results. We also tried comparing the effect of changing the centers of clusters as in the previous section, but in this case the harmonic powers are basically unaffected by this change.

The results of these analyses can be seen in Fig. 6.6. Looking at the figures on the right one can see that the overall shape of the power excess curves in the regions close to the clusters is more or less the same, exhibiting an excess of power until around order 20, which is roughly independent of the aperture and the masking. Nonetheless, some differences are present: going from the smaller to the larger aperture we see a larger dominance of the quadrupolar term, associated with an elongated shape, and a general decrease of power in the odd orders with respect to the even ones until $m \sim 8$, which may also suggest a slight preference towards an even distribution. However, given the large power excess at all orders smaller than at least ~ 15, it is difficult to draw any meaningful conclusion about the projected shape of the gas distribution.

Comparing the three different masks the most evident feature is the increase of power excess in the inner regions when masking more clusters, and it can also be seen in the left panels of Fig. 6.6, looking at how the random power profiles get lower compared to their respective cluster power as we increase the masking. This is due to the fact that the signature coming from structures that are unmasked gets incorporated into the random harmonic powers, which on one hand makes them more similar to the ones calculated around clusters. On the other hand, there is the risk to hide interesting features from structures such as filaments, whose signal in harmonic space is rather low and spread over various multipoles. In fact this is what happens with the "control" aperture at $[2.5-4]R_{200}$: when no mask

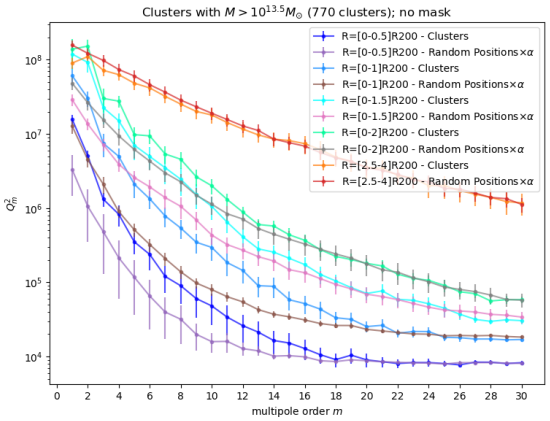

(a)

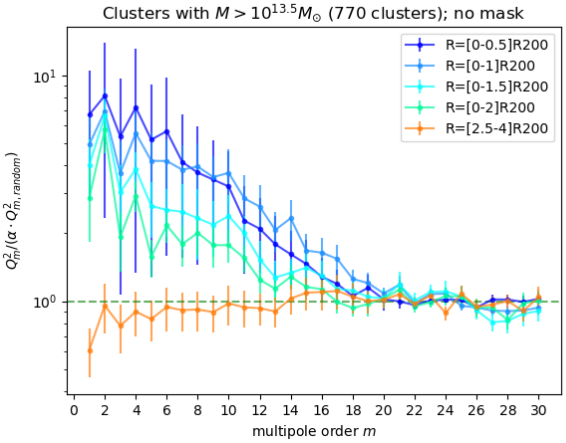

(b)

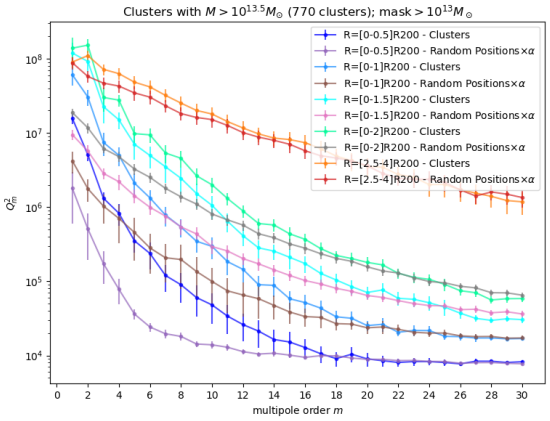

(c)

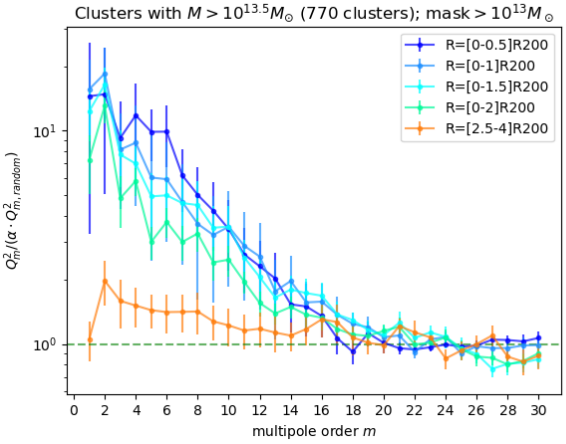

(d)

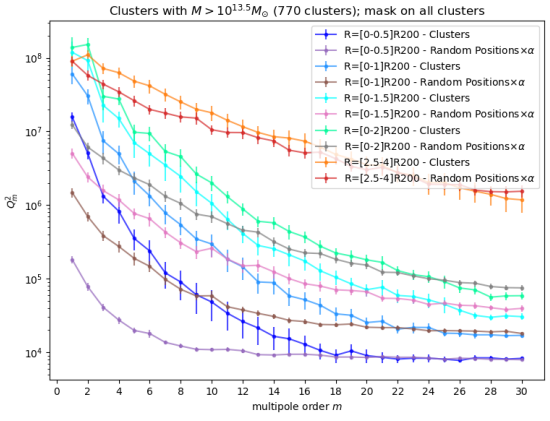

(e)

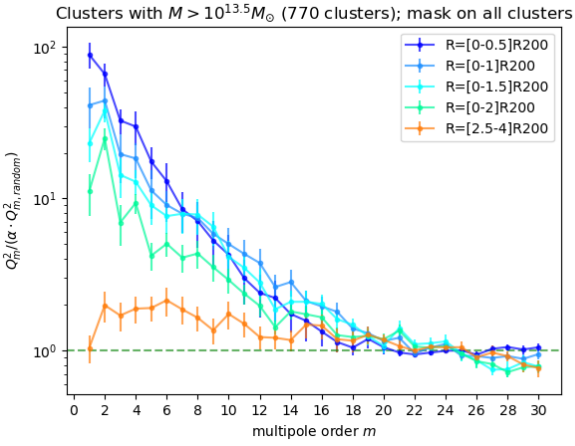

(f)

Figure 6.6: Harmonic power spectra (left), and harmonic power excess (right) of gas distribution around clusters with $M_{200} > 10^{13.5}\ M_\odot$, in a span of apertures (see main text). *Top*: putting no mask on clusters *Middle*: masking clusters with $M_{200} > 10^{13}\ M_\odot$ *Bottom*: masking all the groups in the catalogue.

is implemented (Fig. 6.6(b)), we cannot see any significant difference between the cluster and the random powers, apart from a lack of power in the dipole; whereas if we apply a mask on some (or all) clusters (Figs. 6.6(d) and 6.6(f)) a relevant power excess is found in various orders from $m = 2$ to 10 or 12. For this reason we decided to take 10^{12} $M_\odot$ as minimum mass for the masked clusters.

6.2.8 Reconsidering the continuous approach

Another hypothesis for the source of the unexpected power distribution of the inner region multipoles was that of an unknown problem with the particle-based approach. To test this possibility we considered two different methods to perform the harmonic decomposition, based on a more continuous-oriented approach. The basic idea is to build a 2D map of the gas distribution, and use that to compute the harmonic powers.

The first method consists in creating a 2D polar histogram, formed by 100 evenly spaced angular bins and a variable number of radial bins, 0.1 Mpc in size. These bins are then filled with the gas particles weighted by their mass. Then, the harmonic decomposition is computed using these bins as "pixels" of the 2D map. Fig. 6.7(a) and 6.7(b) show the results of this method: the general shape of the power excess using this approach is not different from the ones we analyzed before with the particle approach. In fact, looking at Fig. 6.8, where a comparison of the different methods is shown, we see that apart from the overall amplitude, this first method gives the same results as the particle one.

The second method also starts from computing a 2D histogram as the first one, but then interpolates it using the Python `SciPy`'s function `interp2d` with a cubic spline. The resulting function is then sampled on a 50×50 polar grid to compute the harmonic decomposition. The results obtained with this method are presented in Figures 6.7(c), 6.7(d). The overall shape of the harmonic power excesses in the two regions (right panel) seems consistent with the previous findings, thus not solving the issues with the inner region. Moreover, when looking at Fig. 6.7(c), and we compare it with Fig. 6.7(a), we see a strange and unexplained rise of power at high orders in basically all the four curves, which is significantly different from all the results we saw previously.

Both methods will be applied and further investigated in the next Section.

6.3 Comparison with simulated distributions

In the effort to understand the reason for the unexpected behaviour of the harmonic power excess in the inner region of clusters, we proceeded with a series of tests in which some known 2D distribution of particles were injected into our code, to see if it responded as we would expect.

The first step was to draw randomly a set number of particles from four different distributions: a 2D Gaussian, a pure quadrupolar ($m = 2$) distribution, a combination of the previous two, and a 2D elliptical distribution. The number of particles was chosen to match the average number of gas particles inside $4R_{200}$ around clusters with mass larger than $10^{13.5}$ $M_\odot$, which is roughly equal to 50000 particles. A rotation of a random angle was also applied, before computing the multipole powers with the three methods we discussed previously in section 6.2.8. This procedure was repeated 50 times and the results averaged.

The results of this analysis are presented in Fig. 6.9. Each row shows the results for a different distribution. In the left column there is an example map from the ones we used for the analysis. The column in the middle shows the harmonic powers calculated in the inner region ($R = [0 - 1.5]$) using the three different methods, while the one on the right contains the ones computed in the outer region of the simulated maps ($R = [1.5 - 4]$).

Taking a general look at the middle and right column, we see that in all pictures the results using the

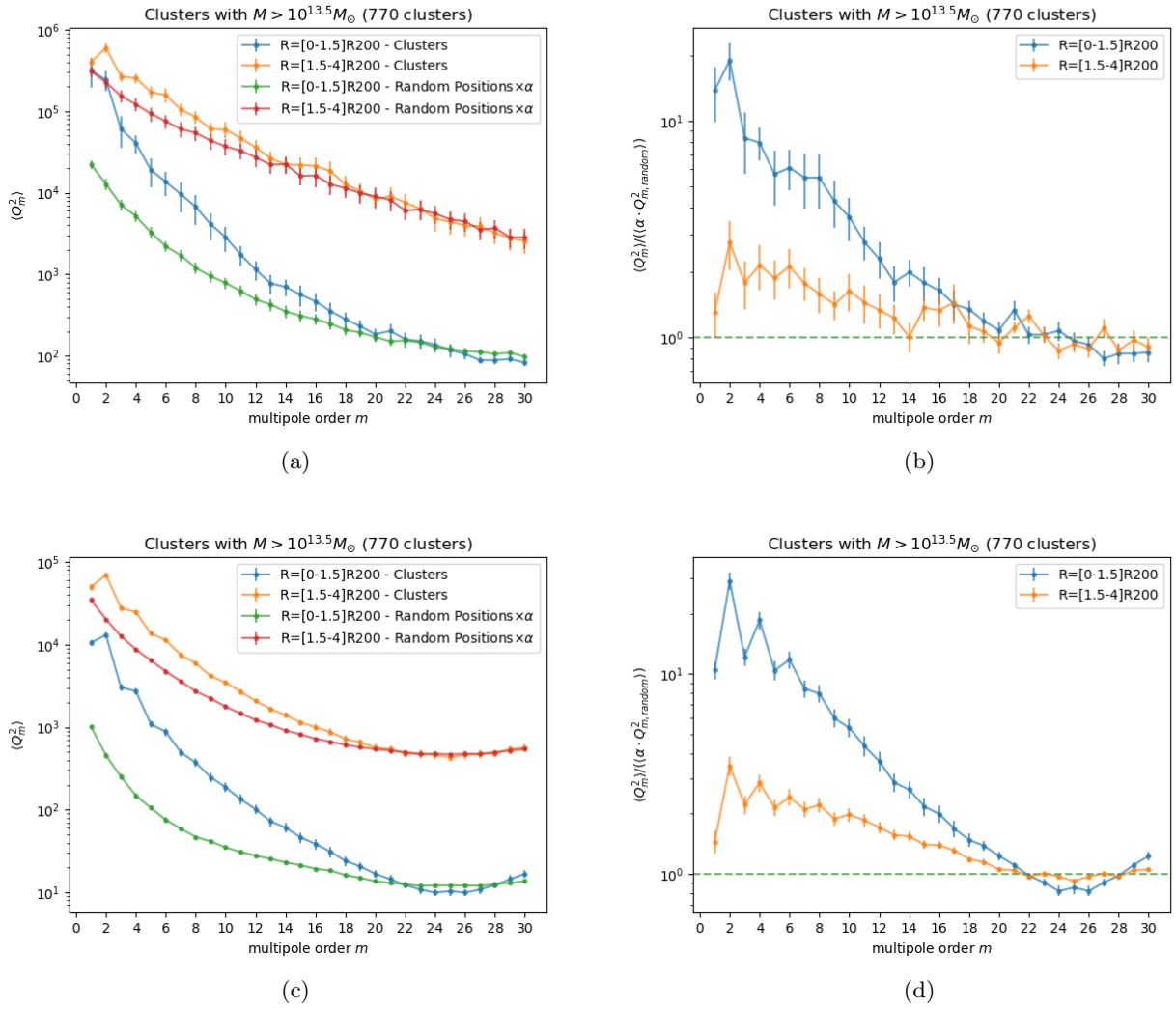

Figure 6.7: Harmonic power spectra (left), and harmonic power excess (right) of gas distribution around clusters with $M_{200} > 10^{14}\ M_\odot$, using the two continuous methods described in the text. *Top*: first method *Bottom*: second method.

particle and the first continuous approach closely match each other, with some very small deviations, confirming their equivalence in the harmonic powers analysis, as we argued in the previous section. On the contrary, the second continuous approach gives a large and unexpected boost of power to small orders in all the cases where the distribution presents a dense central core, which is very puzzling (while the difference in the baseline is not a symptom of bad behaviour).

Examining the different distributions more closely, we see that in the Gaussian case the first two approaches give no significant feature for $m \geq 1$, as we expect for an isotropic map, while the third method produces an unexplained signal at orders 1 and 2 in the inner region, which extends to $m = 3$ in the outer region. When considering a pure quadrupolar distribution, all three methods give results that are consistent with our expectations, with a spike at $m = 2$ and a flat profile elsewhere. This fact is a reassurance that the first two methods work well, while it adds to the puzzlement for the third approach, whose behaviour we have no explanation for.

Combining the previous two distribution in the third row of Fig. 6.9, we see that the particle and the first continuous approaches continue to behave well, showing the same features as in Figs. 6.9(e)

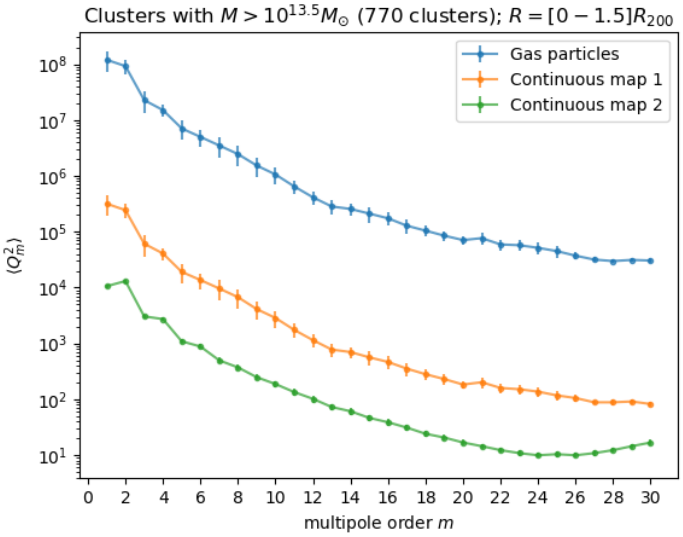

Figure 6.8: Comparison of the harmonic power spectra of gas in the inner aperture around clusters, computed using the different approaches described in the text: particle-based method (blue), first continuous method (orange), second continuous method (green).

and 6.9(f), as the $m = 2$ distribution is the only one that breaks the circular symmetry. On the other hand, the second continuous approach again shows large unexpected power at low orders. Moreover, this power extends to larger multipoles rather than being the simple sum of the two harmonic spectra above. All these considerations made us distrust this last approach as faithful for the harmonic analysis, so from now on we will not consider it anymore.

Last, we tested an elliptical distribution, which is considered to be in general a better approximation of the projected shape of clusters, from both observations and simulations (see for example [35]). In this case an interesting feature is observed (ignoring the third approach as we argued before): in the internal region we can again see a large power in the quadrupole term, as we would expect from an elongated structure. In addition, we see a smaller but significant power in the $m = 4$ order, coming from the fact that we are not probing a pure $m = 2$ distribution, but there are particles also in the region perpendicular to the major axis of the ellipsis. The same pattern is visible in the outer region multipoles, but extending to all even orders up to $m = 10$, with power decreasing as a power law with increasing order. This very clear and recognizable pattern, coming from probing the outer part of an elliptical distribution, will be useful to interpret one of the results in the next Section.

The result for the inner region of the elliptical distribution is perfectly compatible with what we found in the analysis of galaxy distributions (Fig. 5.5), confirming the conclusions that we drew there, but it is clearly very different from what we obtained analyzing the gas distribution. In light of this, given also the limited time of my project, we decided to abandon this line of research, and concentrate on the outskirts of galaxy clusters, where the most interesting results concerning the structure of the cosmic web can be found.

6.4 Results for the different phases in the cluster's outskirts

The harmonic power spectrum of the various gas phases in the outskirts of the clusters can give important information on their distribution around the collapsed structures. Therefore, we investigated the azimuthal behaviour of the three main phases that populate the surrounding of clusters: the Hot Medium (HM), the Warm-Hot Intergalactic Medium (WHIM) and the diffuse part of the Intergalactic

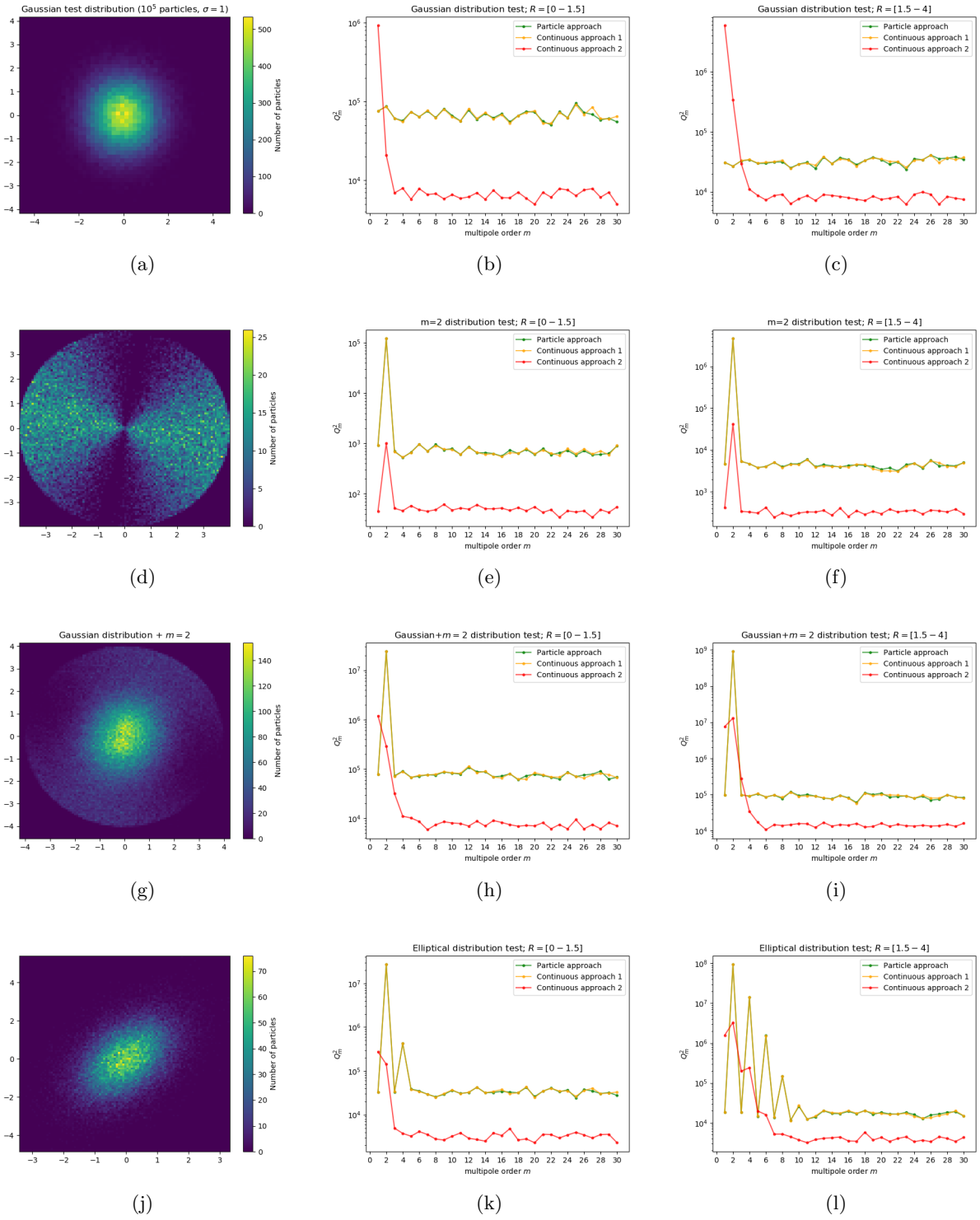

Figure 6.9: Harmonic power spectra of simulated distributions, computed with the three different methods described in the text. On the left, an example of the simulated distribution; in the middle, the power spectra in the inner aperture $R = [0 - 1.5]$; on the right, the power spectra in the outer aperture $R = [1.5 - 4]$. From top to bottom: 2D Gaussian, quadrupolar ($m = 2$), Gaussian plus quadrupolar, elliptical distribution.

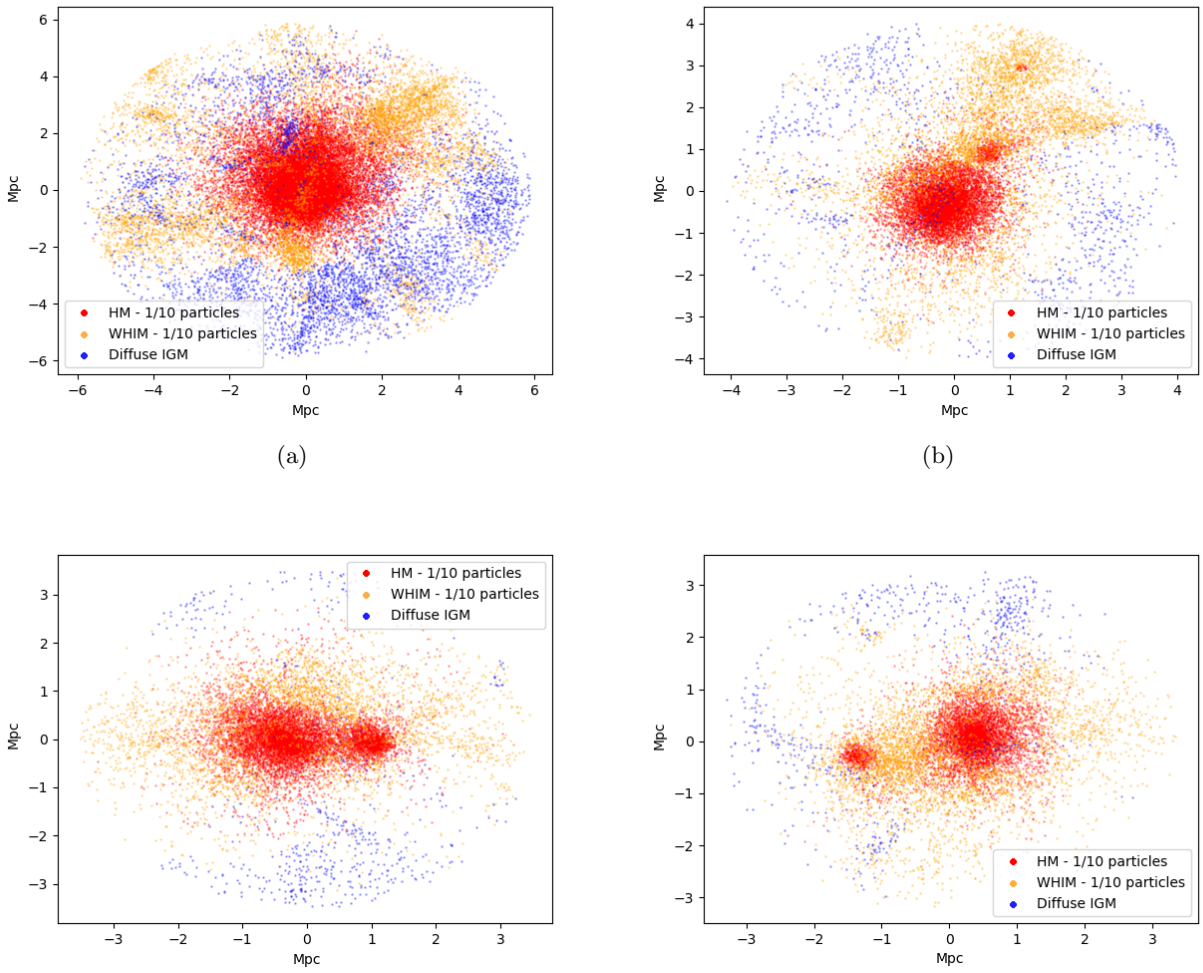

Figure 6.10: Four examples of the distribution of gas around galaxy cluster in TNG300-3, coloured by phase: Hot Medium (red), WHIM (orange), diffuse IGM (blue).

Medium (diffuse IGM), as defined in Section 3.4. As reported in [38], we expect the Hot Medium to be concentrated mainly in the knots of the Cosmic Web, that is in the galaxy clusters. The WHIM should represent a large fraction of the gas in filaments and clusters, while the diffuse IGM is expected to be found predominantly in sheets and voids. In Fig. 6.10 four examples of the distribution of these phases around clusters are shown.

The results of the harmonic analysis of the three phases are shown in Fig. 6.11; on the left the clusters' and random positions' multipole powers, and on the right the corresponding harmonic power excess. For this analysis we decided to mask the clusters with $M_{200} > 10^{12}\ M_{\odot}$, in order to exclude all the clusters that might be visible in an observational study.

We start from the analysis of the HM, in Figures 6.11(a) and 6.11(b). Looking at the second panel we immediately notice the resemblance to Fig. 6.9(l), with large power at all even orders until $m = 10$. This feature clearly indicates that we are probing the outer part of an ellipsis, thus confirming that the HM phase is indeed concentrated in the inner region of clusters and, more importantly, that it is distributed on average following an elliptical shape.

Turning to the central row of Fig. 6.11, we see the results of the analysis of the WHIM distribution:

in the right panel (Fig. 6.11(d)) we see that the harmonic power excess has a shape similar to the one we found for the galaxy distribution (Fig. 5.5), with a higher peak at $m = 2$ and then a decreasing power up to $m = 12$, proving that the WHIM phase traces the filamentary structures around clusters in a similar way to galaxies.

In Figures 6.11(e) and 6.11(f) we finally see the result obtained with the diffuse IGM phase: surprisingly, instead of having an excess of power at low orders, we have a lack of it in the clusters compared to the background gas distribution, with the two matching only around $m = 16$. This result certainly needs to be further investigated in the future, as it is not clear what could be the cause of this behaviour. One hypothesis is that this is a hint that the diffuse IGM is distributed outside the collapsed structures, mainly at the edges of the region considered (as suggested by the examples in Fig. 6.10).

6.5 Conclusions

In this Chapter, we analyzed the distribution of three gas phases in the outskirts of galaxy clusters (due to the reasons discussed before) from the simulation TNG300-3, using the harmonic power excess to characterize statistically the patterns in harmonic space of the various components we probed.

The phases we considered were: hot medium, warm-hot intergalactic medium (WHIM) and diffuse IGM. For these phases we found that:

- the hot gas (Hot Medium) is concentrated in the inner regions of clusters, with only its outer parts extending beyond R_{200}, and its projected shape is on average elliptical, as signaled by the peculiar shape of the harmonic power spectrum;
- the Warm-hot Intergalactic Medium is the phase that better traces the filamentary structures highlighted in the galaxy study, given that its harmonic power spectrum presents a similar shape with respect to the galaxy one;
- the Diffuse Intergalactic Medium presents an harmonic power at low orders that seem to be lower than the background one, this fact is difficult to interpret and needs to be further analyzed, but it could be an hint to the fact that this gas phase seems to sit at the edge of the region probed and outside the filaments.

Further studies will need to explain the results with the gas distribution in the inner parts of clusters, which we were not able to address, together with the lack of power at low orders of the diffuse IGM phase compared to the background.

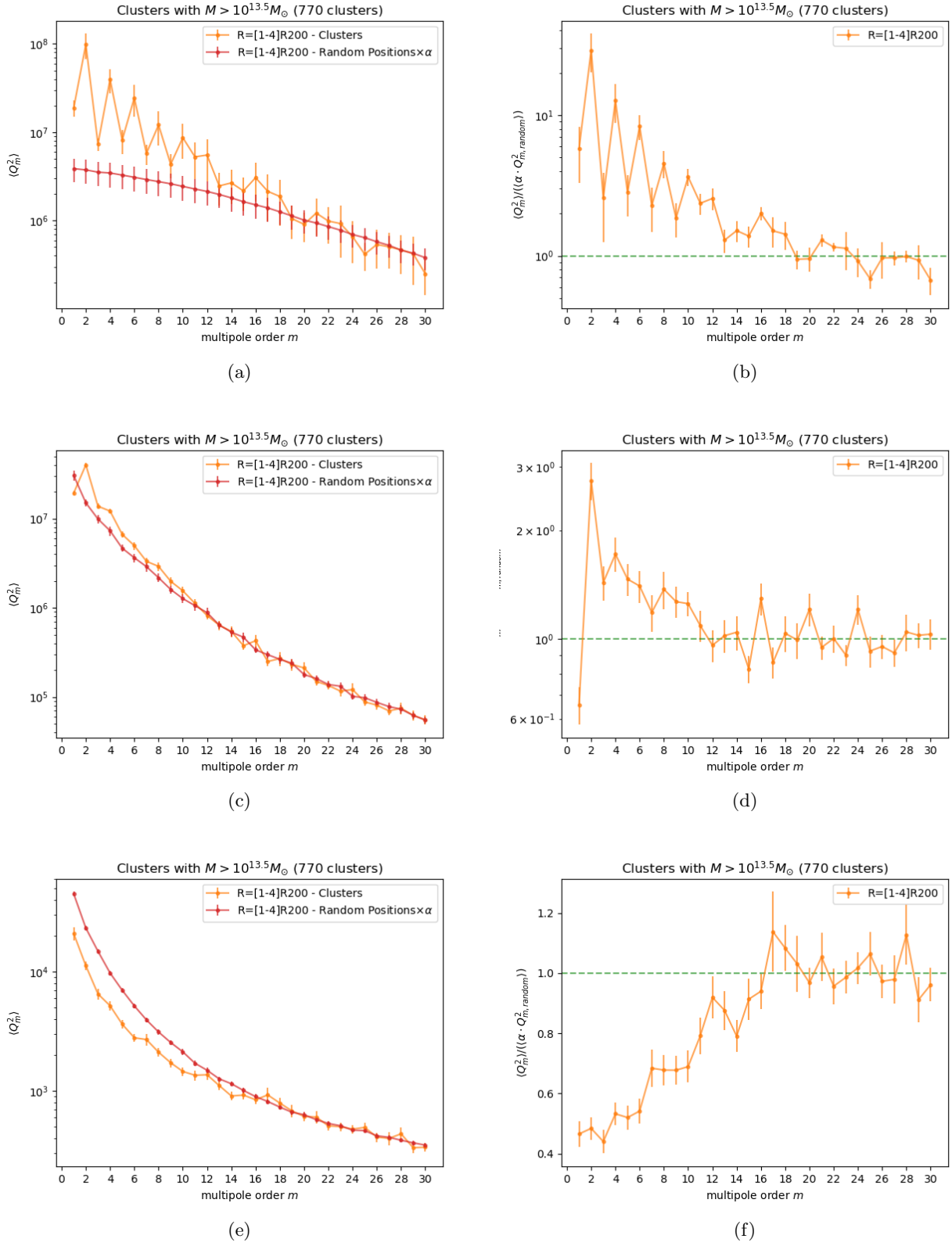

Figure 6.11: Harmonic power spectra (left), and harmonic power excess (right) of the distribution of different gas phases around clusters with $M_{200} > 10^{13.5}\ M_\odot$, for the aperture $R = [1-4]R_{200}$. From top to bottom we have: Hot Medium, WHIM, diffuse IGM.

Chapter 7

Beta analysis on gas phases and DM

In the last part of the project we focused on the second question underpinning our work: how does the level of anisotropies (with respect to a spherical distribution) in clusters' matter distribution correlate to the cluster properties?

To answer this question we make use of the parameters $\beta_{2,3,4}$ defined in Section 4.3, which are meant to represent the main contributions to the anisotropic behaviour of matter distributions. This hypothesis is supported by previous studies on multipole moments [21, 23, 66], and also by the results of this work presented in Chap. 5 and 6, where we notice that, in general, the multipole orders $m = 2, 3$ and 4 are the ones with the largest powers in the harmonic decomposition. Furthermore, we have already observed that different multipole orders highlight different symmetries. Going back to Fig. 4.2, we see that the orders $m = 2, 4$ probe preferentially structures with elongated shapes, while $m = 3$ is more sensitive to structures in which the matter is not aligned along a single direction through the cluster.

7.1 Procedure

For this analysis, we decided to take the highest resolution simulation, TNG300-1, in order to be consistent with the choice of [22]. As suggested in the conclusions of [22], we decided to use a smaller sample of massive galaxy clusters with respect to that work, considering only the ones with masses $M_{200} > 5 \times 10^{13}\, M_{\odot}/h$, aiming to highlight the correlations between cluster properties and the outskirts' anisotropies. Following [22], we also decided to exclude the groups that are located closer than $3 \times R_{200}$ from the edge of the simulation box. We therefore end up with a final catalogue of 415 clusters. Then, as we did for the analysis of the harmonic power excess, we project the matter distribution of the clusters along the three axes of the simulation box, obtaining 3×415 group projections.

We then computed the three parameters, $\beta_{2,3,4}$, were computed in different apertures, and for different matter components. The apertures that we probed were: $[0-1]R_{200}$ and $[1-4]R_{200}$ which, as before, are meant to differentiate between the inner regions and the outskirts of clusters. We also decided to split the outer region in two, and compute the βs on the apertures $[1-2]R_{200}$ and $[2-4]R_{200}$, this choice was made in order to investigate the radial evolution of the asymmetries, from the inner part to the far outskirts. Furthermore, the aperture $[1-2]R_{200}$ is also used to show the correlation of the βs with the connectivity, that is computed at a radius of $1.5 \times R_{200}$, as explained in Section 3.3. As for the matter components analyzed, we decided to focus on three components: dark matter, hot gas (HM), and WHIM. We chose these because we were interested in seeing the difference behaviours of the main gas components' distributions in clusters with respect to a "reference" dark matter distribution.

As we said before, our goal is then to study the relationship between the asymmetric distribution of

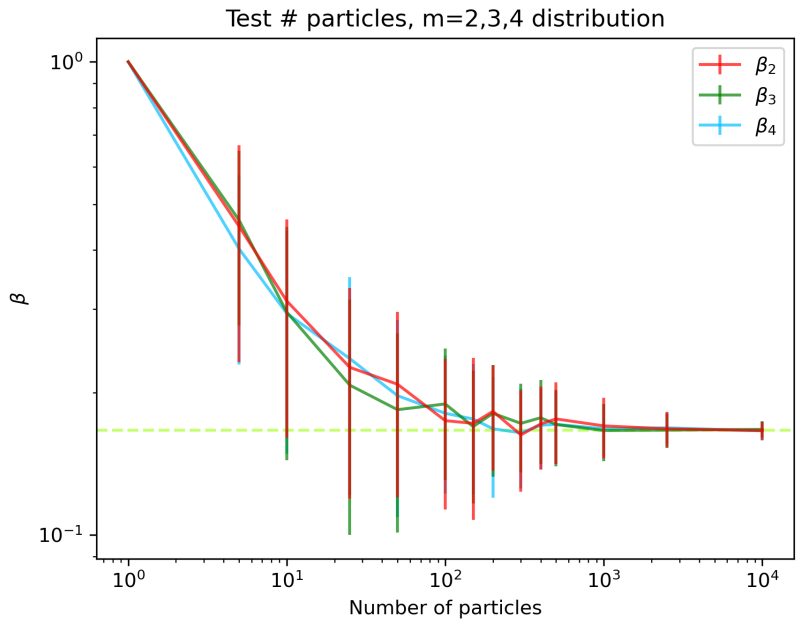

Figure 7.1: Test of the influence of the number of particles in the aperture on the value of $\beta_{2,3,4}$. For each number of particles considered, 100 maps are sampled from the same distribution, the βs are computed on these maps and then averaged. Here the average and standard deviation of $\beta_{2,3,4}$ are shown as a function of the number of particles.

matter and the cluster properties listed in section 3.3.

Before starting with the main analysis, though, we decided to test the limits of our new estimators, performing a series of tests on simple known distributions. Since we chose to estimate the gas distribution by using the center of gas cells such as "gas particles", we have to carefully identify limitations of beta computation on point distribution.

7.2 Tests on the beta parameters

7.2.1 Influence of the number of particles

This first synthetic analysis aims to constrain the number of minimum particles that are needed to accurately probe asymmetries with the β parameters.

Therefore, we simulated a combination of the three distributions with annular symmetries peaked at $m = 2, 3, 4$ with equal weights. In this way, when doing the harmonic decomposition of the resulting distribution, the three β parameters return the same value. Then we sampled this distribution with an increasing number of particles, from 1 to 10^4, and we computed the β parameters on the resulting 2D point distribution. The mean $\beta_{2,3,4}$, computed on the synthetic maps, together with their standard deviations are shown in Fig. 7.1.

As we can see from Fig. 7.1, the value of the β parameters converges to the theoretical expected value when the number of particles used to discribe the matter distribution is closed to one hundred. Below this number, the matter distribution is sub-sampled, and thus, beta estimator is contaminated by shot noise in matter distribution, up to the extreme case of becoming equal to one when there is only one particle. Following this analysis, we decide to consider that few hundred particles inside a given aperture are needed to accurately evaluate beta without noise contamination.

We therefore conclude that our new estimators are quite robust with respect to the number of particles. In fact, when looking at the cases we are interested to study (i.e. matter in and around galaxy clusters in TNG300-1), we see that for our choices of apertures and components the large majority of the distributions have many more particles than just a few hundreds; only when we consider the hot medium in the outskirts of clusters there are some cases where we cannot trust the values of $\beta_{2,3,4}$.

7.2.2 Influence of clumpy matter distributions

The second question we have investigated is: what is the impact on the β parameters when the matter is not distributed smoothly at all azimuthal angles, but it is rather concentrated in small clumps, and absent elsewhere?

We might expect this behaviour in particular for the hot medium outside galaxy clusters. Indeed, since the hot gas is the one that is heated to very high temperatures in shocks, it is expected to be very subdominant in the outskirts of clusters (as we found in Chap. 6), and probably only concentrated in subgroups massive enough to heat it.

To test the response of the β parameters to this situation, we created a toy model of the cluster outskirts. We created "fake" maps placing small, normally-distributed clumps of particles in the region $[1-4]$ in arbitrary units, with the mean of the 2D gaussian selected randomly in the region, and $\sigma = 5 \times 10^{-3}$, each gaussian clumps contained 1000 particles. In order to simulate also the effect of a central cluster, we tested the maps with and without a larger gaussian placed in the center of the coordinate system, with $\sigma = 0.25$, containing 10^4 particles, so that the tails of the gaussian distribution simulate the outer parts of a cluster, extending beyond the circle of radius 1. Some example maps are shown in Fig. 7.2, together with their multipole decomposition in the aperture $[1-4]$.

From the examples of Fig. 7.2 we can already see that a clumpy distribution of matter has a very important impact on the multipole decomposition, leading to very high powers at many orders, up to very large ones. We also notice that the shape of the power spectrum varies drastically with respect to the relative position of the clumps. These observations already seem to imply that our approach based on the multipole orders $m = 2, 3, 4$ is not adequate to describe accurately this specific matter configuration. The inclusion of the central "cluster" has the effect of lowering the relative power with respect to the order 0 of all other orders $m > 0$.

In order to understand better the dependence of the β parameters on the number of substructures, a more thorough analysis was performed, varying the number of gaussian clumps in the maps from 1 to 6 and taking the average of $\beta_{2,3,4}$ over 100 maps for each number of clumps. We also decided to complicate slightly our toy model in order to better approximate the expected real gas distribution around clusters. First we considered a central cluster with an elongated, elliptical shape[1]. Then we added a further complication, varying the size of the external clumps, taking gaussians with random sigmas ranging between $[0.005-0.05]$, selected randomly using a triangular probability density function peaked at 0.005 and linearly decreasing until 0.05. These tests are shown in Fig. 7.3.

Here we see that a clumpy distribution without central "cluster" gives values of βs that are very high on average, although decreasing with the number of substructures. We also see that varying the size of the clumps (Fig. 7.3(f)) leads to values of $\beta_{2,3,4}$ that are closer to each other, especially for a large number of clumps, while keeping the size fixed makes the values of β_2 and β_3 decrease faster than β_4 when increasing the number of substructures. When considering also the central cluster we see that the values of βs are significantly reduced, in particular with few clumps, but they still remain quite high at ~ 0.4. Introducing an elliptical shape for the central cluster, we see that β_2 becomes larger than $\beta_{3,4}$ for few substructures, as we would expect. Varying the size of the clumps with an elliptical

[1] To simulate it we used a central gaussian distribution with $\sigma_x = 0.2$ and $\sigma_y = 0.45$

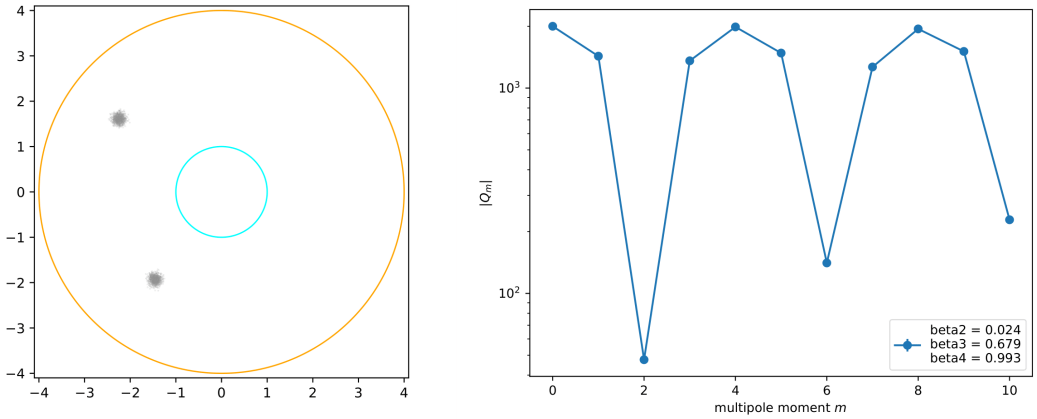

(a) (b)

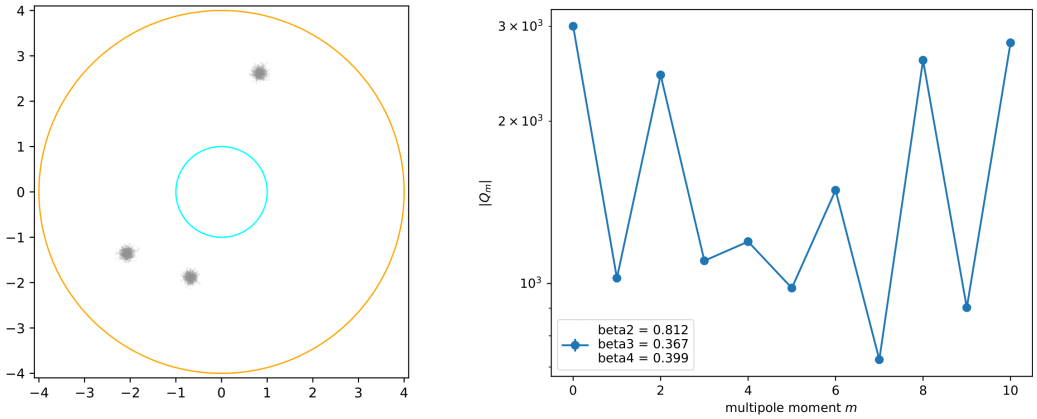

(c) (d)

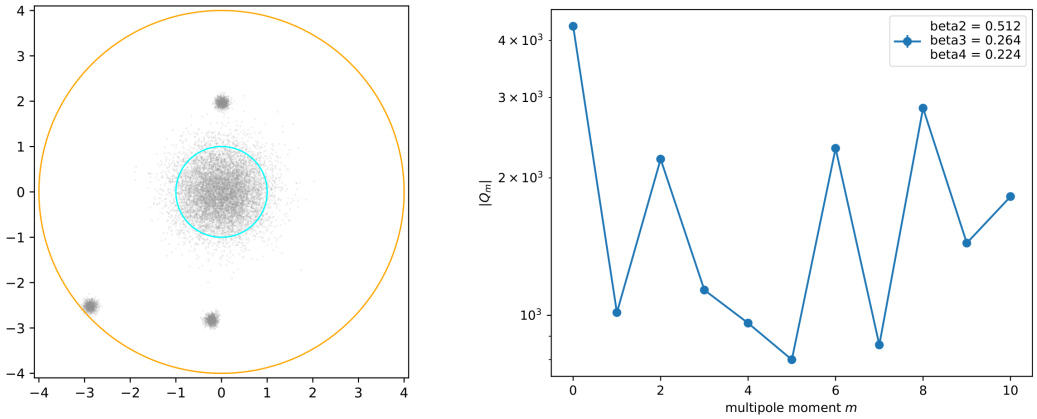

(e) (f)

Figure 7.2: Test of the impact of a clumpy matter distribution on the harmonic decomposition. Three examples of synthetic distributions (*left panels*) with randomly placed Gaussian clumps, and the corresponding multipole decomposition (*right panels*), computed in the region between $R = 1$ (blue circle) and $R = 4$ (orange circle): (*a*-*b*) two clumps, (*c*-*d*) three clumps, (*e*-*f*) three clumps and central "cluster".

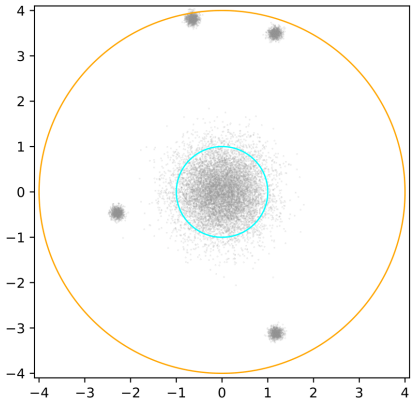

(a)

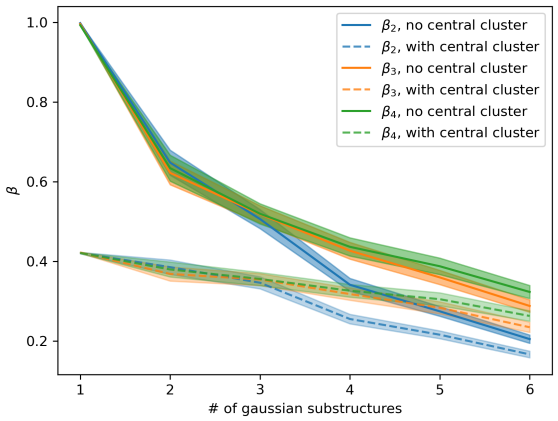

(b)

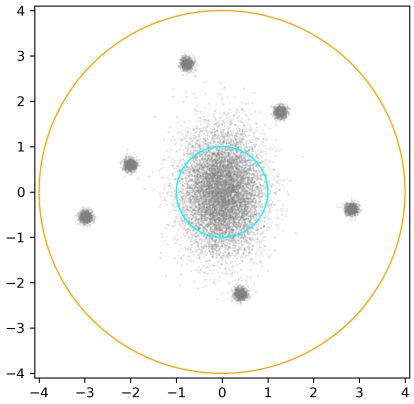

(c)

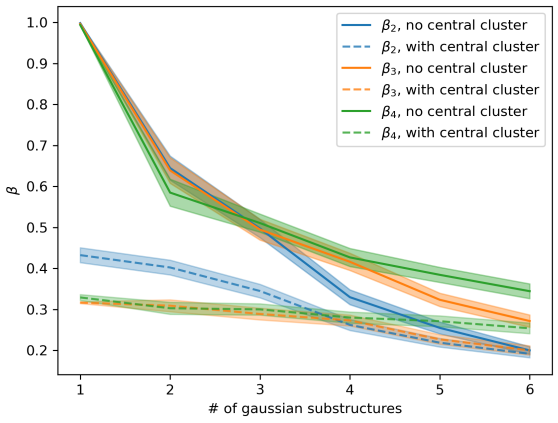

(d)

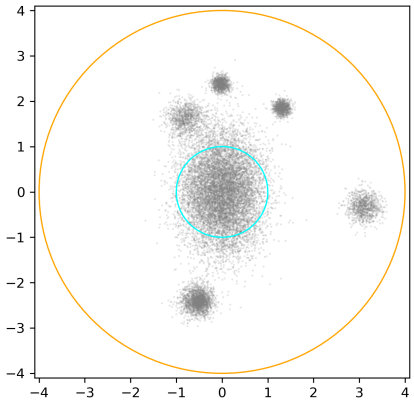

(e)

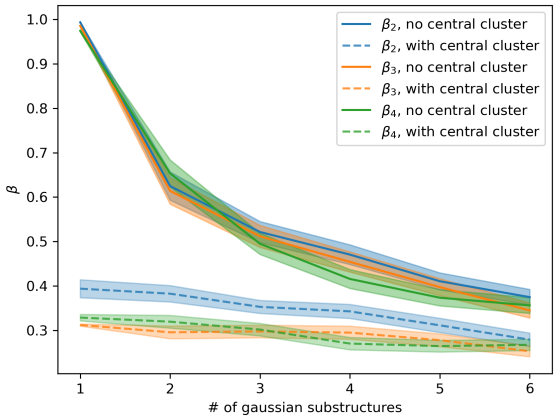

(f)

Figure 7.3: Test of the effect of the number of substructures on the β parameters. On the right panels (*b-d-f*) the average value of $\beta_{2,3,4}$ are shown as a function of the number of clumps, computed in the region between $R = 1$ (blue circle) and $R = 4$ (orange circle) with or without considering the central "cluster" (dashed and solid lines, respectively, the colored areas represent the standard deviation). From top to bottom, three situation are show: (1) considering a spherical central cluster, (2) an elliptical central cluster, (3) elliptical central cluster and varying size of the clumps.

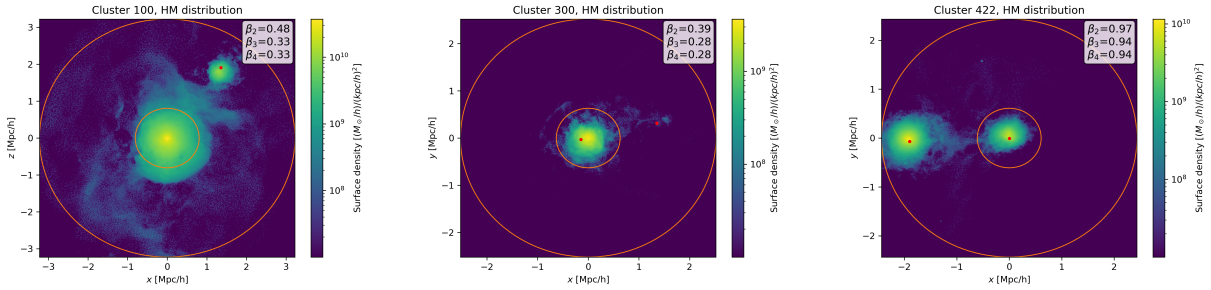

(a) (b) (c)

Figure 7.4: Three examples of hot medium distribution in clusters from TNG300-1. The inner and outer circles have radii of 1 and $4 \times R_{200}$, respectively. The red dots are the centers of the subgroups associated with the possible presence of hot gas, as described in the text. The values of $\beta_{2,3,4}$ for the HM distribution in the region $[1-4]R_{200}$ are reported in the box.

central cluster has the effect of keeping the hierarchy between β_2 and $\beta_{3,4}$ consistent, independently of the number of substructures.

Anyway, we see from Fig. 7.3 that, on average, a clumpy distribution produces values of $\beta_{2,3,4}$ that are always relatively high. This is an important limitation for the use of the β parameters, especially if one tries to interpret their value as the degree of similarity to the perfect multipolar distribution of the same order (as seen in Fig. 4.2). We have shown that this interpretation holds, and leads to important results, in the cases where the matter is distributed more smoothly, but in a case like the one presented here, with most of the matter concentrated in small substructures, it cannot be trusted to give the correct picture of the underlying matter distribution.

Comparison with the simulation data

As we said in the beginning of the last section, we can expect the hot gas far from the cluster center to be concentrated in massive subgroups, and to be almost absent outside of them. We also saw that for this particular configuration, our method provides results that are not easily interpretable and can lead to wrong conclusions. We therefore want to see if this expectation corresponds to the real distribution of the hot medium in the simulation.

To assess this, we want to compare the results coming from the simulation with the ones we obtained using our toy model, in particular the one in Fig. 7.3(f) (which we expect to be the most realistic version of the toy model we investigated).

To do so, we have to relate the values of $\beta_{2,3,4}$ computed of the hot medium distribution in the aperture $[1-4]R_{200}$, with the number of substructures hosting the hot gas. Finding this number is not so straightforward, so we decided to use a simpler proxy: we considered the subgroups in the Subhalo catalogue provided by the simulation, selecting the ones that are massive enough to potentially contain some hot gas, i.e. the ones with total mass larger than $5 \times 10^{12}\, M_\odot/h$. This is quite a crude approximation, but it seems to capture the correct behaviour at first order, as seen in some examples in Fig. 7.4.

Having obtained a catalogue of massive subgroups, we projected their positions along the three axes of the simulation box and associated the number of subgroups that lie in the apertures $[1-4]R_{200}$ to the βs computed in the same aperture for the hot medium.

The result is presented in Fig. 7.5. We see that this result is actually not too distant from what predicted by our simple toy model in Fig. 7.3(f), especially regarding the trends. This seems to

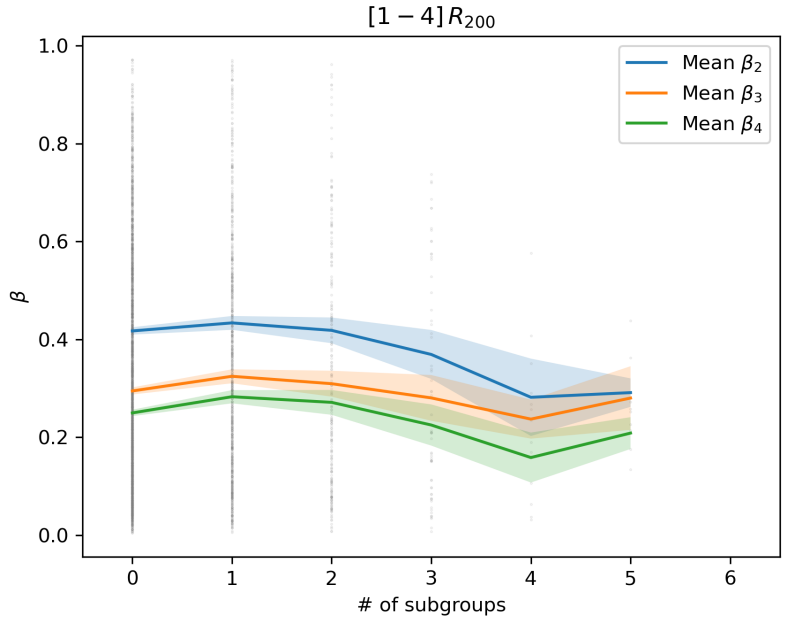

Figure 7.5: Average values of $\beta_{2,3,4}$ computed in the outer regions $[1-4]R_{200}$ of galaxy clusters in TNG300-1, as a function of the number of massive subgroups, as explained in the text.

indicate that our expectations on the hot medium distribution were correct, and that indeed the small clumps of gas dominate the distribution, leading to values of the β parameters that cannot be interpreted with our standard interpretation.

For this reason, we decided to exclude the hot medium outside of clusters from the rest of the analysis, keeping the results of this phase only in the aperture $[0-1]R_{200}$.

7.3 Results

We now present the results of our analysis on the TNG300-1 simulation. As we said before, we want to study the relations between the level of asymmetry in the distribution of the various components with other properties of galaxy clusters. We started by exploring the radial evolution of the β parameters. Then we studied their correlation with the other probes of matter asymmetry, namely the ellipticity and the connectivity, and finally we related them to the cluster mass and its relaxedness.

To obtain a quantitative estimate of the correlation of our parameters with the different properties, we compute the Spearman rank correlation coefficient

$$\rho_{\rm sp}\left(p_i, p_j\right) = \mathrm{Cov}\left(p_i, p_j\right) / \left(\sigma_i \sigma_j\right) \tag{7.1}$$

where p_i and p_j are the two parameters we want to correlate, σ_i is the standard deviation for the parameter p_i, and $\mathrm{Cov}\left(p_i, p_j\right)$ is the covariance between p_i and p_j. We also report the p-values of the coefficients, and we consider a correlation to be statistically significant if its p-value is below 0.05. All the values of $\rho_{\rm sp}$ and the corresponding p-values are reported in Table 7.1, at the end of the Section.

For all figures, we display the mean quantity together with their associated error bars derived from bootstrap resampling.

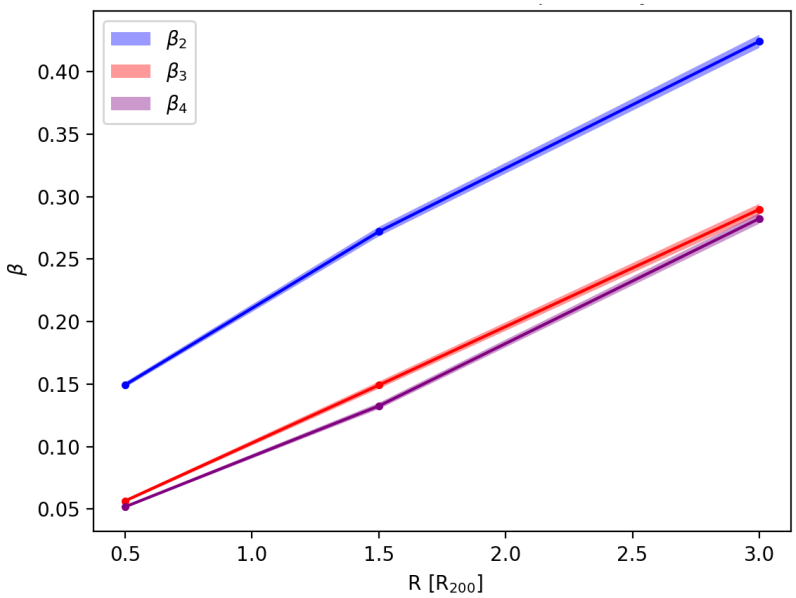

Figure 7.6: Radial evolution of $\beta_{2,3,4}$ computed on dark matter distribution in three apertures: $[0-1]$, $[1-2]$ and $[2-4]R_{200}$.

7.3.1 Radial evolution

The first relationship we explored was the one between the β parameters and the radial distance from the center of the cluster. For this reason we computed $\beta_{2,3,4}$ for dark matter in three apertures: $[0-1]$, $[1-2]$ and $[2-4]R_{200}$, where the last one is larger in order to ensure a good statistics.

The results are shown in Fig. 7.6. Here we clearly see that all three βs grow with the radius, a sign that the matter distribution gets more asymmetrical the further we go from the cluster center. This confirms our results of the previous Chapters, that showed how the matter distribution becomes more complex and less isotropic in the cluster outskirts. We also observe that in the inner regions of clusters the distribution is almost quadrupolar, with β_2 dominating over the other orders, and thus carrying the most part of the information on the asymmetry. On the other hand, when looking at larger radii in the outskirts of clusters, we see that, even if the order 2 is still the most important, also β_3 and β_4 become relevant to describe the level of asymmetry of the matter distribution.

Based on these observations, we decided to use as probes of the asymmetry level with respect to the isotropic distribution only the β_2 parameter inside of clusters (inside R_{200}), while using the sum of the three βs in the cluster outskirts, $\beta_{2+3+4} = \beta_2 + \beta_3 + \beta_4$, to capture the total amount of the complex asymmetries in these regions.

7.3.2 Geometrical proxies: ellipticity and connectivity

After having established the relationship of the βs with the radius, we wanted to relate the harmonic asymmetries, traced by the β parameters, with the underlying geometry of the matter density field in the two regions of interest (inside and around galaxy clusters). Inside clusters, we use the ellipticity as tracer of the triaxial shape of clusters, and we compared it to the quadrupole moment estimator β_2 computed in the aperture $[0-1]R_{200}$. In the cluster outskirts, on the other hand, we take the connectivity as measure of the number of filaments connected to the cluster at $R = 1.5\,R_{200}$, compared to the total level of asymmetries, β_{2+3+4}, computed in the aperture $[1-2]R_{200}$.

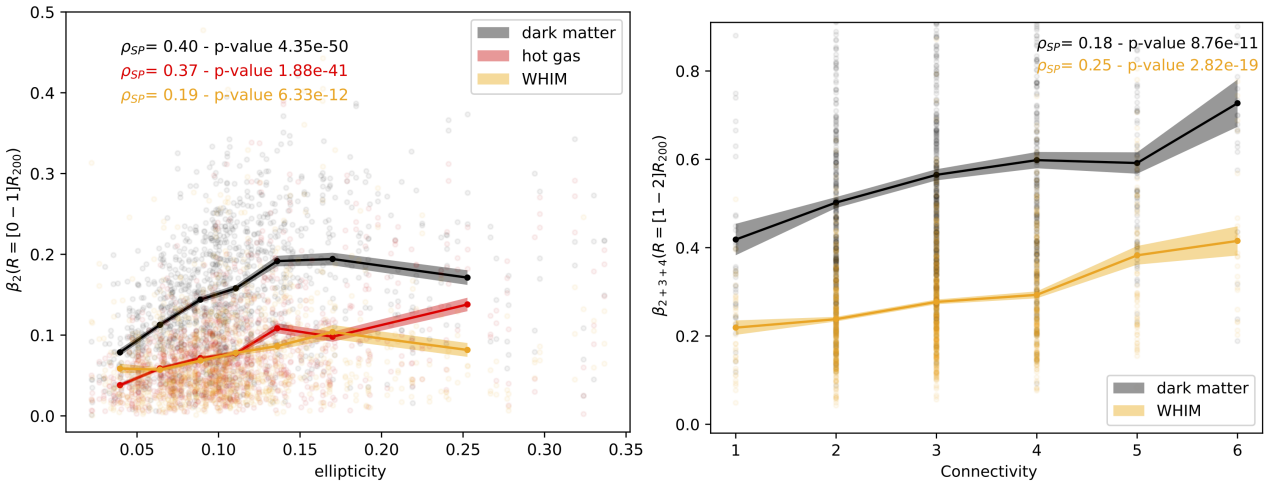

(a) (b)

Figure 7.7: Comparison of the asymmetry level of matter distribution with galaxy clusters' geometrical proxies, for dark matter (in black), hot medium (red) and WHIM (orange). Each dot represents a cluster projection, the solid lines are the average in bins of the cluster property. The values of the Spearman coefficients, $\rho_{\rm sp}$, and relative p-values are quoted for each matter component. (*Left*): β_2 inside clusters ($[0-1]R_{200}$) with respect to the clusters' ellipticity. (*Right*): β_{2+3+4} outside clusters ($[1-4]R_{200}$) with respect to the clusters' connectivity.

In Fig. 7.7(a) we see the results of this analysis in the inner regions of clusters. We notice that β_2 is strongly correlated with the ellipticity. This fact confirms our previous statements about strong quadrupolar power, that is, the more quadrupolar is the matter distribution, the more elliptical is the cluster shape. Looking at the different components of matter considered, we see that the dark matter is the one with the strongest correlation, which is understandable since the ellipticity was computed using only DM particles, but we can notice how the hot medium follows approximately the same trend and it has a very similar Spearman coefficient to the DM. Finally, the WHIM seems to be a little less correlated to the ellipticity with respect to the other two components, but the correlation is still significant. In general, we notice that the gas components have lower values of β_2 than the dark matter on average; this fact can be understood remembering that gas, unlike DM, is affected by pressure forces that tend to symmetrize the distribution, thus lowering the asymmetry level with respect to the collisionless dark matter. From these results we can see that the hot medium, being the dominant gas component in these regions, follows the dark matter distribution and traces very well the ellipticity of the cluster. On the other hand, the WHIM distribution, while still strongly influenced by the elliptical shape of the cluster, seems to be affected also by other factors.

Turning to the outer parts of galaxy clusters, in Fig. 7.7(b) we see the comparison of β_{2+3+4} with the connectivity. Also here we see that there is a good correlation between the two parameters for both DM and WHIM, such that a cluster with higher asymmetry level is generally more connected to the cosmic web, which is a confirmation that regions with more complex signatures in harmonic space can be associated with more branched filamentary structures. This result is in agreement with [20], who found that the gas in filaments is mainly in the phase of WHIM.

7.3.3 Dependence on the cluster mass

We then studied the relationship of the matter asymmetries with respect to the mass of the cluster. We considered the dependence on the cluster mass both in the inner region ($[0-1]R_{200}$) and in the outskirts (using the aperture $[1-4]R_{200}$).

For the inner part of clusters, we show the result in Fig. 7.8(a). We see that the three matter

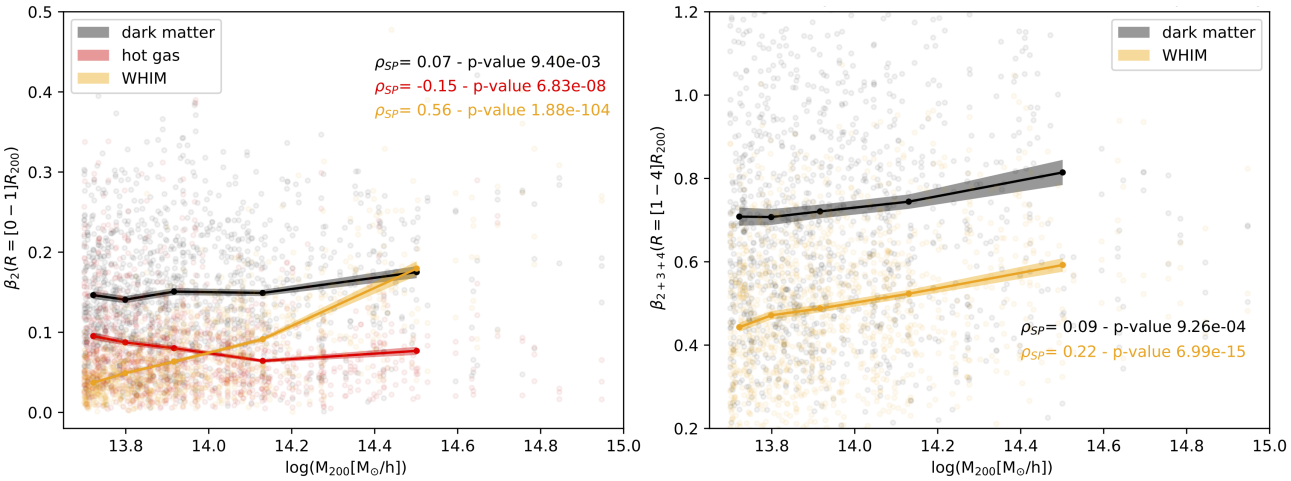

(a) (b)

Figure 7.8: Comparison of the asymmetry level of matter distribution with galaxy cluster's mass, for dark matter (in black), hot medium (red) and WHIM (orange). Each dot represents a cluster projection, the solid lines are the average in bins of the cluster property. The values of the Spearman coefficients, $\rho_{\rm sp}$, and relative p-values are quoted for each matter component. (*Left*): β_2 inside clusters ($[0-1]R_{200}$). (*Right*): β_{2+3+4} outside clusters ($[1-4]R_{200}$).

components we consider show three different behaviours. First of all we can see that the asymmetry level of the dark matter seems to be almost independent on the mass of the cluster, we can see only a slight increase with mass, confirmed by a low value of the Spearman coefficient. On the other hand, we can observe how the WHIM phase shows a much more significant increase with the mass, with the average value of β_2 becoming comparable with the one of dark matter in the most massive clusters. This is consistent with our expectations and previous studies [3, 14, 21, 22], which show that, in general, more massive clusters are both more elliptical and more connected to the cosmic web. Somewhat contrary to our expectations is instead the behaviour of the hot gas, which seem to be more asymmetrically distributed in low-mass clusters than in high-mass ones. One way to interpret this result is to remember that this gas phase gets heated to its high temperature through shocks [68], that spread the gas over a larger volume than the DM, and symmetrizing its distribution. Since we expect shocks to be found at the interface of clusters and filaments, a more connected cluster will have more shocks on average, thus its infalling gas will have more opportunities to be symmetrized, with respect to a poorly connected one. Nevertheless, other explanations are possible, so this behaviour has to be studied in more detail in a future study.

Looking now at Fig. 7.8(b) we see the results obtained in the outskirts of galaxy clusters. Here we see that both DM and WHIM asymmetries increase with the mass, coherently with our expectations, with the WHIM showing a higher correlation coefficient than the dark matter. This results confirms the fact that more massive clusters seem to have stronger asymmetries and more complex matter distribution in their outskirts.

7.3.4 Dependence on the cluster's dynamical state

The last cluster property we related to the level of matter anisotropies is the relaxedness, which measures the level of dynamical relaxation of the cluster, as explained in section 3.3.

In both panels of Fig. 7.9, we see that the level of asymmetry is anti-correlated with the relaxedness, so that the unrelaxed clusters are the ones with higher asymmetries, while the relaxed ones tend to have more isotropic matter distributions. This confirms the results of [22], that compared the relaxedness

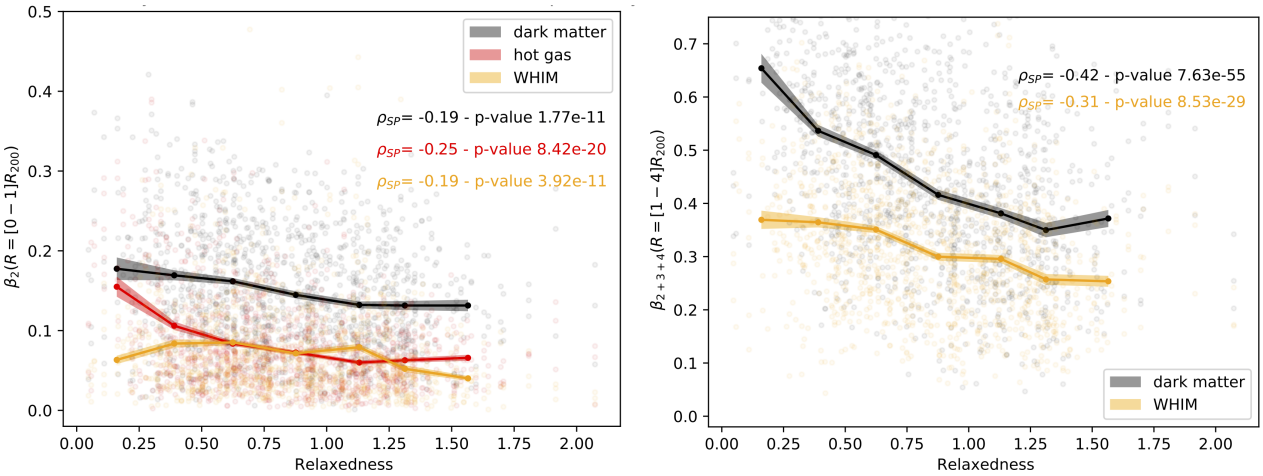

(a) (b)

Figure 7.9: Comparison of the asymmetry level of matter distribution with galaxy cluster's relaxedness, for dark matter (in black), hot medium (red) and WHIM (orange). Each dot represents a cluster projection, the solid lines are the average in bins of the cluster property. The values of the Spearman coefficients, $\rho_{\rm sp}$, and relative p-values are quoted for each matter component. (*Left*): β_2 inside clusters ($[0-1]R_{200}$). (*Right*): β_{2+3+4} outside clusters ($[1-4]R_{200}$).

Table 7.1: Values of the Spearman rank correlation coefficient, $\rho_{\rm sp}$, and the corresponding p-values, of the cluster parameters below with respect to the probes of asymmetries: β_2 inside clusters ($[0-1]R_{200}$), and β_{2+3+4} in the cluster outskirts ($[1-4]$ or $[1-2]R_{200}$).

	Dark matter		WHIM		HM	
	$\rho_{\rm sp}$	p-value	$\rho_{\rm sp}$	p-value	$\rho_{\rm sp}$	p-value
Ellipticity ($R = [0-1]R_{200}$)	0.40	4.35×10^{-50}	0.19	6.33×10^{-12}	0.37	1.88×10^{-41}
Connectivity ($R = [1-2]R_{200}$)	0.18	8.67×10^{-11}	0.25	2.82×10^{-19}	–	–
Mass inside	0.07	9.40×10^{-3}	0.56	1.88×10^{-104}	-0.15	6.83×10^{-8}
Mass outside	0.09	9.26×10^{-4}	0.22	6.99×10^{-15}	–	–
Relaxedness inside	-0.19	1.77×10^{-11}	-0.19	3.92×10^{-11}	-0.25	8.42×10^{-20}
Relaxedness outside	-0.42	7.63×10^{-55}	-0.31	8.53×10^{-29}	–	–

with the ellipticity and the connectivity. Looking at the different components we see that, inside clusters, the HM distribution seems to be the one that gets most influenced by the dynamical state of the cluster, with a higher Spearman coefficient in modulo compared to the other components. For DM the average β_2 decreases monotonically with the relaxedness, although less drastically than the HM. The average β_2 of the WHIM distribution has a more complicated shape, but it still shows an overall descent for higher values of the relaxedness. In the outer regions of clusters we can see that both dark matter and WHIM are strongly anti-correlated with the relaxedness, with a similar shape of the average β_{2+3+4} profile, a sign that the filamentary patterns of both WHIM and DM are strongly influenced by the dynamical state of matter inside the clusters, consistent with the results of [22].

7.4 Conclusions

In this Chapter, we presented the results obtained analyzing how the level of anisotropy of matter distribution in and around galaxy clusters depends on various cluster properties. To estimate the level of asymmetries we used a new method based on aperture multipole moments decomposition, through the use of the β parameters that we introduced in Section 4.3.

We decided to analyze three matter components: dark matter, hot gas and WHIM. Dark matter and WHIM were considered both inside and in the outskirts of galaxy clusters, while the analysis of the hot medium was restricted to the region inside R_{200}, due to the limit of our method in distinguishing a clumpy distribution from an extended filamentary one.

The results of this Chapter are summarized below:

- We saw that asymmetries in the matter distribution grow consistently from the center to the oustskirts of galaxy clusters. In the inner regions of clusters (up to R_{200}), the dominant multipole contribution is the quadrupole, in agreement with our previous results and previous studies [21,23]. In the clusters' outer regions (from 1 to $4R_{200}$), $\beta_{2,3,4}$ become the three dominant orders to describe the complex filamentary patterns in the matter distribution.
- We found a good correlation between the level of azimuthal symmetries, quantified by $\beta_{2,3,4}$, and other probes of matter asymmetry. We related β_2 inside clusters with the ellipticity, and β_{2+3+4} in the outskirts with the connectivity, finding that our β parameters are good estimators of the geometrical properties of the matter distribution.
- Relating the β parameters with the mass of the cluster, we saw that WHIM and dark matter anisotropies grow with increasing mass, both inside and in the vicinity of clusters, although the correlation is weak in the case of dark matter. This is coherent with previous studies' results, for example [3,14,21,22]. For the hot medium we found instead the opposite behaviour, with more massive clusters having a more spherical HM distribution than low-mass ones. The explanation for this fact is not clear yet, and it has to be further investigated.
- Finally, we studied the relationship between the level of asymmetries and the dynamical state of the cluster, represented by the relaxedness parameter. We found that the β parameters of all the components considered are anti-correlated with the relaxedness, both in the inner and the outer regions of clusters. Therefore it means that more relaxed clusters tend to have more spherical distributions, whereas newly formed, unrelaxed clusters have matter distributions that are in general more anisotropic.

Chapter 8

Conclusions

In this work we investigated the distribution of different matter components in the environment of galaxy clusters. In particular we characterised the asymmetries of the distribution of dark matter, galaxies and different gas phases (hot medium, WHIM, diffuse IGM), in two regions: one selecting their insides and the other focused on their outskirts. To do this, we performed a multipolar harmonic decomposition of the projected density field in these two regions, which served as a basis for our subsequent statistical analyses. We used the data from the cosmological hydrodynamical simulation suite IllustrisTNG, in particular the largest simulation of the suite, TNG300, at $z = 0$.

We approached the project with two questions. The first one was: how is matter in galaxy clusters distributed with respect to the background density field of the Universe? To answer this question we computed the harmonic decomposition of the projected density field of galaxies and gas, respectively. While the results obtained from the analysis of the galaxy distribution are mostly in agreement with previous studies [21, 23] (see Chapter 5), the analysis of the gas proved to be more problematic. Computing the harmonic power excess of the gas component inside $1 \times R_{200}$ from the cluster center produces a multipole distribution that we are not able to interpret at this stage. We suppose that this peculiar shape of the harmonic power excess is due to an incorrect characterization of the background field, maybe due to a lack of gas particles, but we have not found yet a proof for this hypothesis. Therefore, this aspects has to be further studied in a future work. Focusing on the cluster outskirts, we analyzed the distribution of three gas phases: hot medium, WHIM and diffuse IGM. We found that the hot gas is situated mainly in clusters, and is a good tracer of their average elliptical shape, while the WHIM is the phase that better traces the filamentary structures of the cosmic web connected to the clusters, which is consistent with the results of [20]. Studying the diffuse IGM, we found that this gas phase has lower multipolar powers around clusters than in the background field, which is again difficult to interpret, and needs further examination in the future.

The second question we addressed was how the level of anisotropy of the matter distribution in galaxy clusters is related to the properties of the clusters. We therefore introduced a new set of parameters to characterize the asymmetries of the matter distribution: the β parameters. We first analyzed the strengths and the limitations of these parameters, to define the limits of applicability of this new approach. We found that the β parameters are affected by the shot noise of the discrete matter distribution only when the number of particles is below ~ 100, and above this number they converge to the theoretical expected value. We also discussed how a clumpy matter distribution can influence the values of the β parameters, finding that such a distribution produces complex results that cannot be interpreted in terms of similarity with simple multipolar distributions. Using these results as guides, we estimated the level of asymmetries in the distribution of dark matter, hot medium and WHIM in galaxy clusters' environments, studying their correlation with clusters' parameters. In general, we saw that the matter distribution tends to become more anisotropic and more complex going from the

clusters' cores to their outskirts. We also found that the β parameters are well correlated with other probes of matter asymmetries, namely the ellipticity and the connectivity, confirming the validity of our method. Comparing the level of matter asymmetries with the cluster mass, we found that the WHIM and (to a lesser extent) dark matter distributions tend to be less spherical in more massive clusters (as found in other studies, e.g. [3,14]). Looking at the dependence of the asymmetry level of the hot gas on the cluster mass, we saw an opposite trend instead, with a more isotropic gas distribution in massive clusters than in low-mass ones. We gave a tentative explanation of this result, but it needs to be confirmed in further studies. Finally, we found an anticorrelation between the asymmetry level and the dynamical relaxedness of the cluster, which confirms the standard hierarchical scenario of structure formation, with newly-formed, unrelaxed clusters being also the most asymmetrical ones and the most connected to the large scale structures.

In conclusion, this work shows that the harmonic decomposition of the projected matter density can be a powerful tool to probe the departure from spherical symmetry of the matter distribution. As we have shown, the level of asymmetry of the various matter components, evaluated through our β parameters, is correlated to clusters' physical properties up to $4 \times R_{200}$. This approach can be therefore applied also to real observational data, in particular to the new and upcoming high-resolution gas observations. Indeed, future X-ray observation missions and upcoming SZ experiments will allow us to explore the hidden gas around clusters in the coming years, such as eROSITA [41] (launched in 2019), and XRISM [71] (launch in 2021) and Advanced-ACT [27] (ground-based telescope started in 2016).

Acknowledgments

During the time I worked on this thesis, and during the course of my studies, I had the opportunity to meet and interact with a lot of amazing people, without whom it would not have been possible to get where I am now. So many that it would be impossible for me to thank them all here. Therefore, this list of acknowledgments will necessarily be severely incomplete.

My first immense thanks go to my two supervisors at the Institut d'Astrophysique Spatiale in Orsay, France. To Dr. Nabila Aghanim, for agreeing on being my supervisor, for welcoming me in the team, for supporting me throughout the thesis work, especially in the difficult conditions we were forced to deal with due to the pandemic, for all the fruitful discussions, insights and feedback on my work, for giving me the opportunity to do a second internship at IAS, and for all the administrative work to make it actually happen. To Dr. Céline Gouin, for introducing me to her previous work on multipole moments, for guiding me step by step during my work, for helping me grow and get better as a scientist, for all the long discussions on the β methods and the very valuable feedback for the thesis. I also want to thank all the colleagues at IAS, for making me feel immediately part of the team and teaching me a lot on various topics, as well as what it means to be a researcher.

Another huge thank you goes to Prof. Sabino Matarrese for his continuous support, patience, kindness and advice while supervising my work, for all the fundamental notions I learnt attending his courses, and also for introducing me to Dr. Aghanim, when I was searching a supervisor in Paris. I also want to thank Prof. Giulia Rodighiero, for the insightful comments and questions on my work during our conversations, as well as her always kind words and manners. I then want to thank all the people involved in the IllustrisTNG project for making their data publicly available, without their impressive work this thesis would have looked very different.

I finally must thank all the people without whom I would not be here. Thanks to my family and to Sofia, who always supported me unconditionally throughout my studies, helping me through the tough moments and pushing me to reach my goals even when they seemed too big to me. Thanks to all my friends, but especially the Balotta group: during these years of university we shared lectures, lunches, study sessions, coffee breaks, days, nights, drinks, breakfasts, holidays, houses, sofas, Christmas parties, and the list could continue for long. You made these years truly unforgettable, and so much fun, thank you so much.

Bibliography

[1] G. O. Abell. The Distribution of Rich Clusters of Galaxies. *Astrophysical Journal, Supplement*, 3:211, May 1958.

[2] S. W. Allen, A. E. Evrard, and A. B. Mantz. Cosmological Parameters from Observations of Galaxy Clusters. *Annual Review of Astronomy and Astrophysics*, 49(1):409–470, Sept. 2011.

[3] M. A. Aragón-Calvo, R. van de Weygaert, and B. J. T. Jones. Multiscale phenomenology of the cosmic web. *Monthly Notices of the Royal Astronomical Society*, 408(4):2163–2187, Nov. 2010.

[4] M. Bartelmann. TOPICAL REVIEW Gravitational lensing. *Classical and Quantum Gravity*, 27(23):233001, Dec. 2010.

[5] M. Bilicki, J. A. Peacock, T. H. Jarrett, M. E. Cluver, N. Maddox, M. J. I. Brown, E. N. Taylor, N. C. Hambly, A. Solarz, B. W. Holwerda, I. Baldry, J. Loveday, A. Moffett, A. M. Hopkins, S. P. Driver, M. Alpaslan, and J. Bland-Hawthorn. WISE × SuperCOSMOS Photometric Redshift Catalog: 20 Million Galaxies over 3/pi Steradians. *Astrophysical Journal, Supplement*, 225(1):5, July 2016.

[6] J. R. Bond, L. Kofman, and D. Pogosyan. How filaments of galaxies are woven into the cosmic web. *Nature*, 380(6575):603–606, Apr. 1996.

[7] V. Bonjean, N. Aghanim, P. Salomé, M. Douspis, and A. Beelen. Gas and galaxies in filaments between clusters of galaxies. The study of A399-A401. *Astronomy and Astrophysics*, 609:A49, Jan. 2018.

[8] T. Bonnaire, N. Aghanim, A. Decelle, and M. Douspis. T-ReX: a graph-based filament detection method. *Astronomy and Astrophysics*, 637:A18, May 2020.

[9] J. S. Bullock, T. S. Kolatt, Y. Sigad, R. S. Somerville, A. V. Kravtsov, A. A. Klypin, J. R. Primack, and A. Dekel. Profiles of dark haloes: evolution, scatter and environment. *Monthly Notices of the Royal Astronomical Society*, 321(3):559–575, Mar. 2001.

[10] J. Clampitt and B. Jain. Lensing measurements of the ellipticity of luminous red galaxies dark matter haloes. *Monthly Notices of the Royal Astronomical Society*, 457(4):4135–4146, Apr. 2016.

[11] S. Cole, W. J. Percival, J. A. Peacock, P. Norberg, C. M. Baugh, C. S. Frenk, I. Baldry, J. Bland-Hawthorn, T. Bridges, R. Cannon, M. Colless, C. Collins, W. Couch, N. J. G. Cross, G. Dalton, V. R. Eke, R. De Propris, S. P. Driver, G. Efstathiou, R. S. Ellis, K. Glazebrook, C. Jackson, A. Jenkins, O. Lahav, I. Lewis, S. Lumsden, S. Maddox, D. Madgwick, B. A. Peterson, W. Sutherland, and K. Taylor. The 2dF Galaxy Redshift Survey: power-spectrum analysis of the final data set and cosmological implications. *Monthly Notices of the Royal Astronomical Society*, 362(2):505–534, Sept. 2005.

[12] P. Coles and F. Lucchin. *Cosmology: The Origin and Evolution of Cosmic Structure, Second Edition*. 2002.

[13] V. de Lapparent, M. J. Geller, and J. P. Huchra. A Slice of the Universe. *Astrophysical Journal, Letters*, 302:L1, Mar. 1986.

[14] G. Despali, C. Giocoli, and G. Tormen. Some like it triaxial: the universality of dark matter halo shapes and their evolution along the cosmic time. *Monthly Notices of the Royal Astronomical Society*, 443(4):3208–3217, Oct. 2014.

[15] E. Di Valentino, O. Mena, S. Pan, L. Visinelli, W. Yang, A. Melchiorri, D. F. Mota, A. G. Riess, and J. Silk. In the Realm of the Hubble tension − a Review of Solutions. *arXiv e-prints*, page arXiv:2103.01183, Mar. 2021.

[16] J. P. Dietrich, P. Schneider, D. Clowe, E. Romano-Díaz, and J. Kerp. Weak lensing study of dark matter filaments and application to the binary cluster A 222 and A 223. *Astronomy and Astrophysics*, 440(2):453–471, Sept. 2005.

[17] K. Dolag, S. Borgani, G. Murante, and V. Springel. Substructures in hydrodynamical cluster simulations. *Monthly Notices of the Royal Astronomical Society*, 399(2):497–514, Oct. 2009.

[18] A. A. Dutton and A. V. Macciò. Cold dark matter haloes in the Planck era: evolution of structural parameters for Einasto and NFW profiles. *Monthly Notices of the Royal Astronomical Society*, 441(4):3359–3374, July 2014.

[19] D. Eckert, F. Vazza, S. Ettori, S. Molendi, D. Nagai, E. T. Lau, M. Roncarelli, M. Rossetti, S. L. Snowden, and F. Gastaldello. The gas distribution in the outer regions of galaxy clusters. *Astronomy and Astrophysics*, 541:A57, May 2012.

[20] D. Galárraga-Espinosa, N. Aghanim, M. Langer, and H. Tanimura. Properties of gas phases around cosmic filaments at z = 0 in the IllustrisTNG simulation. *Astronomy and Astrophysics*, 649:A117, May 2021.

[21] C. Gouin, N. Aghanim, V. Bonjean, and M. Douspis. Probing the azimuthal environment of galaxies around clusters. From cluster core to cosmic filaments. *Astronomy and Astrophysics*, 635:A195, Mar. 2020.

[22] C. Gouin, T. Bonnaire, and N. Aghanim. Shape and connectivity of groups and clusters: Effect of the dynamical state and accretion history. *Astronomy and Astrophysics*, 651:A56, July 2021.

[23] C. Gouin, R. Gavazzi, S. Codis, C. Pichon, S. Peirani, and Y. Dubois. Multipolar moments of weak lensing signal around clusters. Weighing filaments in harmonic space. *Astronomy and Astrophysics*, 605:A27, Sept. 2017.

[24] S. N. Gurbatov, A. I. Saichev, and S. F. Shandarin. Large-scale structure of the Universe. The Zeldovich approximation and the adhesion model. *Physics Uspekhi*, 55(3):223–249, Mar. 2012.

[25] A. H. Guth and S. Y. Pi. Fluctuations in the New Inflationary Universe. *Physical Review Letters*, 49(15):1110–1113, Oct. 1982.

[26] R. Haggar, M. E. Gray, F. R. Pearce, A. Knebe, W. Cui, R. Mostoghiu, and G. Yepes. The Three Hundred project: backsplash galaxies in simulations of clusters. *Monthly Notices of the Royal Astronomical Society*, 492(4):6074–6085, Mar. 2020.

[27] M. Hilton, C. Sifón, S. Naess, M. Madhavacheril, M. Oguri, E. Rozo, E. Rykoff, T. M. C. Abbott, S. Adhikari, M. Aguena, S. Aiola, S. Allam, S. Amodeo, A. Amon, J. Annis, B. Ansarinejad, C. Aros-Bunster, J. E. Austermann, S. Avila, D. Bacon, N. Battaglia, J. A. Beall, D. T. Becker, G. M. Bernstein, E. Bertin, T. Bhandarkar, S. Bhargava, J. R. Bond, D. Brooks, D. L. Burke, E. Calabrese, M. Carrasco Kind, J. Carretero, S. K. Choi, A. Choi, C. Conselice, L. N. da Costa, M. Costanzi, D. Crichton, K. T. Crowley, R. Dünner, E. V. Denison, M. J. Devlin, S. R. Dicker,

H. T. Diehl, J. P. Dietrich, P. Doel, S. M. Duff, A. J. Duivenvoorden, J. Dunkley, S. Everett, S. Ferraro, I. Ferrero, A. Ferté, B. Flaugher, J. Frieman, P. A. Gallardo, J. García-Bellido, E. Gaztanaga, D. W. Gerdes, P. Giles, J. E. Golec, M. B. Gralla, S. Grandis, D. Gruen, R. A. Gruendl, J. Gschwend, G. Gutierrez, D. Han, W. G. Hartley, M. Hasselfield, J. C. Hill, G. C. Hilton, A. D. Hincks, S. R. Hinton, S. P. P. Ho, K. Honscheid, B. Hoyle, J. Hubmayr, K. M. Huffenberger, J. P. Hughes, A. T. Jaelani, B. Jain, D. J. James, T. Jeltema, S. Kent, K. Knowles, B. J. Koopman, K. Kuehn, O. Lahav, M. Lima, Y. T. Lin, M. Lokken, S. I. Loubser, N. MacCrann, M. A. G. Maia, T. A. Marriage, J. Martin, J. McMahon, P. Melchior, F. Menanteau, R. Miquel, H. Miyatake, K. Moodley, R. Morgan, T. Mroczkowski, F. Nati, L. B. Newburgh, M. D. Niemack, A. J. Nishizawa, R. L. C. Ogando, J. Orlowski-Scherer, L. A. Page, A. Palmese, B. Partridge, F. Paz-Chinchón, P. Phakathi, A. A. Plazas, N. C. Robertson, A. K. Romer, A. Carnero Rosell, M. Salatino, E. Sanchez, E. Schaan, A. Schillaci, N. Sehgal, S. Serrano, T. Shin, S. M. Simon, M. Smith, M. Soares-Santos, D. N. Spergel, S. T. Staggs, E. R. Storer, E. Suchyta, M. E. C. Swanson, G. Tarle, D. Thomas, C. To, H. Trac, J. N. Ullom, L. R. Vale, J. Van Lanen, E. M. Vavagiakis, J. De Vicente, R. D. Wilkinson, E. J. Wollack, Z. Xu, and Y. Zhang. The Atacama Cosmology Telescope: A Catalog of > 4000 Sunyaev–Zel'dovich Galaxy Clusters. *Astrophysical Journal, Supplement*, 253(1):3, Mar. 2021.

[28] J. H. Jeans. The Stability of a Spherical Nebula. *Philosophical Transactions of the Royal Society of London Series A*, 199:1–53, Jan. 1902.

[29] Y. P. Jing. The Density Profile of Equilibrium and Nonequilibrium Dark Matter Halos. *Astrophysical Journal*, 535(1):30–36, May 2000.

[30] Y. P. Jing and Y. Suto. Triaxial Modeling of Halo Density Profiles with High-Resolution N-Body Simulations. *Astrophysical Journal*, 574(2):538–553, Aug. 2002.

[31] S. F. Kasun and A. E. Evrard. Shapes and Alignments of Galaxy Cluster Halos. *Astrophysical Journal*, 629(2):781–790, Aug. 2005.

[32] A. A. Klypin, S. Trujillo-Gomez, and J. Primack. Dark Matter Halos in the Standard Cosmological Model: Results from the Bolshoi Simulation. *Astrophysical Journal*, 740(2):102, Oct. 2011.

[33] A. V. Kravtsov and S. Borgani. Formation of Galaxy Clusters. *Annual Review of Astronomy and Astrophysics*, 50:353–409, Sept. 2012.

[34] J. Kuruvilla and N. Aghanim. Information content in mean pairwise velocity and mean relative velocity between pairs in a triplet. *arXiv e-prints*, page arXiv:2102.06709, Feb. 2021.

[35] M. Limousin, A. Morandi, M. Sereno, M. Meneghetti, S. Ettori, M. Bartelmann, and T. Verdugo. The Three-Dimensional Shapes of Galaxy Clusters. *Space Science Reviews*, 177(1-4):155–194, Aug. 2013.

[36] A. V. Macciò, A. A. Dutton, and F. C. van den Bosch. Concentration, spin and shape of dark matter haloes as a function of the cosmological model: WMAP1, WMAP3 and WMAP5 results. *Monthly Notices of the Royal Astronomical Society*, 391(4):1940–1954, Dec. 2008.

[37] F. Marinacci, M. Vogelsberger, R. Pakmor, P. Torrey, V. Springel, L. Hernquist, D. Nelson, R. Weinberger, A. Pillepich, J. Naiman, and S. Genel. First results from the IllustrisTNG simulations: radio haloes and magnetic fields. *Monthly Notices of the Royal Astronomical Society*, 480(4):5113–5139, Nov. 2018.

[38] D. Martizzi, M. Vogelsberger, M. C. Artale, M. Haider, P. Torrey, F. Marinacci, D. Nelson, A. Pillepich, R. Weinberger, L. Hernquist, J. Naiman, and V. Springel. Baryons in the Cosmic Web of IllustrisTNG - I: gas in knots, filaments, sheets, and voids. *Monthly Notices of the Royal Astronomical Society*, 486(3):3766–3787, July 2019.

[39] B. R. McNamara and P. E. J. Nulsen. Mechanical feedback from active galactic nuclei in galaxies, groups and clusters. *New Journal of Physics*, 14(5):055023, May 2012.

[40] J. M. G. Mead, L. J. King, and I. G. McCarthy. Probing the cosmic web: intercluster filament detection using gravitational lensing. *Monthly Notices of the Royal Astronomical Society*, 401(4):2257–2267, Feb. 2010.

[41] A. Merloni, P. Predehl, W. Becker, H. Böhringer, T. Boller, H. Brunner, M. Brusa, K. Dennerl, M. Freyberg, P. Friedrich, A. Georgakakis, F. Haberl, G. Hasinger, N. Meidinger, J. Mohr, K. Nandra, A. Rau, T. H. Reiprich, J. Robrade, M. Salvato, A. Santangelo, M. Sasaki, A. Schwope, J. Wilms, and t. German eROSITA Consortium. eROSITA Science Book: Mapping the Structure of the Energetic Universe. *arXiv e-prints*, page arXiv:1209.3114, Sept. 2012.

[42] J. P. Naiman, A. Pillepich, V. Springel, E. Ramirez-Ruiz, P. Torrey, M. Vogelsberger, R. Pakmor, D. Nelson, F. Marinacci, L. Hernquist, R. Weinberger, and S. Genel. First results from the IllustrisTNG simulations: a tale of two elements - chemical evolution of magnesium and europium. *Monthly Notices of the Royal Astronomical Society*, 477(1):1206–1224, June 2018.

[43] J. F. Navarro, C. S. Frenk, and S. D. M. White. A Universal Density Profile from Hierarchical Clustering. *Astrophysical Journal*, 490(2):493–508, Dec. 1997.

[44] D. Nelson, A. Pillepich, V. Springel, R. Weinberger, L. Hernquist, R. Pakmor, S. Genel, P. Torrey, M. Vogelsberger, G. Kauffmann, F. Marinacci, and J. Naiman. First results from the IllustrisTNG simulations: the galaxy colour bimodality. *Monthly Notices of the Royal Astronomical Society*, 475(1):624–647, Mar. 2018.

[45] D. Nelson, V. Springel, A. Pillepich, V. Rodriguez-Gomez, P. Torrey, S. Genel, M. Vogelsberger, R. Pakmor, F. Marinacci, R. Weinberger, L. Kelley, M. Lovell, B. Diemer, and L. Hernquist. The IllustrisTNG simulations: public data release. *Computational Astrophysics and Cosmology*, 6(1):2, May 2019.

[46] A. F. Neto, L. Gao, P. Bett, S. Cole, J. F. Navarro, C. S. Frenk, S. D. M. White, V. Springel, and A. Jenkins. The statistics of Λ CDM halo concentrations. *Monthly Notices of the Royal Astronomical Society*, 381(4):1450–1462, Nov. 2007.

[47] P. J. E. Peebles. *The large-scale structure of the universe*. 1980.

[48] R. Piffaretti, M. Arnaud, G. W. Pratt, E. Pointecouteau, and J. B. Melin. The MCXC: a meta-catalogue of x-ray detected clusters of galaxies. *Astronomy and Astrophysics*, 534:A109, Oct. 2011.

[49] A. Pillepich, D. Nelson, L. Hernquist, V. Springel, R. Pakmor, P. Torrey, R. Weinberger, S. Genel, J. P. Naiman, F. Marinacci, and M. Vogelsberger. First results from the IllustrisTNG simulations: the stellar mass content of groups and clusters of galaxies. *Monthly Notices of the Royal Astronomical Society*, 475(1):648–675, Mar. 2018.

[50] A. Pillepich, V. Springel, D. Nelson, S. Genel, J. Naiman, R. Pakmor, L. Hernquist, P. Torrey, M. Vogelsberger, R. Weinberger, and F. Marinacci. Simulating galaxy formation with the IllustrisTNG model. *Monthly Notices of the Royal Astronomical Society*, 473(3):4077–4106, Jan. 2018.

[51] Planck Collaboration. Planck 2015 results. XIII. Cosmological parameters. *Astronomy and Astrophysics*, 594:A13, Sept. 2016.

[52] Planck Collaboration. Planck 2015 results. XXVII. The second Planck catalogue of Sunyaev-Zeldovich sources. *Astronomy and Astrophysics*, 594:A27, Sept. 2016.

[53] S. Planelles, D. R. G. Schleicher, and A. M. Bykov. Large-Scale Structure Formation: From the First Non-linear Objects to Massive Galaxy Clusters. *Space Science Reviews*, 188(1-4):93–139, May 2015.

[54] F. Prada, A. A. Klypin, A. J. Cuesta, J. E. Betancort-Rijo, and J. Primack. Halo concentrations in the standard Λ cold dark matter cosmology. *Monthly Notices of the Royal Astronomical Society*, 423(4):3018–3030, July 2012.

[55] T. H. Reiprich, K. Basu, S. Ettori, H. Israel, L. Lovisari, S. Molendi, E. Pointecouteau, and M. Roncarelli. Outskirts of Galaxy Clusters. *Space Science Reviews*, 177(1-4):195–245, Aug. 2013.

[56] A. Rost, U. Kuchner, C. Welker, F. Pearce, F. Stasyszyn, M. Gray, W. Cui, R. Dave, A. Knebe, G. Yepes, and E. Rasia. The ThreeHundred: the structure and properties of cosmic filaments in the outskirts of galaxy clusters. *Monthly Notices of the Royal Astronomical Society*, 502(1):714–727, Mar. 2021.

[57] J. Schmalzing, T. Buchert, A. L. Melott, V. Sahni, B. S. Sathyaprakash, and S. F. Shandarin. Disentangling the Cosmic Web. I. Morphology of Isodensity Contours. *Astrophysical Journal*, 526(2):568–578, Dec. 1999.

[58] P. Schneider and M. Bartelmann. Aperture multipole moments from weak gravitational lensing. *Monthly Notices of the Royal Astronomical Society*, 286(3):696–708, Apr. 1997.

[59] T.-h. Shin, J. Clampitt, B. Jain, G. Bernstein, A. Neil, E. Rozo, and E. Rykoff. The ellipticity of galaxy cluster haloes from satellite galaxies and weak lensing. *Monthly Notices of the Royal Astronomical Society*, 475(2):2421–2437, Apr. 2018.

[60] V. Springel. E pur si muove: Galilean-invariant cosmological hydrodynamical simulations on a moving mesh. *Monthly Notices of the Royal Astronomical Society*, 401(2):791–851, Jan. 2010.

[61] V. Springel, R. Pakmor, A. Pillepich, R. Weinberger, D. Nelson, L. Hernquist, M. Vogelsberger, S. Genel, P. Torrey, F. Marinacci, and J. Naiman. First results from the IllustrisTNG simulations: matter and galaxy clustering. *Monthly Notices of the Royal Astronomical Society*, 475(1):676–698, Mar. 2018.

[62] V. Springel, S. D. M. White, G. Tormen, and G. Kauffmann. Populating a cluster of galaxies - I. Results at $z = 0$. *Monthly Notices of the Royal Astronomical Society*, 328(3):726–750, Dec. 2001.

[63] H. Tanimura, N. Aghanim, V. Bonjean, N. Malavasi, and M. Douspis. Density and temperature of cosmic-web filaments on scales of tens of megaparsecs. *arXiv e-prints*, page arXiv:1911.09706, Nov 2019.

[64] H. Tanimura, G. Hinshaw, I. G. McCarthy, L. Van Waerbeke, N. Aghanim, Y.-Z. Ma, A. Mead, A. Hojjati, and T. Tröster. A search for warm/hot gas filaments between pairs of SDSS Luminous Red Galaxies. *Monthly Notices of the Royal Astronomical Society*, 483(1):223–234, Feb 2019.

[65] G. Tormen, L. Moscardini, and N. Yoshida. Properties of cluster satellites in hydrodynamical simulations. *Monthly Notices of the Royal Astronomical Society*, 350(4):1397–1408, June 2004.

[66] D. Vallés-Pérez, S. Planelles, and V. Quilis. On the accretion history of galaxy clusters: temporal and spatial distribution. *Monthly Notices of the Royal Astronomical Society*, 499(2):2303–2318, Dec. 2020.

[67] M. Vogelsberger, F. Marinacci, P. Torrey, and E. Puchwein. Cosmological simulations of galaxy formation. *Nature Reviews Physics*, 2(1):42–66, Jan. 2020.

[68] S. Walker, A. Simionescu, D. Nagai, N. Okabe, D. Eckert, T. Mroczkowski, H. Akamatsu, S. Ettori, and V. Ghirardini. The Physics of Galaxy Cluster Outskirts. *Space Science Reviews*, 215(1):7, Jan. 2019.

[69] R. Weinberger, V. Springel, L. Hernquist, A. Pillepich, F. Marinacci, R. Pakmor, D. Nelson, S. Genel, M. Vogelsberger, J. Naiman, and P. Torrey. Simulating galaxy formation with black hole driven thermal and kinetic feedback. *Monthly Notices of the Royal Astronomical Society*, 465(3):3291–3308, Mar. 2017.

[70] R. Weinberger, V. Springel, and R. Pakmor. The AREPO Public Code Release. *Astrophysical Journal, Supplement*, 248(2):32, June 2020.

[71] XRISM Science Team. Science with the X-ray Imaging and Spectroscopy Mission (XRISM). *arXiv e-prints*, page arXiv:2003.04962, Mar. 2020.

[72] D. G. York and SDSS Collaboration. The Sloan Digital Sky Survey: Technical Summary. *Astronomical Journal*, 120(3):1579–1587, Sept. 2000.

[73] Y. B. Zel'Dovich. Gravitational instability: an approximate theory for large density perturbations. *Astronomy and Astrophysics*, 500:13–18, Mar. 1970.